Spectroscopic Studies on the Impact of Defects in Hybrid Organic-Inorganic Perovskites on Charge Carrier Dynamics and Photovoltaic Device Performance

Timothy Pollock

A dissertation

Submitted in partial fulfillment of the

Requirements for the degree of

Doctor of Philosophy

University of Washington

2020

Reading Committee:

Cody Schlenker, Chair

Brandi Cossairt

Christine K. Luscombe

Program Authorized to Offer Degree:

Chemistry

University of Washington

Abstract

Spectroscopic Studies on the Impact of Defects in Hybrid Organic-Inorganic Perovskites on Charge Carrier Dynamics and Photovoltaic Device Performance

Timothy Pollock

Chair of the Supervisory Committee:

Professor Cody Schlenker

Department of Chemistry

Photovoltaic devices based on hybrid organic-inorganic perovskites have seen a historic rise in efficiency over the past decade. Relatively low cost of fabrication has allowed a wide range researchers to make meaningful contributions. This class of materials is fascinating in that it acts in some ways like well-known semiconductor systems, but exhibits certain key differences, which provides ample opportunity for future fundamental studies.

The work described in this dissertation includes the spectroscopic characterization of charge carriers in methylammonium lead iodide and the use of this characterization, along with

time-resolved spectroscopy, to better understand the influence of carrier dynamics on solar cell device performance. We observed that a decrease in device fill factor corresponded to an increase in trap state density and a change in the trapping rate constant, implying that the different film fabrication methods lead to a change in the nature of the trap states present in the film. This was an important observation at this point in photovoltaic perovskite research due to the assumption that trap states were non-detrimental to device performance.

Delving further into understanding the influence of trap states on the excited state dynamics in this system, we performed pump-push-probe spectroscopy and transient absorption spectroscopy with a variable wavelength sub-gap pump pulse to study both the energetics and kinetics of trapping processes in methylammonium lead iodide films. Here we utilized a low energy push pulse to delocalize trapped electrons back into the conduction band and then modeled the resulting recombination based on changes in trapped and free electron densities.

From these studies, we were able to add experimental observations to the body of knowledge on the electronic structure of hybrid organic-inorganic perovskites. We also showed how dynamics in the early time periods (ps-ns) following photoexcitation can influence perovskite solar cell performance.

Table of Contents

List of Figures …… iii

List of Tables ……... viii

Chapter 1: Introduction …….. 1

1.1 Photovoltaic Impact on Global Power Production ……..… 1

1.2 Maturation of Perovskite Based PV Technologies ……..…….. 3

1.3 Characterization of Lead Halide Perovskites ……..……. 5

1.4 References ……..……...…… 9

Chapter 2: Background ……..... 12

2.1 Device Physics ……..... 12

2.1.1 Device Performance Parameters …….. 12

2.1.2 Carrier Dynamics ……..... 14

2.2 Electromodulation Spectroscopy ……..… 19

2.2.1 Electronic Band Structure Analysis ……..…….. 19

2.2.2 Electromodulation Experimental Methods and Data Analysis ……... 22

2.3 Multi-pulse Laser Spectroscopy ……..…… 23

2.3.1 Transient Absorption Spectroscopy ……..……...……... 24

2.3.2 Pump-Push-Probe Spectroscopy ……..……... 30

2.4 References ……..……...……..... 32

Chapter 3: Selectively Probing Charge Carrier Dynamics in Perovskite Films …….. 35

3.1 Introduction ……..…….. 35

3.2 Experimental Methods ……..…….. 39

3.3 Results and Discussion ……...……...…… 42

3.4 Conclusions ……..... 59

3.5 References …….. 60

Chapter 4: Trap State Investigation in $CH_3NH_3PbI_3$ by Pump-Push-Probe Spectroscopy …….. 65

4.1 Introduction ……..... 65

4.2 Experimental Methods ……... 67

4.3 Results and Discussion ……..… 69

4.4 Conclusions …… 75

4.5 References …….. 76

Appendix A: Supplementary Information for Chapter 3 ……..… 78

Appendix B: Supplementary Information for Chapter 4 ……. 90

List of Figures

Figure 1-1. Global electricity generation by source as a percentage of total from 2015. Graph adapted from data made available by the International Energy Agency. ……..... 1

Figure 1-2 Perovskite ABX_3 structure. ……..… 5

Figure 1-3. (a) Representative transient absorption of a $CH_3NH_3PbI_3$ thin film. (b) Proposed band structure resulting in band gap (750 nm) and higher energy (480 nm) bleaching. Arrows show transitions which are blocked following a resonant excitation pulse. (c) Radiative (solid black arrow) and non-radiative (dashed black line) excited state decay pathways between the conduction band minimum (CBM) and valence band maximum (VBM), which can be mediated through mid-gap trap states (N_T).. ……..…….. 8

Figure 2-1. Planar heterojunction device architecture and p-i-n band profile. …… 18

Figure 2-2. Electronic band diagram showing splitting effect of spin orbit coupling. …… 20

Figure 2-3. $CH_3NH_3PbI_3$ Energy level schematic and spectra. ……..…. 25

Figure 3-1**.** Current-voltage (a) and EQE (b) comparison between representative devices made with either the one step perovskite deposition (red traces) and two step deposition procedure (black traces). …….. 43

Figure 3-2**.** Transient absorption spectra for 1-step and 2-step $CH_3NH_3PbI_3$ samples on glass at 2.5 ps with a pump wavelength of 650nm. …….. 44

Figure 3-3. (a) Cyclic voltammetry of a $CH_3NH_3PbI_3$ film deposited on a gold electrode (green traces) and on an ITO/PEDOT:PSS electrode (inset: red traces), as well as control measurements made on each working electrode (black traces). Anodic and cathodic sweeps were made on fresh samples, each starting from the cell's open circuit potential. (b) Electromodulation experimental setup. (c) Electromodulated differential reflection ($-\Delta R/R$) signal of $CH_3NH_3PbI_3$ deposited on the gold working electrode under cathodic

(black) or anodic (blue) conditions. The inset shows the transmission mode differential signal, for $CH_3NH_3PbI_3$ deposited on an ITO/PEDOT:PSS working electrode under similar conditions, with the background signal subtracted. (d) Electronic state diagram and point group notation, with and without including spin-orbit coupling (SOC), at the R-point for $CH_3NH_3PbI_3$. The solid arrows between states represent the possible transitions that we propose we are able to observe in our electromodulation spectra in Fig. 3c. …. 46

Figure 3-4. Change in absorbance (ΔA) of $CH_3NH_3PbI_3$ film after applying either a DC (a) or DC + AC (b) bias under anodic (black) and cathodic (red) conditions as described in the text. Absorbance measurements were made prior to applying an external bias and directly post spectroelectrochemical measurement. (c) Absorbance of electrolyte solution post-spectroelectrochemical measurement blanked against a solution where no bias was applied. (d) Photographs of $CH_3NH_3PbI_3$ films pre- and post-spectroelectrochemical measurement. …….. 49

Figure 3-5. (a) Experimental transient absorption spectra for the PEDOT:PSS/$CH_3NH_3PbI_3$ system. (b) Species associated spectra (SAS) and (c) decay kinetics for the electron and hole contributions to the transient absorption spectra (transparent lines) with fits to our model (dotted lines) based on Eqs. 1 - 4 in the text. (d) Energy level diagram representing our model for recombination kinetics of holes in the valence (VB) and electrons in the conduction band (CB) of $CH_3NH_3PbI_3$. As in Eqs. 1 – 4, our model incorporates a state for charge extraction (N_{TM}) and trap state (N_T) mediated recombination, yielding the dotted “Fit” lines in Fig. 5c. ……. 52

Figure 3-6. (a) Comparison of the kinetics associated with the electron lifetime (signal averaged

980-1000 nm) for the **1-step** (red) and **2-step** (black) fabrication methods with fits to Eqs. 1-3 with $k_e = k_h = 0$. Model simulation using initial parameters from **2-step** sample showing effect of (b) decreasing trap state density and (c) increasing trapping rate. (d) Comparison of the **1-step** experimental data (red) and a model simulation of the **2-step** parameters (black) with k_T and N_T replaced with those of the **1-step** values. …… 57

Figure 4-1. (a) Diagram for pump-push-probe spectroscopy (b) Schematic for transitions observed in pump-push-probe spectroscopy. (c) Transient absorption spectra in the visible and NIR (inset) showing the effect of the push pulse. (d) Comparison of kinetics for $CH_3NH_3PbI_3$ at 1000 nm induced absorption with increasing push pulse fluence. Dark lines are model fits as described in the main text. ……...… 69

Figure 4-2. (a) Transient absorption spectra for a $CH_3NH_3PbI_3$ film following a sub-gap pump pulse (1100 nm) at times corresponding to maximum pump-probe overlap (black trace) and longer valence band bleaching (blue trace). (b) Kinetics of valence band bleach (black), and sub-gap induced absorption (red). (c) Diagram showing proposed phase-space filling and bandgap renormalization as origins of sub-gap pump TA signal. Following the pump pulse, a population of holes is introduced to the valence band (blue shaded area) which results in a shift in the band extrema forming a new, lower energy bandgap ($E_{g,BGR}$). ……..…… 73

Figure A-1. Fitting of representative J-V data for 1- and 2-step devices to a simplified non-ideal diode equation (see main text). ……..…….... 78

Figure A-2. (a) Electromodulated differential reflection ($-\Delta R/R$) signal of $CH_3NH_3PbI_3$ deposited on the gold working electrode under cathodic (blue) or anodic (black) conditions. No difference was observed in the spectrum of the Au control electrode (green) comparing

the applied potentials used for anodic and cathodic measurements. (b) Electromodulated differential transmission (-ΔT/T) signal of $CH_3NH_3PbI_3$ deposited on ITO/PEDOT:PSS working electrode under anodic conditions (black), the signal due to just ITO/PEDOT:PSS (green), and the difference of the two showing the signal of the $CH_3NH_3PbI_3$ layer (red). (c) The same as in (b), but under cathodic conditions. ……79

Figure A-3. Differential spectra for $CH_3NH_3PbI_3$ on Au normalized at 1580 nm to identify disparity between the anodic and cathodic charge accumulation conditions …….. 81

Figure A-4. GIXRD patterns of $CH_3NH_3PbI_3$ films on ITO/PEDOT:PSS substrates following DC spectroelectrochemical or DC + AC electromodulation measurements. Electrochemical measurements were made before removing each sample from the electrolyte solution, which were then dried at room temperature, all under an inert atmosphere, followed by GIXRD measurements. GIXRD measurements were performed under ambient atmospheric conditions. (110), (220), and (330) $CH_3NH_3PbI_3$ peaks are labeled on the pristine plot. ITO peaks are labeled with an asterisk (*). …… 82

Figure A-5. Comparison of NIR transient absorption spectra between a single layer $CH_3NH_3PbI_3$ and double layer PEDOT:PSS/$CH_3NH_3PbI_3$ film, both deposited on glass at (a) 2 ps and (b) 500 ps. Spectra are normalized to their high energy peak. …… 84

Figure A-6. (a) Electrotransmission spectra of $CH_3NH_3PbI_3$ after ITO/PEDOT:PSS background has been subtracted. (b) Transient absorption of $CH_3NH_3PbI_3$ film after washing in 0.1M $TBAPF_6$ dichloromethane solution. (c) Comparison of the sum of anodic and cathodic electrotransmission (blue) to transient absorption spectrum (black). (d) Comparison of ground state absorbance of $CH_3NH_3PbI_3$ deposited on glass before and after electrolyte wash. …… 85

Figure A-7. Fluence dependence for kinetics at 980 nm and 1500 nm in both the single layer $CH_3NH_3PbI_3$ (2-step preparation) and bilayer PEDOT:PSS/ $CH_3NH_3PbI_3$. …….….. 87

Figure B-1. (a) Transient absorption spectra normalized at the band edge bleach peak beginning at the peak of the push pulse overlap with the probe (t = 10.56 ps). (b) Fitting of the high energy portion of the bleach signal to a Boltzmann distribution. (c) Comparison of carrier temperature decay with push pulse fluence. …… 90

Figure B-2. Push pulse induced change in transient absorption kinetics for $CH_3NH_3PbI_3$ at (a) the band edge and (b) in the NIR. Solid lines represent monoexponential fits. Lifetimes for these fits are shown in (c). ……..……. 92

Figure B-3. Simulation of carrier dynamics for conduction band electron (n_e), valence band hole (n_h), and trapped electron (n_T) population. Dashed line indicates time delay for push pulse arrival in pump-push-probe measurements. ……. 93

Figure B-4. Normalized pump-push-probe kinetics at 1000 nm with (a) 1500 nm push pulse and (b) 1630 nm push pulses .……..……..……. 94

Figure B-5. (a) Comparison of excited state NIR transient absorption spectra for $CH_3NH_3PbI_3$ with (blue trace) and without (black trace) TOPO treatment. (b) Pump-push-probe kinetics at 1000 nm for a TOPO passivated $CH_3NH_3PbI_3$ sample comparing no push (black) and a 1500 nm push pulse (red).. ……. 95

Figure B-6. Raw kinetics for the low energy induced absorption at 778 nm and the band edge bleach at 732 nm for a (a) 905 nm, (b) 1100 nm, and (c) 1500 nm pump. (d) Kinetics for the band edge bleach normalized following decay of the fast component showing pump energy independent recombination. Red line shows monoexponential fit for 1100 nm data. …….……... 96

List of Tables

Table 3-1 Photodiode Fit Parameters ……... 43

Table 3-2 Model Parameters for Fitting Electron and Hole Species Associated Spectra …… 56

Table 3-3 Model Parameters for Fitting Electron Kinetics …….. 57

Table A-1 Integrated Area and Ratio of PbI_2 (001) Peak (12.8°) and $CH_3NH_3PbI_3$ (110) Peak (14.3°) …….. 83

Table A-2 Correlation Matrix for Fitting of Parameters for the SAS from Table 3-2 ……..… 89

Table A-3 Correlation Matrix for Parameters from Fitting the 1-step Electron Signal from Table 3-3 ……. 89

Table A-4 Correlation Matrix for Parameters from Fitting the 2-step Electron Signal from Table 3-3 ……..…… 89

“All we have to decide is what to do with the time that is given us”

-J.R.R Tolkien

Chapter 1: Introduction

1.1 Photovoltaic Impact on Global Power Production

The total global power consumption for 2018 was >18 TW.[1] The percentage of this power that was produced by solar power and other renewables was ~4%, whereas coal, natural gas, and oil accounted for ~85% (Figure 1-1). While the cost per unit power generated for solar has decreased to competitive levels with non-renewable sources, there are several factors leading to this disparity in power production including: variability in solar irradiation by location, storage requirements at night, and safe integration into the electric grid.[2]

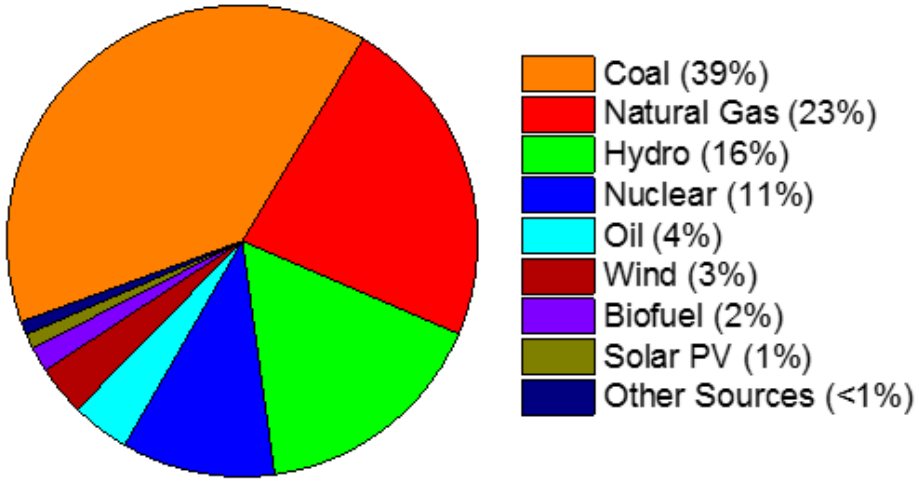

Figure 1-1. Global electricity generation by source as a percentage of total from 2015. Graph adapted from data made available by the International Energy Agency.[3]

The majority of this solar power production is done by large "solar farms" which generate power in the MW – GW range and can cover areas of up to 50 km^2.[4] While these large

installations are useful in specific locations with predictable amounts of solar irradiation, distributed PV resources (e.g. residential rooftop PV) also have potential to decrease reliance on non-renewable sources.[5] It has been estimated that 30% of the energy demand in Ontario, CA could be met by rooftop PV,[6] and the state of California has begun mandating a certain degree of solar electricity generation for new residential and commercial buildings.[7] Crystalline silicon (c-Si) photovoltaic modules are the main technology being utilized to produce this energy, but many other systems such as organic photovoltaics, GaAs, CIGS, CZTS, quantum dots, and perovskites are being explored.

To produce power on a meaningful scale an aspect that needs to be considered is the abundance and annual production of elements required for each PV technology. Out of the technologies with similar device efficiencies to c-Si, lead halide perovskites are the only competitor whose precursor element production will allow for large scale incorporation within a meaningful time period.[8] Due to the substantial capital investment in research and development as well as manufacturing infrastructure, along with current global supply chains,[5] it is unlikely a single technology will supplant c-Si in the near term. Rather it is likely technologies such as lead halide perovskites can serve to augment c-Si, in the form of tandem solar cells,[9] as well as explore other application spaces more well suited to thin films, such as photovoltachromic window incorporation into buildings and automobiles.[10-11]

For an incoming photovoltaic technology to make an impact on the market it must be cost competitive and show similar, if not greater, device performance than existing technologies. While purely inorganic systems, such as c-Si and CdTe, show relatively high efficiencies, they require high temperature processing to make high purity materials suitable to use in PV modules. Solution processable materials cut down on the cost of fabrication and allow for a wider array of

device architectures to be explored. Much effort in this regard has been put toward studying organic photovoltaics (OPVs), but these systems have so far been hindered by relatively low charge generation and extraction efficiencies. The knowledge gained from studying both inorganic and organic systems has led to hybrid organic-inorganic perovskites having a historic rise in efficiency with small scale, research laboratory devices nearly on par with their silicon counterparts.[12]

Already, more than a dozen firms are seeking to commercialize perovskite solar cells with aims ranging from small-scale printable, flexible cells to integration into Si tandem cells.[13] While perovskite devices have shown efficiencies comparable to Si issues of stability and longevity still need to be addressed.

1.2 Maturation of Perovskite Based PV Technologies

Hybrid organic-inorganic metal halide perovskites have seen a major increase in interest from the photovoltaic community since the seminal report by Kojima et al.[14] on the use of $CH_3NH_3PbI_3$ and $CH_3NH_3PbBr_3$ as a visible light absorbing layer in a dye-sensitized solar cell in 2009. Here the perovskite layer was coated on titanium dioxide which accepted photoexcited electrons, while an iodide/triiodide redox couple acted to shuttle holes to the cathode. This device architecture acted as a proof of concept, but would require iteration as the perovskite layer was found to readily degrade under illumination. Three years later, it was discovered that the liquid electrolyte in the DSSC could be replaced with an organic semiconductor layer, forming a fully solid state device, termed a meso-superstructured solar cell (MSSC).[15] While devices with this architecture are still studied today, mainstream adoption of perovskites by the photovoltaic community came after it was shown that their incorporation into planar heterojunction

architecture,[16] similar to organic photovoltaics, maintained high device performance and improved stability.

From the original report of ~3.8% efficiency, the evolution of device architecture has led to efficiencies >20% being reported by several groups for single junction thin film planar heterojunction devices.[17-19] While solar cells utilizing these materials have seen a drastic increase in device efficiency toward their theoretical limit of ~30%,[20] overcoming the hurdles to reach that limit will require greater understanding of the systems charge carrier dynamics, specifically the role of defects in unproductive recombination. A deeper understanding of the fundamental properties which make this performance possible will also lead to opportunities for incorporation into other photovoltaic applications including solar concentrators[21] and tandem cell architectures.[9]

With perovskite based solar cells proving their competitiveness with more widely commercialized photovoltaics, more research focus has been directed toward improving stability. The ability to solution process these films allows for controllable tuning of the final film composition. Chemical substitution at both the A- and X-sites, advanced in cell encapsulation, and the incorporation of surface passivating layers into device stacks have all been shown to help maintain device efficiency over extended periods of time.[22]

While reports of high device efficiencies initially led the community to think there were either low trap state densities or that the trap states present were non-detrimental to device performance, subsequent reports of rate constants for carrier dynamics in perovskite single crystals and increases in photoluminescence lifetime and intensity by treatment of thin films with Lewis bases have shown that trap states do influence charge carrier dynamics in these systems.[23] A more thorough understanding of the nature of trap states and their influence on both electron

and ion motion will be important for both stability and guiding engineering principles for perovskites based devices in a number of applications moving forward.

1.3 Characterization of Hybrid Organic-Inorganic Perovskites

Perovskites are defined by their ABX_3 structure. Here we will limit the discussion to those compositions relevant to photovoltaic applications, although similarly structured materials have been used for their superconducting[24] and ionic conductivity properties.[25] In this subclass of perovskites, the A site is a small organic or inorganic cation, typically methylammonium, formamidinium, or cesium; the B site is a cation in the +2 oxidation state, typically Pb or Sn, although some transition metals have been shown to form the perovskite structure as well; and the X site is a halide, where compositions with Br and I have been found to produce films resulting in the highest device performance.

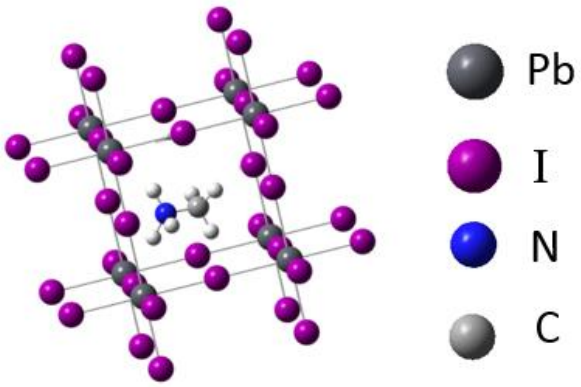

Figure 1-2. Representation of the cubic methylammonium lead iodide perovskite cubic structure.

Depending on the interaction of the A site cation with the BX_6 octahedra (see Figure 1-2), different crystal structures can form. This is an important as the perovskites crystal structure defines its optoelectronic properties. The structure which forms preferentially can be predicted

empirically using the Goldschmidt tolerance factor (t),[26] which is an empirically derived formula for the geometric ratio of the A, B, and X ionic radii. The ideal cubic structure forms for values of $0.9<t<1.0$.[27] Methylammonium lead iodide (t=0.95) has been one of the most highly studied A-site cations due to its stability in the cubic phase, whereas cesium lead iodide ($t<0.8$) and formamidinium lead iodide (t=1.03) form orthorhombic and hexagonal phases, respectively, although it has been found that alloys of the two can improve phase stability relative to either cation on their own. In-depth computational studies have shown that distortions of the pseudocubic structure have a strong impact on the material's electronic band structure, and therefore many of its optoelectronic properties, including band gap and carrier effective masses.[28]

One appealing aspect of perovskites, and a factor in the accessibility for so many research groups to be able to study this material over the past decade, is their relative ease of fabrication. Perovskite precursors can readily be dissolved in polar solvents, along with additives which can be used to tune their nucleation and crystal growth. These precursor solutions can then be spin-coated and annealed at relatively low temperatures, forming polycrystalline thin films suitable for use in a photovoltaic device. Several other fabrication methods have also been implemented to form perovskite films including chemical vapor deposition,[29] electrodeposition,[30] and dip coating.[31] While the ease of fabrication has led to a large interest in studying these materials, work that we have done (described in Chapter 3) along with work from other research groups,[32-33] has shown that the type of defects present in a film are dependent on the method of fabrication, making direct comparisons of device performance complicated. These studies show that strict control of fabrication conditions is necessary to reproducibly make high quality perovskite films.

The relationship between the perovskites structure and the properties which make it a good absorbing layer in photovoltaic cells is still not completely understood. The high absorption coefficient of most perovskite compositions implies these materials act as a direct band gap semiconductor, whose valence band maximum and conduction band minimum occur at the same momentum value (defined more thoroughly in Chapter 2). Indirect band gap materials, such as silicon, whose band extrema occur at different momentum values require a photon-phonon interaction during the absorption process and typically have lower absorption coefficients, but also exhibit longer charge carrier lifetimes. Despite their direct band gap nature, lead halide perovskites have been shown to exhibit a relatively long lived photoexcited state. A number of explanations for these carrier lifetimes have been given based on the fundamental properties of the system including large polaron formation,[34] phonon assisted recombination,[35] Rashba spin-orbit coupling,[36] and an inverse absorption process,[37] but the influence of trap states cannot be neglected as surface passivation treatments have been shown to improve these lifetimes.[23]

To properly understand carrier dynamics in this system, accurate calculations of the electronic structure of a material are necessary. Experimentally, observations of a high energy bleach signal and a broad induced absorption above the band gap from initial transient absorption studies[38] led to speculation that the optical response arose from transitions involving multiple valence and conduction bands (Figure 1-3). Several computational[39-40] and experimental[41-43] studies followed seeming to confirm the use of the multiband picture in modelling the electronic structure and charge carrier dynamics in these systems. Our findings[44] add to this multiband model, as we were able to characterize distinct valence and conduction band transitions in the photoexcited state. Proper fitting of the model to the recovery of the transient signal induced by photoexcitation back to the ground state ($\Delta A = 0$) allows for the relevant recombination kinetic

parameters (Figure 1-3c) to be calculated. While Auger and bimolecular rate constants are generally intrinsic to the material system,[45] the kinetics for Shockley-Read-Hall (SRH) recombination are dependent on the nature and energetics of trap states present in the sample being measured.

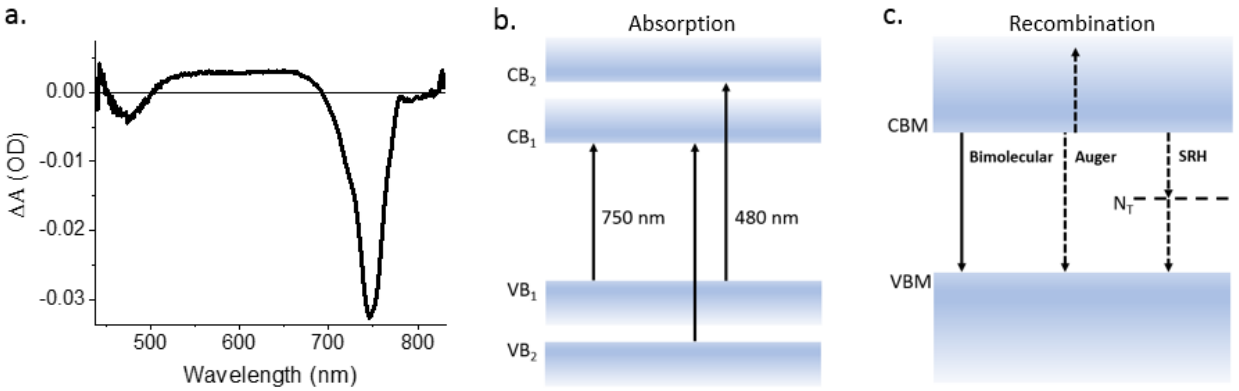

Figure 1-3. (a) Representative transient absorption of a $CH_3NH_3PbI_3$ thin film. (b) Proposed band structure resulting in band gap (750 nm) and higher energy (480 nm) bleaching. Arrows show transitions which are blocked following a resonant excitation pulse. (c) Radiative (solid black arrow) and non-radiative (dashed black line) excited state decay pathways between the conduction band minimum (CBM) and valence band maximum (VBM), which can be mediated through mid-gap trap states (N_T).

Energetically, deep level trap states in $CH_3NH_3PbI_3$ have experimentally been observed around 0.6-0.8 eV below the conduction band minimum.[46-47] Work focused on the nature of trap states in hybrid organic-inorganic perovskites has mainly consisted of computational studies. These studies typically differentiate trap states located at either the surface[48] or within the bulk of a grain.[49] The energy level associated with specific defects has been found to depend on the computational method used, but calculations generally find that bulk defects with energies within

the band gap are composed of interstitial iodine or iodine on methylammonium anti-site substitution, whereas surface defects are highly dependent on processing conditions and include undercoordinated lead in addition to iodine defects. Further studies on the nature and energetics of trap states, such as those presented in Chapter 4, are not only important in understanding these system's optoelectronic properties, but also to inform the means of passivation.

1.4 References

1. BP Statistical Review of World Energy 2019 **2019**.
2. Alboaouh, K. A.; Mohagheghi, S., Impact of Rooftop Photovoltaics on the Distribution System. *Journal of Renewable Energy* **2020,** *2020*, 4831434.
3. Agency, I. E., Data & Statistics. https://www.iea.org/data-and-statistics, 2015.
4. Fairley, P., The Pros and Cons of the World's Biggest Solar Park. *IEEE Spectrum* **2020**.
5. Woodhouse, M.; Smith, B.; Ramdas, A.; Margolis, R., Crystalline Silicon Photovoltaic Module Manufacturing Costs and Sustainable Pricing: 1H 2018 Benchmark and Cost Reduction Road Map. **2019**.
6. Wiginton, L. K.; Nguyen, H. T.; Pearce, J. M., Quantifying rooftop solar photovoltaic potential for regional renewable energy policy. *Computers, Environment and Urban Systems* **2010,** *34* (4), 345-357.
7. Weisenmiller, R. B.; Douglas, K.; Mcallister, A.; Hochschild, D.; Scott, J. A.; Bozorgchami, P.; Froess, L.; Meyer, C.; Ashuckian, D.; Bohan, D., 2019 Building Energy Efficency Standards. Commission, C. E., Ed. 2019.
8. Snaith, H. J., Present status and future prospects of perovskite photovoltaics. *Nat Mater* **2018,** *17* (5), 372-376.
9. Leijtens, T.; Bush, K. A.; Prasanna, R.; McGehee, M. D., Opportunities and challenges for tandem solar cells using metal halide perovskite semiconductors. *Nature Energy* **2018,** *3* (10), 828-838.
10. Cannavale, A.; Eperon, G. E.; Cossari, P.; Abate, A.; Snaith, H. J.; Gigli, G., Perovskite photovoltachromic cells for building integration. *Energy Environ. Sci.* **2015,** *8* (5), 1578-1584.
11. Lin, J.; Lai, M.; Dou, L.; Kley, C. S.; Chen, H.; Peng, F.; Sun, J.; Lu, D.; Hawks, S. A.; Xie, C.; Cui, F.; Alivisatos, A. P.; Limmer, D. T.; Yang, P., Thermochromic halide perovskite solar cells. *Nature Materials* **2018,** *17* (3), 261-267.
12. NREL Best Research-Cell Efficiency Chart. https://www.nrel.gov/pv/cell-efficiency.html (accessed 8/16/2020).
13. Extance, A., The reality behind solar power's next star material. *Nature* **2019,** (570), 429-432.
14. Kojima, A.; Teshima, K.; Shirai, Y.; Miyasaka, T., Organometal Halide Perovskites as Visible-Light Sensitizers for Photovoltaic Cells. *J. Am. Chem. Soc.* **2009,** *131* (17), 6050-+.
15. Lee, M. M.; Teuscher, J.; Miyasaka, T.; Murakami, T. N.; Snaith, H. J., Efficient hybrid solar cells based on meso-superstructured organometal halide perovskites. *Science* **2012,** *338* (6107), 643-7.
16. Docampo, P.; Ball, J. M.; Darwich, M.; Eperon, G. E.; Snaith, H. J., Efficient organometal trihalide perovskite planar-heterojunction solar cells on flexible polymer substrates. *Nature Communications* **2013,** *4* (1), 2761.

17. Saliba, M.; Matsui, T.; Domanski, K.; Seo, J. Y.; Ummadisingu, A.; Zakeeruddin, S. M.; Correa-Baena, J. P.; Tress, W. R.; Abate, A.; Hagfeldt, A.; Gratzel, M., Incorporation of rubidium cations into perovskite solar cells improves photovoltaic performance. *Science* **2016,** *354* (6309), 206-209.
18. Tsai, H.; Asadpour, R.; Blancon, J.-C.; Stoumpos, C. C.; Durand, O.; Strzalka, J. W.; Chen, B.; Verduzco, R.; Ajayan, P. M.; Tretiak, S.; Even, J.; Alam, M. A.; Kanatzidis, M. G.; Nie, W.; Mohite, A. D., Light-induced lattice expansion leads to high-efficiency perovskite solar cells. *Science* **2018,** *360* (6384), 67-70.
19. Jeon, N. J.; Na, H.; Jung, E. H.; Yang, T.-Y.; Lee, Y. G.; Kim, G.; Shin, H.-W.; Il Seok, S.; Lee, J.; Seo, J., A fluorene-terminated hole-transporting material for highly efficient and stable perovskite solar cells. *Nature Energy* **2018,** *3* (8), 682-689.
20. Shockley, W.; Queisser, H. J., Detailed Balance Limit of Efficiency of p-n Junction Solar Cells. *J. Appl. Phys.* **1961,** *32* (3), 510-519.
21. Lin, Q.; Wang, Z.; Snaith, H. J.; Johnston, M. B.; Herz, L. M., Hybrid Perovskites: Prospects for Concentrator Solar Cells. *Adv Sci (Weinh)* **2018,** *5* (4), 1700792.
22. Boyd, C. C.; Cheacharoen, R.; Leijtens, T.; McGehee, M. D., Understanding Degradation Mechanisms and Improving Stability of Perovskite Photovoltaics. *Chemical Reviews* **2019,** *119* (5), 3418-3451.
23. deQuilettes, D. W.; Koch, S.; Burke, S.; Paranji, R. K.; Shropshire, A. J.; Ziffer, M. E.; Ginger, D. S., Photoluminescence Lifetimes Exceeding 8 μs and Quantum Yields Exceeding 30% in Hybrid Perovskite Thin Films by Ligand Passivation. *ACS Energy Letters* **2016,** *1* (2), 438-444.
24. Collignon, C.; Lin, X.; Rischau, C. W.; Fauqué, B.; Behnia, K., Metallicity and Superconductivity in Doped Strontium Titanate. *Annual Review of Condensed Matter Physics* **2019,** *10* (1), 25-44.
25. Jun, A.; Kim, J.; Shin, J.; Kim, G., Perovskite as a Cathode Material: A Review of its Role in Solid-Oxide Fuel Cell Technology. *ChemElectroChem* **2016,** *3* (4), 511-530.
26. Goldschmidt, V. M., Die Gesetze Der Krystallochemie (The Laws of Cristallochemistry). *Naturwissenchaften* **1926,** *14*, 477-485.
27. Li, Z.; Yang, M.; Park, J.-S.; Wei, S.-H.; Berry, J. J.; Zhu, K., Stabilizing Perovskite Structures by Tuning Tolerance Factor: Formation of Formamidinium and Cesium Lead Iodide Solid-State Alloys. *Chem. Mater.* **2015,** *28* (1), 284-292.
28. Even, J.; Pedesseau, L.; Katan, C.; Kepenekian, M.; Lauret, J.-S.; Sapori, D.; Deleporte, E., Solid-State Physics Perspective on Hybrid Perovskite Semiconductors. *J. Phys. Chem. C* **2015,** *119* (19), 10161-10177.
29. Tavakoli, M. M.; Gu, L.; Gao, Y.; Reckmeier, C.; He, J.; Rogach, A. L.; Yao, Y.; Fan, Z., Fabrication of efficient planar perovskite solar cells using a one-step chemical vapor deposition method. *Scientific Reports* **2015,** *5* (1), 14083.
30. Chen, H.; Wei, Z.; Zheng, X.; Yang, S., A scalable electrodeposition route to the low-cost, versatile and controllable fabrication of perovskite solar cells. *Nano Energy* **2015,** *15*, 216-226.
31. Adnan, M.; Lee, J. K., All Sequential Dip-Coating Processed Perovskite Layers from an Aqueous Lead Precursor for High Efficiency Perovskite Solar Cells. *Scientific Reports* **2018,** *8* (1), 2168.
32. Meggiolaro, D.; Motti, S. G.; Mosconi, E.; Barker, A. J.; Ball, J.; Perini, C. A. R.; Deschler, F.; Petrozza, A.; De Angelis, F., Iodine chemistry determines the defect tolerance of lead-halide perovskites. *Energy Environ. Sci.* **2018,** *11* (3), 702-713.
33. Camargo, F. V. A.; Nagahara, T.; Feldmann, S.; Richter, J. M.; Friend, R. H.; Cerullo, G.; Deschler, F., Dark Subgap States in Metal-Halide Perovskites Revealed by Coherent Multidimensional Spectroscopy. *J. Am. Chem. Soc.* **2019**.
34. Zhu, H.; Miyata, K.; Fu, Y.; Wang, J.; Joshi, P. P.; Niesner, D.; Williams, K. W.; Jin, S.; Zhu, X. Y., Screening in crystalline liquids protects energetic carriers in hybrid perovskites. *Science* **2016,** *353* (6306), 1409-1413.

35. Hutter, E. M.; Gelvez-Rueda, M. C.; Osherov, A.; Bulovic, V.; Grozema, F. C.; Stranks, S. D.; Savenije, T. J., Direct-indirect character of the bandgap in methylammonium lead iodide perovskite. *Nat Mater* **2017,** *16* (1), 115-120.
36. Etienne, T.; Mosconi, E.; De Angelis, F., Dynamical Origin of the Rashba Effect in Organohalide Lead Perovskites: A Key to Suppressed Carrier Recombination in Perovskite Solar Cells? *J. Phys. Chem. Lett.* **2016,** *7* (9), 1638-45.
37. Davies, C. L.; Filip, M. R.; Patel, J. B.; Crothers, T. W.; Verdi, C.; Wright, A. D.; Milot, R. L.; Giustino, F.; Johnston, M. B.; Herz, L. M., Bimolecular recombination in methylammonium lead triiodide perovskite is an inverse absorption process. *Nat. Commun.* **2018,** *9* (1), 293.
38. Xing, G.; Mathews, N.; Sun, S.; Lim, S. S.; Lam, Y. M.; Gratzel, M.; Mhaisalkar, S.; Sum, T. C., Long-range balanced electron- and hole-transport lengths in organic-inorganic $CH_3NH_3PbI_3$. *Science* **2013,** *342* (6156), 344-7.
39. Even, J.; Pedesseau, L.; Katan, C., Analysis of Multivalley and Multibandgap Absorption and Enhancement of Free Carriers Related to Exciton Screening in Hybrid Perovskites. *J. Phys. Chem. C* **2014,** *118* (22), 11566-11572.
40. Umebayashi, T.; Asai, K.; Kondo, T.; Nakao, A., Electronic structures of lead iodide based low-dimensional crystals. *Phys. Rev. B* **2003,** *67* (15), 155405.
41. Endres, J.; Egger, D. A.; Kulbak, M.; Kerner, R. A.; Zhao, L.; Silver, S. H.; Hodes, G.; Rand, B. P.; Cahen, D.; Kronik, L.; Kahn, A., Valence and Conduction Band Densities of States of Metal Halide Perovskites: A Combined Experimental-Theoretical Study. *J. Phys. Chem. Lett.* **2016,** *7* (14), 2722-9.
42. Anand, B.; Sampat, S.; Danilov, E. O.; Peng, W.; Rupich, S. M.; Chabal, Y. J.; Gartstein, Y. N.; Malko, A. V., Broadband transient absorption study of photoexcitations in lead halide perovskites: Towards a multiband picture. *Phys. Rev. B* **2016,** *93* (16), 161205.
43. Leguy, A. M.; Azarhoosh, P.; Alonso, M. I.; Campoy-Quiles, M.; Weber, O. J.; Yao, J.; Bryant, D.; Weller, M. T.; Nelson, J.; Walsh, A.; van Schilfgaarde, M.; Barnes, P. R., Experimental and theoretical optical properties of methylammonium lead halide perovskites. *Nanoscale* **2016,** *8* (12), 6317-27.
44. Pollock, T. P.; Schlenker, C. W., Electromodulation and Transient Absorption Spectroscopy Suggest Conduction Band Electron Lifetime, Electron Trapping Parameters, and CH3NH3PbI3 Solar Cell Fill Factor Are Correlated. *J. Phys. Chem. C* **2019,** *123* (30), 18160-18170.
45. Herz, L. M., Charge-Carrier Dynamics in Organic-Inorganic Metal Halide Perovskites. *Annu. Rev. Phys. Chem.* **2016,** *67*, 65-89.
46. Heo, S.; Seo, G.; Lee, Y.; Lee, D.; Seol, M.; Lee, J.; Park, J.-B.; Kim, K.; Yun, D.-J.; Kim, Y. S.; Shin, J. K.; Ahn, T. K.; Nazeeruddin, M. K., Deep level trapped defect analysis in $CH_3NH_3PbI_3$ perovskite solar cells by deep level transient spectroscopy. *Energy Environ. Sci.* **2017,** *10* (5), 1128-1133.
47. Baumann, A.; Vath, S.; Rieder, P.; Heiber, M. C.; Tvingstedt, K.; Dyakonov, V., Identification of Trap States in Perovskite Solar Cells. *J. Phys. Chem. Lett.* **2015,** *6* (12), 2350-4.
48. Uratani, H.; Yamashita, K., Charge Carrier Trapping at Surface Defects of Perovskite Solar Cell Absorbers: A First-Principles Study. *J. Phys. Chem. Lett.* **2017,** *8* (4), 742-746.
49. Du, M. H., Density Functional Calculations of Native Defects in $CH_3NH_3PbI_3$: Effects of Spin-Orbit Coupling and Self-Interaction Error. *J. Phys. Chem. Lett.* **2015,** *6* (8), 1461-6.

Chapter 2: Background

2.1 Device Physics

2.1.1 Device performance metrics

Photovoltaic device performance is defined by a device's efficiency in converting light energy, in the form of photons, into electrical current, in the form of electrons, and is given by the following equation,

$$\eta(\%) = \frac{V_{OC} I_{SC} FF}{P_{in}} \qquad (2.1)$$

where V_{OC} is the voltage at open circuit, I_{SC} is the photocurrent at short circuit, FF is the fill factor, and P_{in} is the power input from the incident light. Following will be a brief discussion of these metrics and the factors affecting them.

Short circuit photocurrent is the electrical current passing through a cell when the voltage is zero. The density of carriers being generated is dependent on the amount of light being absorbed and thus it is more common to report photocurrent density (J_{SC}) to account for the area of the device being illuminated. The power and spectrum of incident light is also standardized to allow for comparison between devices made by different research groups and to more accurately reflect performance under average solar illumination conditions (AM 1.5G) on the Earth's surface. As the efficiency of photocurrent generation is dependent on both the material's absorption properties and the wavelength of incident light, a typical method for standardizing this measurement is to perform external quantum efficiency measurements, which is a ratio of charge carriers collected by the solar cell to the number of incoming photons, on both the device

of interest and a calibrated reference diode, followed by correction for the spectral mismatch factor (M),[1]

$$M = \frac{\int_a^b E_{SIM}(\lambda) SR^{UN}(\lambda) d\lambda \int_a^b E_{REF}(\lambda) SR^{RC}(\lambda) d\lambda}{\int_a^b E_{REF}(\lambda) SR^{UN}(\lambda) d\lambda \int_a^b E_{SIM}(\lambda) SR^{RC}(\lambda) d\lambda} \tag{2.2}$$

where a and b are the range of spectral response, E_{SIM} is the simulator spectral irradiance, E_{REF} is the reference spectral irradiance, SR^{UN} is the spectral response of the uncalibrated cell, and SR^{RC} is the spectral response of the reference cell. Each integral is equal to the current for the specific cell under simulator or reference spectral irradiance. Substituting current (I) for each integral gives,

$$I_{REF}^{UN} = \frac{I_{SIM}^{UN}}{M} \frac{I_{REF}^{RC}}{I_{SIM}^{RC}} \tag{2.3}$$

which allows for the current to be corrected for in an uncalibrated device.

For a net photocurrent to be generated, excited electrons must persist long enough to diffuse to selective contacts and be collected in an external circuit. Therefore, any process which increases recombination of electrons and holes, such as the presence of mid-gap trap states, can decrease the overall photocurrent produced by a cell. Recombination in this manner also has a pronounced effect on open circuit voltage and fill factor due to changes in carrier's quasi-Fermi levels.

A device's open circuit voltage is the maximum available voltage that a cell is able to sustain, when there is no net current flowing under illumination. This voltage arises due to the difference in quasi fermi level of charge carriers as they are extracted from the cell and is dependent on the materials used as well as the device architecture. Open circuit voltage with respect to band gap (E_g) can be expressed as,[2]

$$eV_{OC} = E_g - k_B T \ln \frac{N_C N_V}{np} \tag{2.4}$$

where k_B is Boltzmann's constant, T is temperature, N_C and N_V are the density of states for the conduction and valence bands, which are partially occupied by electrons with concentration n and hole concentration p. This implies that as the relative concentrations n and p increase, the open circuit potential approaches the material's band gap.

Output power from a cell depends on the product of voltage and current, which implies that a device at either short circuit or open circuit will produce no power. At some applied bias between short and open circuit a device will have its maximum power output with respective current (I_M) and voltage (V_M). The fill factor (FF) of a device is defined as,

$$FF = \frac{I_M V_M}{I_{SC} V_{OC}} \tag{2.5}$$

This parameter is often described as measuring the "squareness" of a cell's current-voltage response. Deviations from ideality occur due to a number of factors including the cell's series and parallel resistances. Series resistance is the resistance to current flow in the absorbing layer as well as at interfaces within the device. This parameter can be influenced by both traps in the bulk of the intrinsic layer, as well as at the surface/interfaces. Increasing series resistance leads to decreases in fill factor. Parallel resistance occurs due to leakage of current through the cell and at the edges of the device. High parallel resistance thus contributes to high fill factors. As this parameter is most often influenced by the device fabrication process, care must be taken to ensure proper contacts, especially in the case of solution processed layers.

2.1.2 Carrier Dynamics

The main operating principle behind photovoltaic devices is the conversion of light into electricity. The first step in this process is the absorption of light by one or more semiconductor layers within the device. The probability of light being absorbed is dependent on both the material and the wavelength of light. This interaction is typically quantified by the absorption coefficient (α),

$$\alpha = \frac{4\pi k}{\lambda} \tag{2.6}$$

where k is the extinction coefficient and λ is the wavelength.

Disregarding trap states for the moment, for light to be absorbed it must have energy equal to or greater than the band gap of the material, which is the difference in energy between the valence band maximum and conduction band minimum. Light with energy greater than the band gap will be absorbed with some probability along with the joint density of states between the valence and conductions bands. Rewriting the expression for absorption coefficient to account for these states results in,

$$\alpha(h\nu) = A\sum P_{if} n_i n_f \tag{2.7}$$

where A is a pre-factor, P_{if} is the probability for a transition between the initial and final states, n_i is the density of electrons in the initial state, and n_f is the density of available final states.[3]

The result of light absorption is the formation of either a free electron and free hole, or a bound electron-hole pair, known as an exciton. Which species forms is dependent on the properties of the material, namely the relative permittivity, also known as the dielectric constant (ε), as well as the reduced masses of the electron and hole. Relative permittivity is an intrinsic property to each specific material and defines the Coulomb force between two point charges in the material relative to that in vacuum. Exciton binding energy, based on the hydrogen-like model, is then given by

$$\Delta E_{exc} = -\frac{m_r e^4}{2\hbar^2 (4\pi\varepsilon\varepsilon_0)^2}\frac{1}{n^2} \qquad (2.8)$$

where m_r is the reduced effective mass.[4] If there is enough energy present in the system, such as the thermal energy available at room temperature (k_BT = 26 meV at 300K), then the dominant photoexcited species will be free electron and holes. For $MAPbI_3$, exciton binding energies have been measured to be on the order of 10-50 meV, with more recent studies pointing toward the lower end of that range, implying the dominant photoexcited species in these systems consists of free carriers.[5]

Free carrier recombination within the perovskite layer occurs mainly through three mechanisms: bimolecular, trap-assisted, and Auger. Bimolecular recombination occurs when two charge carriers recombine and corresponding energy is released in the form of a photon or phonon. Trap-assisted recombination occurs when an electron or hole is first localized in a trap state prior to recombining with a free carrier. While trap mediated carrier recombination is generally non-radiative in nature, trap state emission has been shown to occur in certain systems.[6-7] Auger recombination is a 3-body process where the excess energy from the recombination of an electron and hole is transferred to a third carrier which is typically a third carrier, but can also be a phonon.

A simple model for describing the rate of relaxation from these three processes can be written as follows:

$$\frac{dN}{dt} = -k_1 N - k_2 N^2 - k_3 N^3 \qquad (2.9)$$

Here k_1 is the rate constant associated with non-radiative, or trap assisted recombination, and depends on either the electron or hole density (N). The bimolecular recombination rate constant

k_2 depends on both electron and hole carrier densities. The Auger recombination rate k_3 is dependent on N^3 as the energy of two carriers recombining is transferred to a third carrier.

For an ideal absorbing material used in a photovoltaic device carrier recombination should proceed through the bimolecular pathway, with no contribution from trap states or the Auger process. In typical inorganic semiconductors the bimolecular recombination rate constant is intrinsic to the system, although various effects such as photon reabsorption can complicate the determination of this parameter.[8]

For the production of photocurrent carriers must be extracted from the absorbing layer. This requires a carrier to be transported, either by diffusion or drift under the influence of an electric field, to its specific selective interface prior. In planar heterojunction devices of either n-i-p or p-i-n configurations (Figure 2-1), an electric field exists due to the gradient introduced by differences in the materials ionization potentials and electron affinities. Additionally, a carrier density gradient exists due to the asymmetric composition of the contacts which serves to enhance the photocurrent. The rate for charge transfer by necessity needs to outcompete that of the recombination processes for photocurrent to be generated.

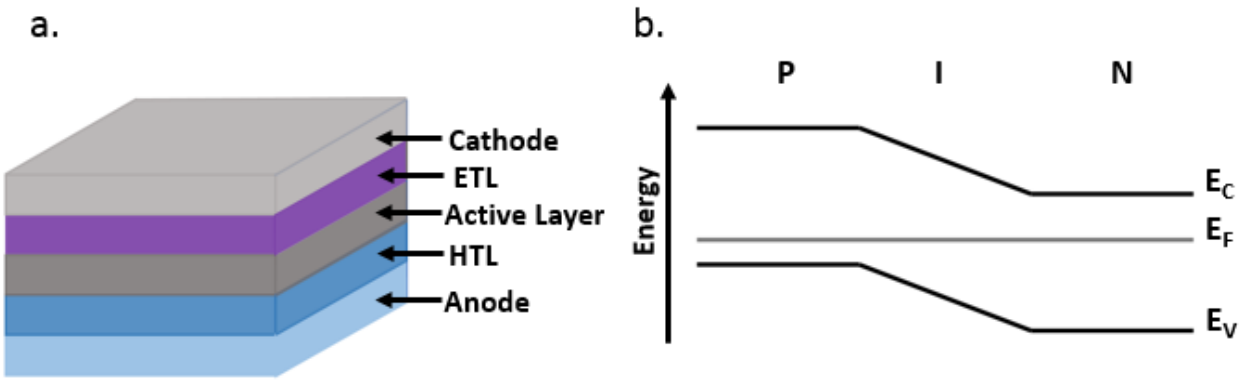

Figure 2-1. (a) Planar heterojunction device architecture showing the active (intrinsic) layer in between an electron transport layer (ETL) and hole transport layer (HTL). (b) Band profile for a p-i-n interface showing the influence of an electric field over the intrinsic layer.

The typical means for determining whether a given material will operate as a selective contact for either electron or hole extraction is by comparing the electron affinity and ionization potential, obtained from ultraviolet photoelectron spectroscopy and photoemission spectroscopy, for the contact material to that of the light absorbing layer. For a contact to be selective it must have energy levels which allow for transfer of one carrier while restricting transport of the oppositely charged carrier (i.e. an electron acceptor should have a higher ionization potential than the light absorbing layer to block hole transfer).

While techniques which measure a devices current-voltage response under illumination are important in defining overall performance metrics, typically other methods are required to gain deeper insight into the fundamental photophysics of a material. Time-resolved changes in absorption or photoluminescence intensity can be used to study the dynamics of a systems photoexcited state. The spectral changes which arise during these measurements are often due to a number of overlapping features arising from various possible transitions. Therefore, it is often

necessary to use complementary techniques, such as electromodulation spectroscopy, to characterize individual contributions to the excited state spectra.

2.2 Electromodulation Spectroscopy

Electromodulation spectroscopy is a specialized spectroelectrochemical technique which utilizes an alternating current to apply an electric field to a sample and measure the spectral response compared to that of the ground state. This section will describe the electronic band structure of semiconductors and how to interpret electromodulation spectroscopy in this context.

2.2.1 Electronic Band Structure

A brief description of the electronic band structure of a semiconductor will now be given to aid in the interpretation of spectroelectrochemical measurements. Rather than the discrete states which are present in molecular systems, the extended interaction of atomic orbitals in a crystalline solid lead to an energetic distribution of states, which is known as a band. In an ideal, undoped semiconductor, the valence band is composed of fully occupied states while the conduction band is the next highest energy unoccupied band of states.

Band diagrams are presented in momentum space. The relationship between the kinetic energy (E) of an electron and its momentum ($\hbar k$) is given by,

$$E = \frac{k^2 \hbar^2}{2m^*} \tag{2.10}$$

where m^* is the electron effective mass. Efficient photon absorption requires conservation of photon energy and electron momentum. The probability for this process decreases if there is a change in the electrons momentum as the photon absorption needs to couple to either absorption or emission of a phonon. The difference in energy between the valence band maximum and

conduction band minimum is known as the band gap. When these values occur at the same k value, the material is said to have a direct band gap, whereas if they occur at different values the material is said to have an indirect band gap. Lead halide perovskites are generally accepted to have a direct band gap,[9-11] so the following discussion will focus on the characteristics of direct band gap systems and the influence of this electronic structure on a material's absorption properties and carrier dynamics.

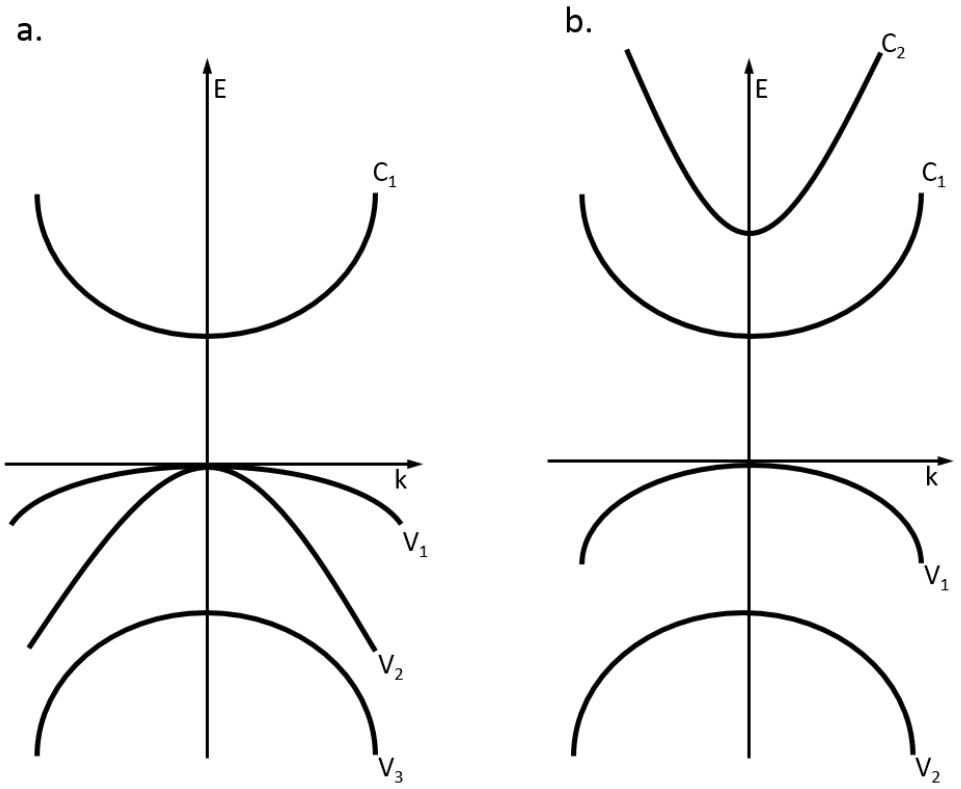

Figure 2-2. Band diagram for direct band gap semiconductor systems with split valence bands (a) and split conduction bands (b).

Theoretical calculations for the band structure around the valence and conduction bands have been studied in depth for III-V semiconductors and metals such as germanium.[12-15] One defining feature of these systems is the presence of sub-bands which form in the valence band

due to spin orbit interactions (Figure 2-2a.). Here V_1 is the heavy-hole band, V_2 is the light hole band, and V_3 is the split-off band. Transitions between these three bands were first observed by altering the Fermi level through doping,[16] although these transitions have also been observed through transient absorption measurements.[17]

In the case of Pb based hybrid perovskites, where the conduction band is formed from the overlap of Pb 6p and the halide 5p and 5s orbitals,[18-19] spin orbit coupling results in a splitting of the conduction band (Figure 2-2b, C_1 and C_2). The valence band, which for lead iodide systems consists of Pb 6s-I 5p σ-antibonding orbitals, does not exhibit the overlap that exists at k=0 in the valence band of III-V semiconductors.

A material's linear absorption spectrum is determined by the joint density of states between the valence and conductions bands. Typically, these transitions are dominated by contributions from states near the valence band maximum and conduction band minimum, but for systems that exhibit large density of states away from k=0, such as lead halide perovskites, the absorption spectrum is broadened.

Filling of states by charge carriers due to photoexcitation,[20] doping,[21] or an applied bias[14] result in perturbations to the system's absorption. Phase-space filling (Burstein-Moss shift) and band gap renormalization will be discussed in detail in the subsequent transient absorption section. The main transitions which will be focused on in the following section are due to an applied bias introducing a population of electrons in the conduction band or a population of holes in the valence band.

2.2.2 Electromodulation Experimental Methods and Data Analysis

Electrochemical measurements entail monitoring some change in the electrochemical system with respect to a change in applied voltage or current at the working electrode. The application of this applied voltage (or current) results in a change in the system's absorption properties due to an alteration of the electric field or a change in band population (oxidation state for molecular systems).

Experimental setups for spectroelectrochemical measurements range in complexity due to intricacies in sample preparation, as well as integration of the electrochemical cell with the probe source and detection system. A standard three electrode cell includes a working electrode, which applies voltage or current to the system, a counter electrode which compensates the cell's charge, and a reference electrode which allows for comparison between measurements. For bulk semiconductor films, the film itself can be used as the working electrode if the material's conductivity is high enough,[22] or the film can be directly deposited on an optically transparent electrode.[23]

Determining the energetics for electron transfer in solid state systems is complex compared to molecular systems.[24] In the latter case, the Nernst equation can reliably be used to calculate the reduction and oxidation potentials for species in solution. For solid state systems, the magnitude of band bending, as well as the presence of mid-gap states, will determine the potential onset of both cathodic and anodic current flow. Due to this effect, the difference between these potential onsets, sometimes referred to as the electrochemical band gap, will typically be smaller than the optical band gap. Additional complications arise in attempting to analyze band structure from potential step measurements, as processes such as corrosion will

lead to current being passed which doesn't correspond to filling of either valence or conduction band states.

In electromodulation spectroscopy, the applied electric field is modulated by the use of alternating current. In the case where no carriers are injected, the amplitude of the AC perturbation in relation to the band gap determines the response of the system, and can be separated into three ranges based on the relative strength of the applied electric field (ε): Low range, where the invariant spectral line shape scales as ε^2, intermediate range, where Franz-Keldysh oscillations begin to complicate the line shape and the fundamental absorption edge shows an exponential dependence on ε, and the high range, which is characterized by Stark shifts of energy bands and breakdown of selection rules.[25] For analysis of the effect of an applied electric field on the fundamental absorption edge, care must be taken that the applied AC field does not inject carriers.[14] However in the work presented in Chapter 3, the applied bias is chosen specifically to populate carriers in either the valence or conduction band. A population of electrons in the conduction band (Figure 2-2, C_1) introduces transitions to higher lying, unoccupied states ($C_1 \rightarrow C_2$). Similarly, a population of holes in the valence band allows for transitions from lower lying occupied states to the vacant band edge ($V_2 \rightarrow V_1$).

The ability for electromodulation spectroscopy to characterize individual electron and hole transitions allows for improved modeling of excited state dynamics involving these transitions. This type of characterization becomes necessary in transient absorption measurements, whose spectra often result from multiple overlapping features.

2.3 Multi-pulse Laser Spectroscopy

Transient absorption spectroscopy has been an instrumental tool in the study of some of the underlying fundamental photophysics of hybrid organic-inorganic perovskites which have led to high photovoltaic device performance. This method utilizes two laser pulses, the first pulse electronically excites the sample and, after some time delay, the second pulse probes the transmission properties of the excited state. Due to innovations in supercontinuum generation, broad band probe pulses can be generated spanning the UV into the infrared. Monitoring how these excited state spectral features change over time allows for the calculation of kinetic parameters corresponding to the recombination pathways in the system. Following will be a discussion of observed phenomena in typical semiconductor excited state features and of the insight transient absorption has provided into the electronic structure and carrier dynamics in hybrid organic-inorganic perovskites.

2.3.1 Transient Absorption Spectroscopy

For a material to exhibit a transient absorption signal requires a change in the absorption properties of the excited state in comparison to the ground state. Transient absorption spectra are typically plotted as the change in absorption (ΔA) or change in transmission normalized by the overall transmission (-ΔT/T) and is calculated by,

$$\Delta A(\lambda, t) = A(\lambda, t_1) - A(\lambda, t_0) \qquad (2.11)$$

where t_0 refers to absorption prior to photoexcitation. This implies that the ΔA signal for excited state species is positive, whereas loss of ground state absorption results in a negative signal (bleach).

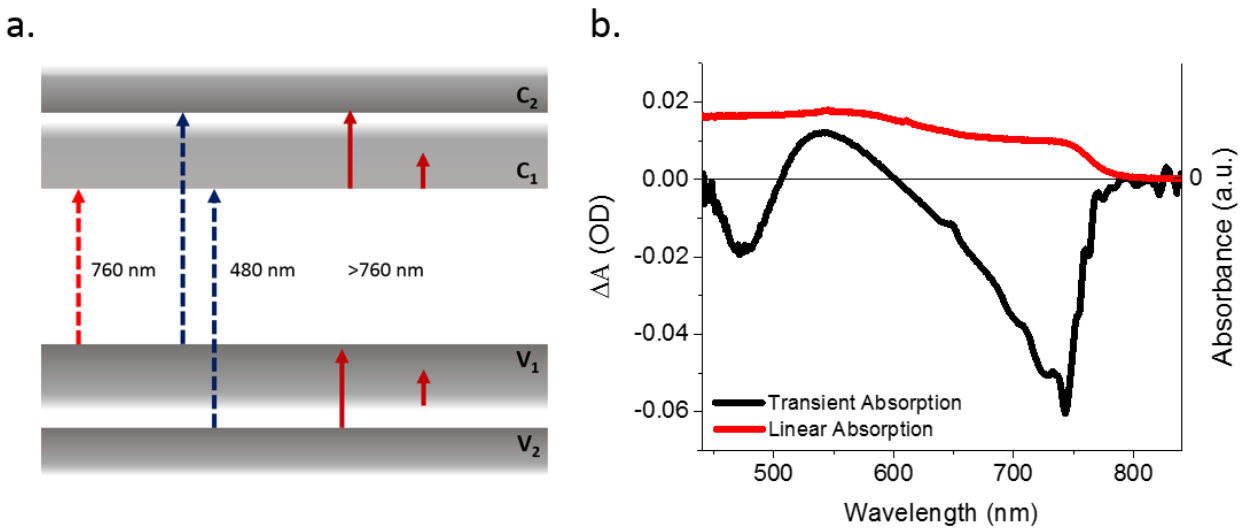

Figure 2-3. (a) Energy level schematic showing the transitions leading to bleaching and induced absorptions observable in $CH_3NH_3PbI_3$ transient absorption measurements. Dashed lines correspond to bleaching and solid lines correspond to induced absorptions. (b) Transient (black) and linear (red) absorption spectra of $CH_3NH_3PbI_3$.

Several different excited state species can form which result in induced absorptions. Neglecting changes which occur near the band edge for the moment, the two main excited state species which can influence semiconductor transient absorption spectra are excitons and free carriers. Each of these species has characteristic features and recombination kinetics which can be used to differentiate their nature. Exciton absorption typically occurs at energies below the band gap and decay monoexponentially, except at high fluences. Free carriers spectral features include both inter- and intraband transitions. Interband transitions occur due to excitation of carriers to higher lying bands and follow similar rules to valence to conduction band transitions. Intraband transitions involve transitions within the same band and typically are characterized by

a monotonic absorption which increases as λ^p, where $1.5 < p < 3.5$ and depends on the type of ionized impurity or phonon modes present which are required for momentum conservation.[3]

There are a few reports of the lead halide excited state showing excitonic properties,[26] but due to more recent in-depth studies showing exciton binding energies lower than the thermal energy available at room temperature and modeling of photoluminescence decay[27] and transient absorption ground state recovery,[28] the main photoexcited species in these systems appears to be free carriers. Intraband transitions for these carriers have been observed,[29-30] although these features may overlap with low energy polaron absorption.[31-32] Our work, discussed in Chapter 3, was the first to show that higher energy interband transitions were observable in transient absorption measurements.

Bleaching, or negative ΔA, spectral features occur due to an increased number of photons reaching the detector in the excited state measurement compared to the ground state. The most obvious energy range this occurs in is that around the band gap as electrons are excited by the pump pulse from the valence band to the conduction band. Stimulated emission can also result in a greater number of photons reaching the detector leading to bleaching. Depending on the magnitude of the material's Stokes shift, the PL bleaching can overlap with that of the band edge.[33]

Many of the initial transient absorption studies on perovskites focused on dynamics near the material's band edge. Three mechanisms have been observed to effect where the bleaching onset occurs in perovskites; the Burstein-Moss effect,[34] band gap renormalization,[35] and the optical stark effect.[36] These effects will now be discussed briefly due to their importance in analysis presented in Chapters 3 and 4.

The Burstein-Moss effect, or phase-space filling, is observed in transient absorption measurements due to changes in electron density in the conduction band and hole density in the valence band induced by the pump pulse. Depending on the energy and intensity of the pump pulse, some distribution of each photoexcited carrier population is present in their respective bands resulting in bleaching in the transient absorption spectra. In lead halide perovskites, at early times following photoexcitation by a resonant pump pulse, the energetic distribution of carriers leads to a broad bleach feature which sharpens as carriers thermally equilibrate toward the band edge.[34] Carriers with excess energy have been observed to persist on the ~100 ps timescale in lead halide perovskite films.[32] This slow carrier cooling has been attributed to the "hot phonon bottleneck" effect, in which the type of phonon modes available do not allow for carriers to rapidly lose energy within a band.

Band gap renormalization results in a decrease in band gap as a function of carrier density due to exchange and correlation effects.[37] This can be understood as for carriers in an electron-hole plasma, Coulomb energies act to attract other carriers of opposite charge and repel carriers of like charge. If carriers were completely randomly distributed then these attractive and repulsive forces would cancel each other out and there would be no change in the system's band gap with respect to carrier density. For a real system, the exchange energy increases the average distance between the electrons with parallel spin resulting in a decrease in their repulsive Coulomb energy and a lowering of the total energy of the system. Additionally, the correlation energy for an electron-hole pair system can act to lower the system's energy even further, as a hole will have a higher probability to be found in the vicinity of an electron compared with a second electron. As a material's band gap is reduced, new transitions become allowed at sub-band gap energies, resulting in the appearance of induced absorptions at energies between the

unperturbed and renormalized band gap. This feature decays as carriers equilibrate to these new energy levels blocking the band edge transition.

The optical Stark effect (OSE) is analogous to the stark effect observed due to the application of an electric field by varying potential in an electrochemical cell, only here the electric field is due to a non-resonant photon field. The electric field acts to shift exciton transition energy which results in changes to absorption near the band edge. The magnitude of the shift (δE) is dependent on several factors given by the equation:

$$\delta E = \frac{(\mu_{0X})^2 \langle F \rangle^2}{\Delta} \qquad (2.12)$$

where μ_{0X} is the transition dipole moment, $\langle F \rangle$ is the time averaged electric field, and Δ is the difference in energy between between the exciton resonance and the pump excitation energy.[36] As δE is dependent on the transition dipole moment, the optical stark effect only arises when specific selection rules are met. For $CH_3NH_3PbI_3$ the conduction and valence band edge states have a total angular momentum of ½, and the allowed transitions are for $\Delta m_j = \pm 1$. Polarization selectivity for OSE in this system then implies that circularly polarized light with spin magnetic quantum number $m_S = \pm 1$ will couple with the respective exitonic state of $m_j = \pm 1$. For the case of measuring a system with linear polarized light, $\sigma+$ and $\sigma-$ are present in equal amounts implying OSE can be observed under appropriate conditions.

In $CH_3NH_3PbI_3$, the OSE acts to increase the energy of the excitonic transition from that in the ground state, resulting in an induced absorption at this energy and bleaching at the unperturbed excitonic transition energy. The magnitude of the change in absorbance (ΔA) can be approximated by the following equation:

$$\Delta A = -\frac{1}{2} \frac{\partial A_{ex}}{\partial \hbar \omega} \bullet \delta E \qquad (2.13)$$

where A_{ex} is the absorption spectrum of the excitonic transition and ħω is the probe photon energy. Since the square of the electric field is linearly dependent on the intensity of the laser pulse, this implies that the change in absorbance is also linearly dependent on the laser intensity.

More recent studies on lead halide perovskites, including those conducted in our group, have shown that sub-gap bleaching can be observed due to valence-to-trap state transitions induced by the pump pulse.[38-39] This implies that electron traps exist in these films and gives information on the energy level difference between the valence band and the trap state. Knowledge of the type of carrier a trap acts on is important as photovoltaic device performance is dependent on both electrons and holes being transported out of the perovskite layer. The type of trap present also informs the means of passivation, as different methods are required to passivate filled versus unfilled trap states. As will be discussed more in depth in Chapter 4, surface treatments with Lewis bases leads to removal of low energy, sub gap bleaching in certain perovskite films, implying the trap state is electron poor.

One method of deconvoluting overlapping spectral features from transient absorption measurements which have different kinetic profiles is global analysis.[40-41] In performing global analysis, one assumes the overall spectrum is a superposition of spectral features arising from different components which have their own time-dependent concentrations ($c_l(t)$) and spectra ($\varepsilon_l(\lambda)$).

$$\Psi(\lambda,t) = \sum_{l}^{n_{comp}} c_l(t)\varepsilon_l(\lambda) \qquad (2.14)$$

Mathematically, the concentration of each component is assumed to be a linear combination of exponential decays signified by the parameter θ. When specific assumptions are made to test a hypothesis, this method is known as target analysis.[42] Here each spectral component is called a species associated spectrum (SAS).

$$\Psi(\lambda,t) = \sum_{l}^{n_{comp}} c_l^{SAS}(t,\theta) SAS_l(\lambda) \qquad (2.15)$$

The number of spectrally and temporally independent components comprising the data set can either be predetermined, as is the case in target analysis, or can be determined by performing singular value decomposition (SVD). Adding more components to a model will lead to a better fit to the data, but these components will not necessarily have any physical meaning. SVD is a matrix factorization technique which is based on any m x n matrix having a singular value decomposition of the form:

$$\Psi_{m\times n} = U_{m\times m} S_{m\times n} W_{n\times n} \qquad (2.16)$$

where U and W are orthogonal matrices containing the left and right singular vectors, respectively, and S is a matrix which only has values on its diagonal. For a time resolved spectral data set, the left singular vectors represents the time dependence of each component, and the right singular vectors represent the spectral dependence. As the number of components used to model the data set increases, the singular values decrease and the right and left singular vectors become less distinct from noise.

2.3.2 Pump-Push-Probe Spectroscopy

Transient absorption spectroscopy is typically a two pulse technique where the pump pulse excites the system and a probe pulse monitors changes in the spectral response compared to the ground state absorption. Pump-push-pulse is a transient absorption technique wherein a third pulse is added to the experiment to “push” the excited state at some time following the pump pulse. The energy of the push pulse along with the relative populations and allowable transitions of the excited state determines the observable response of the system.

Pump-push-probe studies on lead halide perovskite systems have been limited. Lim et al.[43] used this technique to study the barrier for hot carrier charge transfer between $CH_3NH_3PbI_3$ and an electron accepting material (bphen). In this study they determined that despite an energy offset of ~0.9 eV between the conduction band of $CH_3NH_3PbI_3$ and the LUMO of bphen, a push pulse >1.98 eV was required for efficient hot carrier charge transfer. They interpreted that this excess energy was required due to the formation of a Schottky barrier between the two materials and that this result must be taken into account when choosing materials for designing a hot carrier solar cell.

Hopper et al.[44] used pump-push-probe to study hot carrier relaxation in a series of perovskite compositions. Here they used a 2.6 eV pump, a 0.6 eV push, and a 0.6 eV probe. To analyze their data, they used a two level model consisting of the "hot" and "cold" states. They observed that HC cooling dynamics depended on the HC density as well as the organic (or inorganic) cation present. These observations imply that HC cooling in lead halide perovskites operates by the hot phonon bottleneck mechanism. Further work by these authors has provided evidence for carrier-carrier interactions as well as carrier-phonon interactions influencing hot carrier dynamics.[45]

Neither of these works took the presence of sub-gap states into account for their kinetic analysis. Our work, as discussed in Chapter 4, uses pump-push-probe to study trapping kinetics in $CH_3NH_3PbI_3$. Here we use the tuneability of our push pulse to promote electrons trapped in mid-gap states back into the conduction band and monitor the resulting kinetics. The energy difference between sub gap bleaching and the band edge transition allowed us to approximate the push energy required to delocalize trapped electrons. Using a push pulse with lower energy allows for hot carrier dynamics to be differentiated from carrier trapping dynamics.

2.4 References

1. Osterwald, C. R., Translation of device performance measurements to reference conditions. *Solar Cells* **1986,** *18* (3), 269-279.
2. Tress, W.; Yavari, M.; Domanski, K.; Yadav, P.; Niesen, B.; Correa Baena, J. P.; Hagfeldt, A.; Graetzel, M., Interpretation and evolution of open-circuit voltage, recombination, ideality factor and subgap defect states during reversible light-soaking and irreversible degradation of perovskite solar cells. *Energy Environ. Sci.* **2018,** *11* (1), 151-165.
3. Pankove, J. I., *Optical Processes in Semiconductors*. Dover Publications, Inc.: New York, N.Y., 1971.
4. Seeger, K., *Semiconductor Physics, An Introduction*. Springer: New York, 1997.
5. Miyata, A.; Mitioglu, A.; Plochocka, P.; Portugall, O.; Wang, J. T.-W.; Stranks, S. D.; Snaith, H. J.; Nicholas, R. J., Direct measurement of the exciton binding energy and effective masses for charge carriers in organic–inorganic tri-halide perovskites. *Nature Physics* **2015,** *11* (7), 582-587.
6. Motti, S. G.; Gandini, M.; Barker, A. J.; Ball, J. M.; Srimath Kandada, A. R.; Petrozza, A., Photoinduced Emissive Trap States in Lead Halide Perovskite Semiconductors. *ACS Energy Letters* **2016,** *1* (4), 726-730.
7. Flatae, A. M.; Tantussi, F.; Messina, G. C.; De Angelis, F.; Agio, M., Plasmon-Assisted Suppression of Surface Trap States and Enhanced Band-Edge Emission in a Bare CdTe Quantum Dot. *J. Phys. Chem. Lett.* **2019,** *10* (11), 2874-2878.
8. Crothers, T. W.; Milot, R. L.; Patel, J. B.; Parrott, E. S.; Schlipf, J.; Muller-Buschbaum, P.; Johnston, M. B.; Herz, L. M., Photon Reabsorption Masks Intrinsic Bimolecular Charge-Carrier Recombination in CH3NH3PbI3 Perovskite. *Nano Lett.* **2017,** *17* (9), 5782-5789.
9. Even, J.; Pedesseau, L.; Katan, C.; Kepenekian, M.; Lauret, J.-S.; Sapori, D.; Deleporte, E., Solid-State Physics Perspective on Hybrid Perovskite Semiconductors. *J. Phys. Chem. C* **2015,** *119* (19), 10161-10177.
10. Mosconi, E.; Etienne, T.; De Angelis, F., Rashba Band Splitting in Organohalide Lead Perovskites: Bulk and Surface Effects. *J. Phys. Chem. Lett.* **2017,** *8* (10), 2247-2252.
11. Richter, J. M.; Chen, K.; Sadhanala, A.; Butkus, J.; Rivett, J. P. H.; Friend, R. H.; Monserrat, B.; Hodgkiss, J. M.; Deschler, F., Direct Bandgap Behavior in Rashba-Type Metal Halide Perovskites. *Advanced Materials* **2018,** *30* (52), 1803379.
12. Kahn, A. H., Theory of the Infrared Absorption of Carriers in Germanium and Silicon. *Phys. Rev.* **1955,** *97* (6), 1647-1652.
13. Bottka, N.; Johnson, D. L., Theory of band-population effects in electroreflectance. *Phys. Rev. B* **1975,** *11* (8), 2969-2978.
14. Bottka, N.; Johnson, D. L.; Glosser, R., Band-population interference phenomena in the electroreflectance of narrow-gap semiconductors under heavy surface accumulation. *Phys. Rev. B* **1977,** *15* (4), 2184-2194.
15. Seraphin, B. O.; Bottka, N., Band-Structure Analysis from Electro-Reflectance Studies. *Phys. Rev.* **1966,** *145* (2), 628-636.
16. Briggs, H. B.; Fletcher, R. C., New Infrared Absorption Bands in p-Type Germanium. *Phys. Rev.* **1952,** *87* (6), 1130-1131.
17. Ganikhanov, F.; Burr, K. C.; Tang, C. L., Ultrafast dynamics of holes in GaAs probed by two-color femtosecond spectroscopy. *Appl. Phys. Lett.* **1998,** *73* (1), 64-66.
18. Umebayashi, T.; Asai, K.; Kondo, T.; Nakao, A., Electronic structures of lead iodide based low-dimensional crystals. *Phys. Rev. B* **2003,** *67* (15), 155405.

19. Endres, J.; Egger, D. A.; Kulbak, M.; Kerner, R. A.; Zhao, L.; Silver, S. H.; Hodes, G.; Rand, B. P.; Cahen, D.; Kronik, L.; Kahn, A., Valence and Conduction Band Densities of States of Metal Halide Perovskites: A Combined Experimental-Theoretical Study. *J. Phys. Chem. Lett.* **2016,** *7* (14), 2722-9.
20. Juodawlkis, P. W.; Ralph, S. E., Hole-induced transient bandgap renormalization: A mechanism for photo-induced absorption in defect-engineered semiconductors. *Appl. Phys. Lett.* **2000,** *76* (13), 1722-1724.
21. Walsh, A.; Da Silva, J. L. F.; Wei, S.-H., Origins of band-gap renormalization in degenerately doped semiconductors. *Phys. Rev. B* **2008,** *78* (7), 075211.
22. Venkateswara Rao, A.; Chazalviel, J. N.; Ozanam, F., In-situ characterization of the n-Si/acetonitrile interface by electromodulated infrared internal-reflection spectroscopy. *J. Appl. Phys.* **1986,** *60* (2), 696-706.
23. Shallcross, R. C.; Zheng, Y.; Saavedra, S. S.; Armstrong, N. R., Determining Band-Edge Energies and Morphology-Dependent Stability of Formamidinium Lead Perovskite Films Using Spectroelectrochemistry and Photoelectron Spectroscopy. *J. Am. Chem. Soc.* **2017,** *139* (13), 4866-4878.
24. Bisquert, J.; Cendula, P.; Bertoluzzi, L.; Gimenez, S., Energy Diagram of Semiconductor/Electrolyte Junctions. *J. Phys. Chem. Lett.* **2014,** *5* (1), 205-7.
25. Aspnes, D. E., Third-Derivative Modulation Spectroscopy with Low-Field Electroreflectance. *Surface Science* **1973,** *37* (1), 418-442.
26. Zhai, Y.; Sheng, C. X.; Zhang, C.; Vardeny, Z. V., Ultrafast Spectroscopy of Photoexcitations in Organometal Trihalide Perovskites. *Adv. Funct. Mater.* **2016,** *26* (10), 1617-1627.
27. Stranks, S. D.; Burlakov, V. M.; Leijtens, T.; Ball, J. M.; Goriely, A.; Snaith, H. J., Recombination Kinetics in Organic-Inorganic Perovskites: Excitons, Free Charge, and Subgap States. *Physical Review Applied* **2014,** *2* (3).
28. Trinh, M. T.; Wu, X.; Niesner, D.; Zhu, X. Y., Many-body interactions in photo-excited lead iodide perovskite. *J. Mater. Chem. A* **2015,** *3* (17), 9285-9290.
29. Narra, S.; Chung, C. C.; Diau, E. W.; Shigeto, S., Simultaneous Observation of an Intraband Transition and Distinct Transient Species in the Infrared Region for Perovskite Solar Cells. *J. Phys. Chem. Lett.* **2016,** *7* (13), 2450-5.
30. Munson, K. T.; Grieco, C.; Kennehan, E. R.; Stewart, R. J.; Asbury, J. B., Time-Resolved Infrared Spectroscopy Directly Probes Free and Trapped Carriers in Organo-Halide Perovskites. *ACS Energy Letters* **2017,** *2* (3), 651-658.
31. Munson, K. T.; Kennehan, E. R.; Doucette, G. S.; Asbury, J. B., Dynamic Disorder Dominates Delocalization, Transport, and Recombination in Halide Perovskites. *Chem* **2018,** *4* (12), 2826-2843.
32. Niesner, D.; Zhu, H.; Miyata, K.; Joshi, P. P.; Evans, T. J.; Kudisch, B. J.; Trinh, M. T.; Marks, M.; Zhu, X. Y., Persistent Energetic Electrons in Methylammonium Lead Iodide Perovskite Thin Films. *J. Am. Chem. Soc.* **2016,** *138* (48), 15717-15726.
33. Yakunin, S.; Protesescu, L.; Krieg, F.; Bodnarchuk, M. I.; Nedelcu, G.; Humer, M.; De Luca, G.; Fiebig, M.; Heiss, W.; Kovalenko, M. V., Low-threshold amplified spontaneous emission and lasing from colloidal nanocrystals of caesium lead halide perovskites. *Nature Communications* **2015,** *6* (1), 8056.
34. Manser, J. S.; Kamat, P. V., Band filling with free charge carriers in organometal halide perovskites. *Nat. Photonics* **2014,** *8* (9), 737-743.
35. Price, M. B.; Butkus, J.; Jellicoe, T. C.; Sadhanala, A.; Briane, A.; Halpert, J. E.; Broch, K.; Hodgkiss, J. M.; Friend, R. H.; Deschler, F., Hot-carrier cooling and photoinduced refractive index changes in organic-inorganic lead halide perovskites. *Nat. Commun.* **2015,** *6*, 8420.
36. Yang, Y.; Yang, M.; Zhu, K.; Johnson, J. C.; Berry, J. J.; van de Lagemaat, J.; Beard, M. C., Large polarization-dependent exciton optical Stark effect in lead iodide perovskites. *Nature Communications* **2016,** *7* (1), 12613.

37. Zimmerman, R., Many Particle Theoryf Highly Excited Semiconductors. *Teubner Texte Phys.* **1988**.
38. Pollock, T. P.; Schlenker, C. W., Electromodulation and Transient Absorption Spectroscopy Suggest Conduction Band Electron Lifetime, Electron Trapping Parameters, and CH3NH3PbI3 Solar Cell Fill Factor Are Correlated. *J. Phys. Chem. C* **2019,** *123* (30), 18160-18170.
39. Camargo, F. V. A.; Nagahara, T.; Feldmann, S.; Richter, J. M.; Friend, R. H.; Cerullo, G.; Deschler, F., Dark Subgap States in Metal-Halide Perovskites Revealed by Coherent Multidimensional Spectroscopy. *J. Am. Chem. Soc.* **2019**.
40. Snellenburg, J. J.; Laptenok, S. P.; Seger, R.; Mullen, K. M.; van Stokkum, I. H. M., Glotaran: A Java-Based Graphical User Interface for the R Package TIMP. *J. Stat. Softw* **2012,** *49* (3), 1-22.
41. Manger, L. H.; Rowley, M. B.; Fu, Y.; Foote, A. K.; Rea, M. T.; Wood, S. L.; Jin, S.; Wright, J. C.; Goldsmith, R. H., Global Analysis of Perovskite Photophysics Reveals Importance of Geminate Pathways. *J. Phys. Chem. C* **2017,** *121* (2), 1062-1071.
42. Williams, R. M.; Van Anh, N.; van Stokkum, I. H., Triplet formation by charge recombination in thin film blends of perylene red and pyrene: developing a target model for the photophysics of organic photovoltaic materials. *J Phys Chem B* **2013,** *117* (38), 11239-48.
43. Lim, S. S.; Giovanni, D.; Zhang, Q.; Solanki, A.; Jamaludin, N. F.; Lim, J. W. M.; Mathews, N.; Mhaisalkar, S.; Pshenichnikov, M. S.; Sum, T. C., Hot carrier extraction in CH₃NH₃PbI₃ unveiled by pump-push-probe spectroscopy. *Science Advances* **2019,** *5* (11), eaax3620.
44. Hopper, T. R.; Gorodetsky, A.; Frost, J. M.; Müller, C.; Lovrincic, R.; Bakulin, A. A., Ultrafast Intraband Spectroscopy of Hot-Carrier Cooling in Lead-Halide Perovskites. *ACS Energy Letters* **2018,** *3* (9), 2199-2205.
45. Hopper, T. R.; Jeong, A.; Gorodetsky, A.; Krieg, F.; Bodnarchuk, M. I.; Huang, X.; Lovrincic, R.; Kovalenko, M. V.; Bakulin, A. A., Kinetic Modeling of carrier cooling in lead halide perovskite materials. *arXiv:1912.05354 [physics.app-ph]* **2019**.

Chapter 3: Probing Electron and Hole Dynamics in Lead Iodide Perovskites

This chapter contains the work published originally in "Electromodulation and Transient Absorption Spectroscopy Suggest Conduction Band Electron Lifetime, Electron Trapping Parameters, and $CH_3NH_3PbI_3$ Solar Cell Fill Factor Are Correlated" by Pollock, T.P; Schlenker, C.W., in the Journal of Physical Chemistry C 2019, 123 (30), 18160-18170 **DOI:** 10.1021/acs.jpcc.9b02748

3.1 Introduction

The optoelectronic properties of metal halide-based perovskite materials, such as methylammonium lead iodide ($CH_3NH_3PbI_3$), have recently received renewed interest. This resurgence is largely due to the relative ease with which these materials can be cast as solvent-borne thin films to achieve solid-state devices with solar cell power conversion efficiencies exceeding 20%.[1] Their intriguing charge carrier dynamics, including long carrier lifetimes and large absorption oscillator strengths,[2] slow carrier cooling,[3] and rapid large-polaron formation[4-5] also make metal halide perovskites compelling candidates for a number of applications including lasers,[6] LEDs,[7] solid state lighting,[8] and spintronics.[9] Identifying the spectral signatures for charge carriers in optoelectronic materials is an important step in understanding their dynamic behavior, which in turn is critically important for device engineering. In the case of hybrid organic-inorganic perovskite-based devices, where the highest performing photovoltaic devices utilize the perovskite layer as the light-absorbing semiconducting layer between electron-selective and hole-selective contacts, efficient charge generation and extraction is necessary for optimal device efficiency and stability. While device stability issues such as current-voltage hysteresis have mainly been attributed to ionic migration, it has been postulated that some

contribution is due to the presence of interface defect sites, accompanied by charge carrier trapping.[10-11] Improvements in device efficiency and reduction in hysteresis have been rationalized through minimizing the barrier for charge extraction and passivating surface trap sites by optimizing the interface between the perovskite active layer and the charge transporting layers,[12] although direct measurement of the dynamics of specific charge carriers have not yet been experimentally achieved.

The study of charge extraction from a perovskite layer to a charge selective contact has mainly been limited to monitoring the recovery of the ground-state following photoexcitation by methods such as transient absorption spectroscopy[13-14] and photoluminescence lifetime measurements.[15] An alternative method of studying charge carrier dynamics in these systems is time-resolved microwave conductivity,[16-17] which monitors the lifetime of mobile carriers following photoexcitation. One limitation inherent to these methods is that they provide little information about the selectivity of charge collection at the perovskite-charge extraction layer interface, which is an important consideration in limiting undesired recombination. Analysis of the ground-state recovery of $CH_3NH_3PbI_3$ through transient absorption measurements focusing on the dynamics around the band-edge is additionally complicated by processes which influence both the spectral shape and dynamics of the excited state, such as photoinduced changes in reflectivity,[18] stimulated emission,[13] electroabsorption,[19] and band filling effects.[20] Electronic structure calculations on $CH_3NH_3PbI_3$ have been important in understanding the nature of both ground- and excited-state optical transitions, specifically showing the relatively large effect of spin-orbit coupling on the splitting of conduction and valence band states.[21-23] These calculations along with transient absorption measurements,[13, 24] UV photoemission spectroscopy,[25] and low temperature absorption[26] show that the energy level differences relevant to charge carrier

interband transitions to be ~1.0-1.2 eV for the conduction bands and ~0.9-1.0 eV for the valence bands. Resolving these energetically separated spectral features would report on the charge carrier dynamics of electrons and holes independently.

While a number of studies have investigated the kinetics of $CH_3NH_3PbI_3$ band edge recovery, few have exploited photoinduced NIR absorption.[14, 27, 28] In principal, the absorption signatures for electrons and holes in the NIR region could provide detailed kinetic insight if one could identify discernably unique features for positive and negative charge carriers. Spectroelectrochemistry has been an invaluable tool in characterizing charge carrier spectra in a number of systems relevant to photovoltaic devices.[29-32] However, the instability of hybrid organic-inorganic perovskites, which is exacerbated when they are immersed in polar solvents, has hindered the spectral characterization of charge carriers in this system by such methods.[33-35] Consequently, it is compelling to consider an electromodulation technique which utilizes an AC bias to overcome corrosion processes that occur under common DC-mode electrolysis. Here we show that mitigating film degradation while acquiring spectra under AC electrochemical anodic and cathodic potentials can be a practical way to obtain perovskite charge carrier spectra.

Assigning distinct electron and hole absorption spectra may also provide insight in to charge trapping processes. Trap assisted recombination typically proceeds through mid-gap states, whose densities are highly dependent on the film fabrication method for perovskites.[36] Two of the more widely utilized fabrication methods are commonly referred to as the "**1-step** deposition," were the precursor lead and organic salts are dissolved along with any additives in the same solution prior to spin-coating, and the "**2-step** deposition" which consists of sequential deposition of the lead halide layer followed by either dipping the lead halide covered substrate into an organic salt solution or spin-casting the organic salt solution onto the lead halide covered

substrate. Typically, devices fabricated using the **1-step** deposition method have shown higher efficiencies than those fabricated using the **2-step** method but the limited number of studies directly comparing the two methods have not shown a direct correlation between device performance, charge carrier kinetics, and trap state density.[37-38]

In this study, we demonstrate that the improved performance resulting from the **1-step** compared to the **2-step** fabrication for $CH_3NH_3PbI_3$ correlates with fewer electron traps and longer electron lifetimes. We utilize electromodulation spectroscopy to characterize electron and hole NIR spectral features under charge accumulation conditions, and NIR transient absorption spectroscopy to monitor the dynamics of these carriers. In our electromodulation measurements we apply an AC perturbation to drive charge accumulation in the perovskite film while monitoring changes in the intensity of either reflected or transmitted probe light using phase-sensitive detection methods. This electromodulation technique appears to preserve the stability of the $CH_3NH_3PbI_3$-electrolyte interface during the measurement and we observe negligible film degradation post-data collection. This stability contrasts markedly with typical corrosion processes that occur during more common DC spectroelectrochemical electrolysis measurements. Assigning these charge carrier spectra allows us to build a kinetic model to extract separate rate constants for electron and hole trapping, recombination, and extraction. Through model simulations we are also able to correlate an increase in the lifetime of conduction band electrons for the **1-step** perovskite deposition method with a decrease in the density of trap states. A greater fundamental understanding of charge carrier dynamics in these systems is not only important to increasing device efficiencies, but is also critical to improving device operational stability.

3.2 Experimental Methods

Materials & Physicochemical Studies: Unless otherwise stated, all materials were purchased from Sigma Aldrich and used without further purification. Methylammonium iodide (MAI) was synthesized by dropwise addition of hydroiodic acid (10 mL) to methylamine (24 mL) in ethanol in an ice bath. This solution was stirred for 2 hours and then the solvent was evaporated at 100°C, leaving white crystals. The crude product was then recrystallized twice using the mixed solvent technique with EtOH and ether at an ~7:1 ratio, and then isolated by vacuum filtration. The crystals were dried overnight in a vacuum oven at 100°C prior to further use.

Film thicknesses were measured with a Bruker OM-DektakXT profilometer. Grazing incidence X-ray diffraction (GIXRD) patterns were collected on a Bruker D8 Discover system with a Pilatus 2-D detector, using Cu Kα radiation (λ = 1.5418 Å).

Device Fabrication: Devices for both 1- and 2-step deposition methods were fabricated using a procedure modified from that published by Xiao.[39] Indium tin oxide (ITO, TFD Inc.) slides were cleaned sequentially in detergent (Micro-90), acetone, and isopropanol. For the **2-step** procedure, 460mg PbI_2 (99.999%) was dissolved in 1mL dry DMF (Alfa Aesar 99.8%) by stirring at 100°C overnight. PEDOT:PSS (Clevios) was sonicated for ~30 minutes prior to spin coating at 5000 rpm for 50 s followed by annealing at 120°C for 15 minutes in air. PbI_2 was then spin coated from the DMF solution heated to 70°C onto substrates also heated to the same temperature at 4000rpm for 40 s. After the PbI_2 layer was allowed to dry for ~20 minutes, MAI was spin coated from a 45 mg/mL solution in isopropyl alcohol at 4000 rpm for 25 s followed by annealing at 100°C in air. $PC_{71}BM$ was then spin coated from a 20 mg/mL solution in dry chlorobenzene at 1000 rpm for 30 s. The sample was then solvent-annealed by adding a drop (~10 uL) of dry chlorobenzene to a Petri dish, overnight in air. Ca (20 nm) and Al (100 nm) were then thermally

evaporated through a shadow mask to form electron-collecting contacts. For the **1-step** deposition, all parameters from the **2-step** method were conserved, with the exception of the perovskite deposition step. Therein a 30 wt% precursor solution in DMF was prepared with 3.06:1 $Pb(OAc)_2 \bullet 3H_2O$ (99.99%) to MAI ratio and 3 μL of hypophosphorous acid (50 wt% in H_2O). Spin coating for this step was performed under a N_2 atmosphere.

Device testing: The J-V characteristics of planar heterojunction perovskite solar cells were measured in a nitrogen atmosphere under one-sun illumination (AM1.5G, 100 mW/cm^2) with a Solar Light Co. 16S-300 solar simulator referenced with a calibrated Si photodiode. The solar cell was masked to an area of 0.0122 cm^2. Scans were made from reverse to forward bias and no light soaking or pre-biasing was performed prior to J-V measurements. EQE measurements were taken on a home-built optical table, with the output of a halogen lamp routed through a monochromator and focused on to the masked device. Current output was measured with a pre-amplifier connected to a lock-in amplifier. Lamp power output and EQE was referenced to a calibrated Si photodiode for visible-NIR measurements (350-950 nm) and the longer wavelength NIR response (950-1600 nm) was normalized to the visible with the vendor responsivity from a dual band Si/InGaAs photodiode (Thorlabs DSD2).

Electromodulation Measurements: All electrochemical measurements were made in an air-tight three electrode cell with a Ag wire as a quasi-reference and a Pt counter electrode, in a 0.1 M tetrabutylammonium hexafluorophosphate ($TBAPF_6$) dichloromethane electrolyte solution, which was assembled under an inert atmosphere. The working electrode was $CH_3NH_3PbI_3$ deposited on either a thin layer of gold (30 nm) on top of a titanium adhesion layer (20 nm) on a glass substrate or PEDOT:PSS (30 nm)-coated ITO. Potentials were referenced to the ferrocene/ferrocenium (Fc/Fc^+) redox couple. The AC waveform was generated with a function

generator (Agilent 33210A) which was routed through a potentiostat (Autolab PGSTAT302N) to control the potential of the electrochemical cell. The output of the function generator was frequency locked to a lock-in amplifier (Stanford Research Systems SR830). The output of a halogen lamp was routed through a monochromator and focused down on the working electrode, before being refocused into a dual band Si/InGaAs photodetector (Thorlabs DSD2). The probe beam was aligned normal to the working electrode for transmission mode measurements and at a 45° for the reflection mode measurements. The photodetector output was routed through a pre-amplifier (Stanford Research Systems SR570), and then split to a sourcemeter (Keithley 2400) and the lock-in amplifier.

Transient Absorption: All transient absorption measurements were made on samples prepared on glass substrates and encapsulated within an Ar-filled glovebox.

The 800nm output (pulse duration ~50 fs, repetition rate 1 kHz) from a Ti:sapphire laser system (Coherent, Libra) was used to generate both pump and probe beams for transient absorption measurements. This output is split using a 75/25 beam splitter with the higher-intensity beam directed into the optical parametric amplifier (Coherent OPerA) for pump pulse generation, while the lower intensity beam was used for probe white light generation.

For probe beam generation, the Ti:sapphire output was focused onto a sapphire crystal. A variable reflective ND filter attenuates the beam and splits it into a probe beam which passes through the sample before reaching the detector and a reference beam which does not interact with the sample and is routed to a separate detector. The change in transmittance of the sample is measured with a spectrometer coupled to a 256 pixel InGaAs sensor. An 850 nm long pass filter was placed in front of the sample to attenuate excess 800nm light. A mechanical chopper (500 Hz) was used to collect pump on-pump off measurements.

Surface Xplorer software (Ultrafast Systems) was used to collect the absorption spectra and OriginLab OriginPro 9.1.0 was used to process, analyze, and plot the data. Custom scripts for modeling kinetic data were written in Origin C. Each system of ordinary differential equations was solved using Runge-Kutta methods.

Target analysis was performed to obtain relevant species associated spectra using Glotaran software.[40]

3.3 Results and Discussion

The fill factor values for the devices fabricated from the **1-step** (FF= 0.74) process are markedly higher than those of the **2-step** (FF= 0.69) device fabrication process (Figure 3-1a). Fitting the current-voltage characteristics of each type of device to a simplified non-ideal diode equation $V = n * \frac{k_B T}{q} * \ln(\left(\frac{J+J_{ph}}{J_s}\right) + 1) + (J * R_{sa})$ (Figure A-1) shows that the reverse bias saturation current density (J_S), ideality factor (n), and photocurrent density (J_{ph}) are comparable between the two fabrication methods (Table 3-1), while the specific series resistance is approximately 3 times larger for the **2-step** device (R_{SA} = 0.88 Ω cm^2) than that of the **1-step** (R_{SA} = 0.32 Ωcm^2). These results suggest suppressed charge recombination in devices assembled with the **1-step** fabrication method, which can occur due to a decrease in the localization of charge carriers in trap states within the absorbing layer or at an interface. While external quantum efficiency (EQE) measurements are typically used to probe the efficiency of photon to current conversion at energies above the band gap of a material, absorption from deep level trap states can also be observed as photocurrent in response to sub-gap illumination in some cases. We observe weak sub-gap EQE in the NIR spectral region in the **2-step** sample that is not present in the **1-step** sample (Figure 3-1b). The density of sub-gap states here is ~4-5 orders of

magnitude lower than those above the band gap. The decreased fill factor and NIR photocurrent we observe for the **2-step** method indicates that there may be spectrally resolvable trap states in the NIR spectral region.

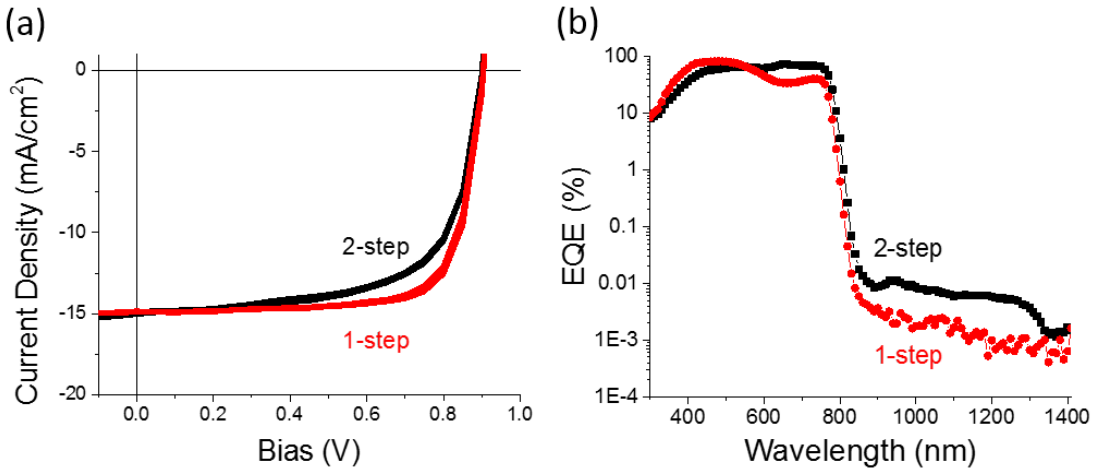

Figure 3-1. Current-voltage (a) and EQE (b) comparison between representative devices made with either the one step perovskite deposition (red traces) and two step deposition procedure (black traces).

Table 3-1. Photodiode Fit Parameters

Sample	**J_S[a] (nA/cm^2)**	**n[b]**	**R_{SA}[c] (Ωcm^2)**	**J_{ph}[d] (mA/cm^2)**
1-step	6.0 ± 5.5	2.2 ± 0.8	0.32 ± 0.28	15.5 ± 0.2
2-step	6.7 ± 4.3	2.2 ± 0.8	0.88 ± 0.31	15.1 ± 0.1

[a]Reverse bias saturation current density
[b]Ideality factor
[c]Specific series resistance
[d]Photocurrent density

To determine whether we could resolve the difference between the two sample preparations leading to the low energy photocurrent generating states, we utilized transient

absorption spectroscopy (Figure 3-2). Following excitation by a 650 nm pump pulse, we observe a broad induced absorption in the **1-step** sample, whereas the **2-step** sample shows a weak negative ΔA signal (bleach) between induced absorption features. Bleaching in the NIR spectrum of $CH_3NH_3PbI_3$ has previously been attributed to the presence of trap states,[41] although induced absorptions have also been observed in samples prepared using alternate fabrication methods.[14, 27] We postulated that the nature of the defect, as well as the density of defect states, likely depend on the method of fabrication. As we discuss in more detail in subsequent sections, we attribute the induced absorptions to the presence of photogenerated charge carriers.

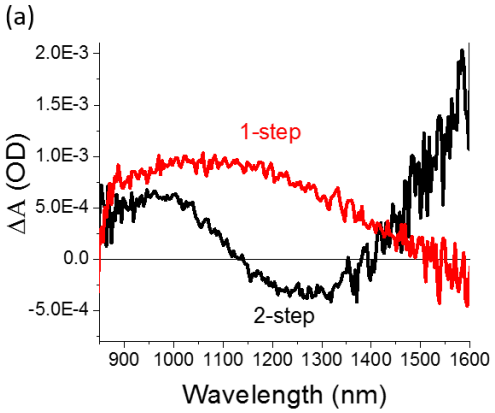

Figure 3-2. Transient absorption spectra for 1-step and 2-step $CH_3NH_3PbI_3$ samples on glass at 2.5 ps with a pump wavelength of 650nm.

We utilized electromodulation spectroscopy to better understand the origin of the observed induced absorption features in our NIR TA spectra. All electrochemical measurements were made on films fabricated with the **2-step** method. Prior to collecting the spectra of $CH_3NH_3PbI_3$ films under charge accumulation conditions, we performed cyclic voltammetry to determine the potential onset for anodic and cathodic current (Figure 3-3a). Dichloromethane was chosen as an electrolyte solvent for electrochemical measurements due to its chemical potential window, as well as the relative stability of the $CH_3NH_3PbI_3$ film. The cyclic

voltammograms shown here were measured with 200 mV/s sweep rates as to limit degradation during the measurement. We observe the onset of cathodic current at -0.8 V (vs. Fc/Fc^+) and anodic current at 0.1 V (vs. Fc/Fc^+) for a $CH_3NH_3PbI_3$ film deposited on a gold working electrode. This electrochemical potential range between anodic and cathodic current onset here is smaller than previous reports of ~1.5 V,[33, 42] although these reports used different working electrode substrates and their supporting electrolyte concentrations were approximately an order of magnitude lower than our measurements. The higher electrolyte concentration in our measurements would lead to a lower uncompensated resistance drop, as well as a larger magnitude of band bending, resulting in the smaller electrochemical potential range that we observe. Closer inspection of the voltammogram also reveals shoulders prior to an exponential increase in current in both the anodic and cathodic directions, which are attributable to corrosion processes.[33] For a better comparison to our device architecture, we also conducted cyclic voltammetry on $CH_3NH_3PbI_3$ films deposited on PEDOT:PSS modified ITO (Figure 3-3a inset). The anodic current onset potential for $CH_3NH_3PbI_3$ deposited on ITO (0.05 V vs Fc/Fc^+) was similar to that observed on the Au electrode, while the cathodic current onset was observed at a slightly more negative potential (-0.93 V vs. Fc/Fc^+) compared to that on the Au electrode.

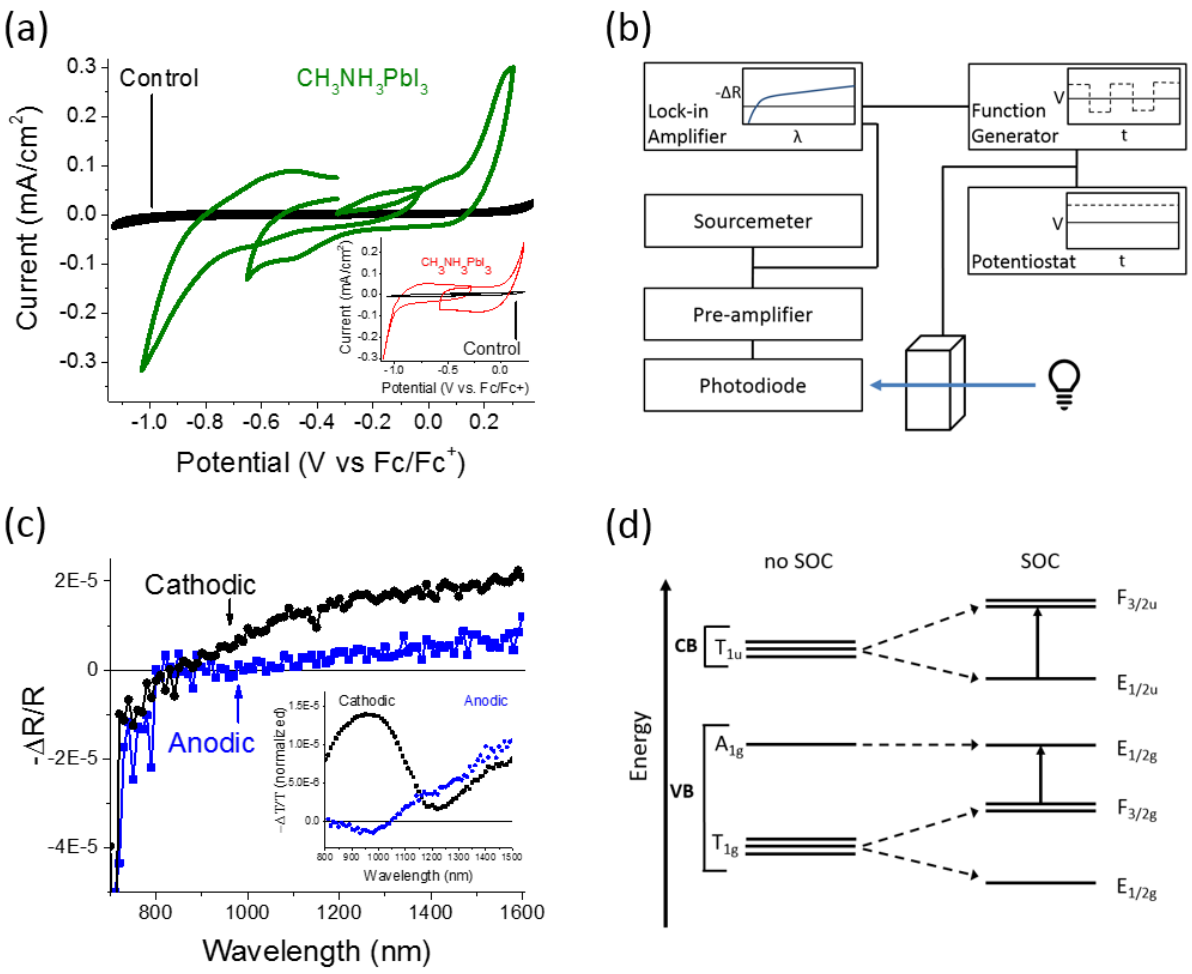

Figure 3-3. (a) Cyclic voltammetry of a $CH_3NH_3PbI_3$ film deposited on a gold electrode (green traces) and on an ITO/PEDOT:PSS electrode (inset: red traces), as well as control measurements made on each working electrode (black traces). Anodic and cathodic sweeps were made on fresh samples, each starting from the cell's open circuit potential. (b) Electromodulation experimental setup. (c) Electromodulated differential reflection (-ΔR/R) signal of $CH_3NH_3PbI_3$ deposited on the gold working electrode under cathodic (black) or anodic (blue) conditions. The inset shows the transmission mode differential signal, for $CH_3NH_3PbI_3$ deposited on an ITO/PEDOT:PSS working electrode under similar conditions, with the background signal subtracted. (d) Electronic state diagram and point group notation,[22] with and without including spin-orbit coupling (SOC),

at the R-point for $CH_3NH_3PbI_3$. The solid arrows between states represent the possible transitions that we propose we are able to observe in our electromodulation spectra in Fig. 3c.

Direct current spectroelectrochemical measurements entail applying a set potential for a period of time to inject charges into the compound of interest. One then measures the resulting change in that compound's spectral profile. This type of measurement is complicated in the $CH_3NH_3PbI_3$ system due to the perovskite's poor chemical stability in polar solutions, under illumination, and under an applied electric field.[34-35, 43-44] Therefore, with the anodic and cathodic current onset potentials determined from cyclic voltammetry, we used an electromodulation method to measure the spectra of a $CH_3NH_3PbI_3$ film while under charge accumulation conditions, as opposed to DC electrolysis. In this method (Figure 3-3b) a DC bias prior to the onset of either anodic or cathodic current is applied to the working electrode with a superimposed AC (square wave) perturbation which drives a change in the population of electrons or holes in the space-charge region. A lock-in amplifier coupled to a dual band Si/InGaAs photodetector measures the change in reflection or transmission of light at the working electrode. The wavelength dependent photodetector response and probe power intensity variation are corrected for by simultaneously measuring the steady state photodetector response with a DC sourcemeter. While this experimental method does limit the perovskite film degradation, as will be discussed in more detail below, a minor portion of the applied current likely leads to irreversible chemical reactions which do not contribute to the electromodulation response.

While the transient absorption spectra we've collected are made in transmission mode, inviting direct comparison to the transmission mode electromodulation spectra, there is some

uncertainty in the calculated $CH_3NH_3PbI_3$ contribution to the electromodulation spectra under these conditions due to the background electroabsorption of ITO, the changing oxidation state of PEDOT:PSS, and possible thin film interference effects overlapping with signals from the perovskite film (Figure A-2). Therefore, we will focus our discussion on the gold- $CH_3NH_3PbI_3$ electroreflectance data (Figure 3-3c), as these spectral features appear to be a more accurate representation for accumulated electrons or holes at the surface of the perovskite film. Under anodic charge accumulation conditions (0.04 ± 0.4 V vs. Fc/Fc^+, 1 kHz), a broad induced absorption is observed from 1050nm to 1600nm. Similarly, under cathodic charge accumulation conditions (-0.75 ± 0.4 V vs. Fc/Fc^+, 1 kHz), a broad induced absorption from 850 nm to 1600 nm is observed. Optical absorption transitions made by free charge carriers in semiconductors have historically been observed as perturbations to the absorption coefficient in the near- to mid-IR region as a result of p- or n-type chemical doping,[45-48] although similar features have been observed as a result of charge accumulation under the influence of an applied electric field.[49-50] These spectral features comprise contributions from direct interband transitions, which will present as an absorption peak, and indirect free carrier absorption (Drude absorption), which typically manifest as a structureless absorption signal which increases with increasing wavelength based on a power law relationship (λ^p);[51] the latter has been observed for $CH_3NH_3PbI_3$ in the mid- to far-IR region.[52] The higher energies at which the features that we observe are consistent with interband transitions from the conduction band minima to a higher lying conduction band, and transitions between the valence band maxima and lower lying valence bands (Figure 3-3d).[26, 53] While these transitions ($E_{1/2u} \rightarrow F_{1/2u}$ and $F_{3/2g} \rightarrow E_{1/2g}$) are forbidden due to symmetry considerations, several effects may break down the selection rules allowing for formally forbidden transitions to be observed, including the application of an

electric field.[54-55] While further analysis could be applied to quantify the Drude and interband contributions to the spectral features we observed under anodic and cathodic conditions, we focus here solely on their relationship to the character (i.e., either electron or hole) of the charge carriers from which they arise.

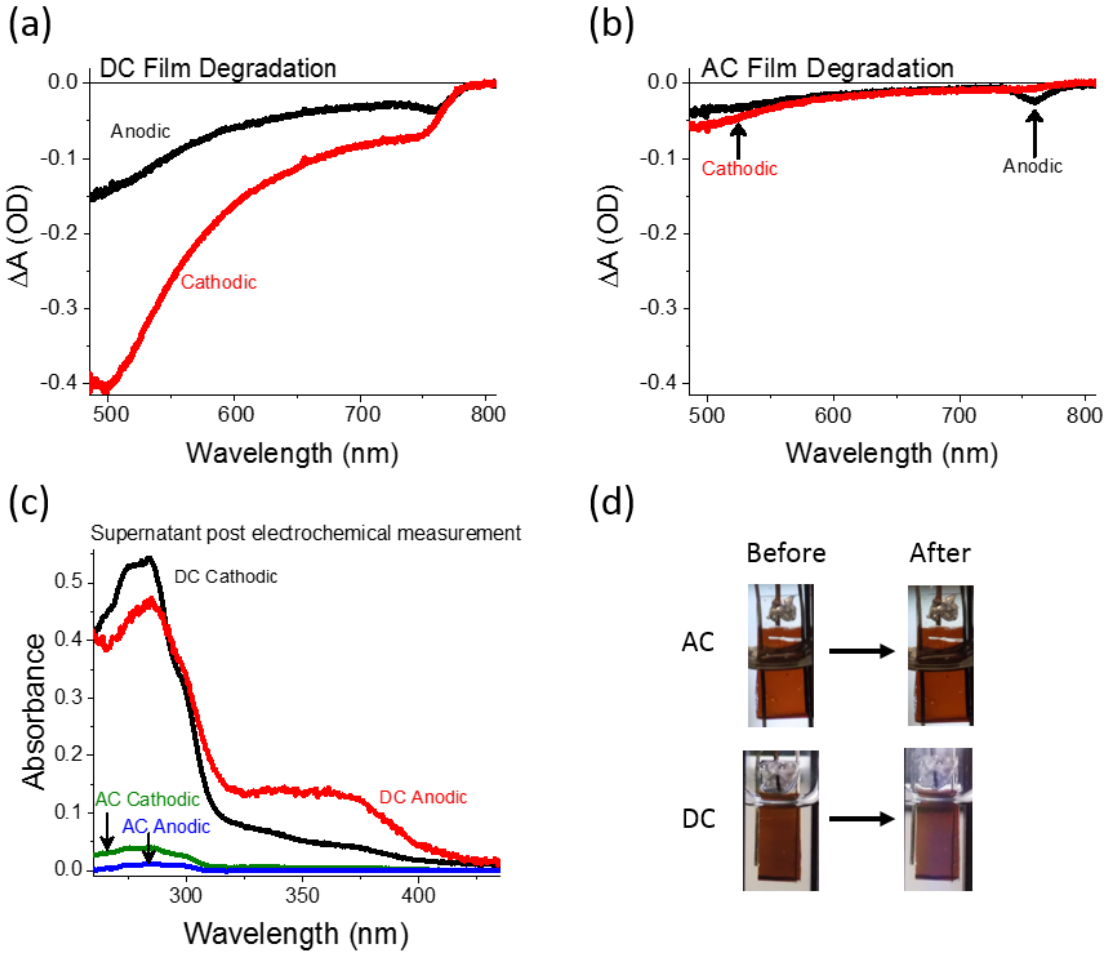

Figure 3-4. Change in absorbance (ΔA) of $CH_3NH_3PbI_3$ film after applying either a DC (a) or DC + AC (b) bias under anodic (black) and cathodic (red) conditions as described in the text. Absorbance measurements were made prior to applying an external bias and directly post spectroelectrochemical measurement. (c) Absorbance of electrolyte solution post-spectroelectrochemical measurement blanked against a solution where no bias was applied. (d) Photographs of $CH_3NH_3PbI_3$ films pre- and post-spectroelectrochemical measurement.

To discern what influence the electromodulation measurement has on the irreversible degradation of the $CH_3NH_3PbI_3$ film, we collected UV-vis spectra of the films before and after each set of electrochemical conditions. Here we used $CH_3NH_3PbI_3$ on PEDOT:PSS modified ITO as opposed to Au due to limited transmission of probe light through the Au substrate which would obscure our absorption measurements. In contrast to the electromodulation method, applying either an anodic (0.05 V vs. Fc/Fc^+) or cathodic (-0.9 V vs. Fc/Fc^+) DC bias to the working electrode resulted in dramatic degradation of the $CH_3NH_3PbI_3$ layer (Figure 3-4a and 3-4b), where the degradation was observed as a bleaching of the ground-state absorbance spectrum. While the AC method (DC bias ± 0.4 V, 1 kHz) also results in slight irreversible film degradation, we found this method mitigates the degradation process at both anodic and cathodic potentials. The degradation observed here corresponds to GIXRD measurements made on each film following each set of electrochemical conditions (Figure A-4), where we observed a decrease in the ratio of the $CH_3NH_3PbI_3$ (110) peak to that of the PbI_2 (001) peak comparing the DC to the DC + AC measurement. This is a qualitative comparison, as additional degradation of the $CH_3NH_3PbI_3$ layer likely occurred during the GIXRD measurement due to the films being exposed to ambient atmosphere prior to and during the measurement.

The UV-vis absorbance of the electrolyte solution after the spectroelectrochemical measurement were made (Figure 3-4c) shows additional evidence for increased $CH_3NH_3PbI_3$ film degradation from the strictly DC process, with absorptions at 285 nm and 370 nm corresponding, respectively, to PbI_2 and PbI_3^- in solution.[56] Here all spectra have had the spectrum from a solution where no bias has been applied to the working electrode subtracted away to highlight the magnitude of degradation occurring under each set of electrochemical

conditions. Under both sets of AC conditions, we found the dissolution of PbI_2 to be comparable to that of having a film immersed in the electrolyte solution with no applied bias. Under anodic conditions, film degradation likely proceeds through the oxidation of iodide resulting in the formation of I_3^-, which is readily soluble in polar solutions and would account for the observation of PbI_3^- in the electrolyte solution. Cathodic degradation for Pb based perovskite materials has been proposed to be due to charge localization at grain boundaries resulting in the formation of Pb^0 and I^-, followed by the dissolution of those species.[35] The presence of PbI_2 that we observe in the supernatant after applying cathodic potentials is then likely due to dissolution induced by the electric field as well as an increase in the polarity of the electrolyte solution. By applying an alternating current, we posit that the magnitude of polarization at the electrode is diminished, decreasing the decomposition of $CH_3NH_3PbI_3$ into the electrolyte solution.

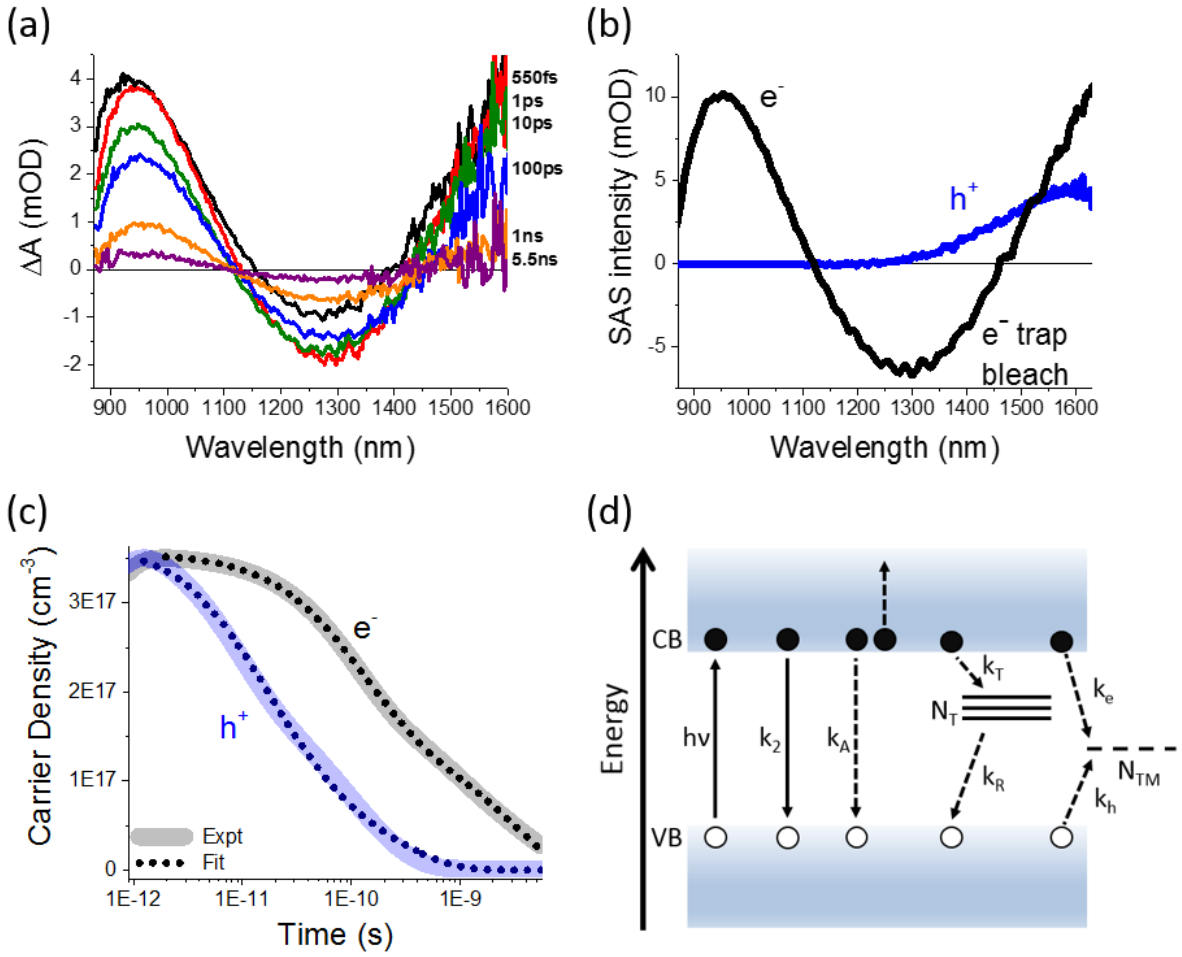

Figure 3-5. (a) Experimental transient absorption spectra for the PEDOT:PSS/$CH_3NH_3PbI_3$ system. (b) Species associated spectra (SAS) and (c) decay kinetics for the electron and hole contributions to the transient absorption spectra (transparent lines) with fits to our model (dotted lines) based on Eqs. 1 - 4 in the text. (d) Energy level diagram representing our model for recombination kinetics of holes in the valence (VB) and electrons in the conduction band (CB) of $CH_3NH_3PbI_3$. As in Eqs. 1 – 4, our model incorporates a state for charge extraction (N_{TM}) and trap state (N_T) mediated recombination, yielding the dotted "Fit" lines in Fig. 5c.

Using the spectral characterization obtained from our electromodulation measurements, we then investigated the excited-state dynamics using transient absorption spectroscopy to see if

the electromodulation features correspond to the expected dynamics for charge carriers in the presence of a selective hole accepting material. We prepared PEDOT:PSS/$CH_3NH_3PbI_3$ samples using the **2-step** method on glass substrates and excited with a 650nm pump pulse at various fluences and the change in optical density was monitored with a temporally delayed NIR probe. Negligible difference was observed in the spectra comparing the single layer $CH_3NH_3PbI_3$ to the bilayer PEDOT:PSS/$CH_3NH_3PbI_3$ (Figure A-5), therefore we can attribute the majority of the transient absorption signal in these measurements to the perovskite layer. The spectra and kinetics shown in Figures 3-5a-c correspond to charge carrier densities below the generation rate of a typical perovskite solar cell under AM1.5G conditions (~10^{21} cm^{-3}), but slightly above steady state carrier densities (10^{14}-10^{16} cm^{-3}).[57] As we observed in the single layer sample (Figure 3-2), two induced absorption features ($\Delta A > 0$) are present, along with a bleach ($\Delta A < 0$) in the bilayer sample (Figure 3-5a). Although the higher energy "peak" appears prominently, the spectral shape is likely perturbed by the trap state bleaching, leading to a local maximum due to overlap from the positive and negative features. It should be noted that, while the transient absorption spectra differ from the reflection mode electromodulation spectra (Figure 3-3c), taking a linear combination of the transmission mode anodic and cathodic $CH_3NH_3PbI_3$ electromodulation spectra results in a qualitatively comparable spectrum (Figure A-6). Increasing the pump pulse fluence led to a decreased lifetime for both the high and low energy induced absorptions (Figure A-7), which is expected for free carrier recombination.[20]

Due to the spectral overlap we observed in our electromodulation experiment, we applied global target analysis to kinetically resolve the transient absorption spectra associated with electron and hole dynamics in this system. These species-associated spectra or "SAS" are displayed in Figure 3-5b. Our target analysis assumes a set of species with time-invariant

absorption spectra with time-variant concentrations which decay monoexponentially. However, free charge carrier decay is typically more complex than can be physically modeled by simple exponential decay, so we sought to deconvolute our set of spectra into contributions from the electron and hole signals by first beginning with two distinct sets of spectrally-invariant sequential decay components. The linear sum of each set of components was then taken as the decay profile for each SAS in Figure 3-5c. Since our reflection mode electromodulation spectra under anodic conditions exhibit negligible amplitude between the wavelength range from ~800 nm to ~1050 nm, we applied this physicochemical constraint in our target analysis model to recover the SAS for positive charge carriers (h^+) in Figure 3-5b.

To account for the various recombination pathways for photoexcited electrons and holes in $CH_3NH_3PbI_3$, including charge transfer to the PEDOT:PSS layer, we fit the kinetics for electron SAS to a series of ordinary differential equations (Eqs. 1 - 4), which model the electronic processes shown in Figure 3-5d. A similar model has been used to model charge recombination in time-resolved microwave conductivity measurements,[16] although we included an additional term for Auger recombination in our model. Following light absorption ($h\nu$), an equal population of electrons in the conduction band ($\Delta n_{CB} = \Delta n_e$) and holes in the valence band ($-\Delta n_{VB} = \Delta n_h$) are generated. Here we assume each absorbed photon generates one free electron and hole due to this material's low exciton binding energy.[58-60] These photoexcited charge carriers can then recombine via a bimolecular pathway (k_2), a trap state (N_T) assisted monomolecular pathway (k_T and k_R), or the Auger pathway (k_A), in which two carriers recombine non-radiatively by transferring energy to a third carrier. Interfacing the $CH_3NH_3PbI_3$ layer to a charge transport material (N_{TM}) results in additional monomolecular rate constants for either electron or hole transfer (k_e and k_h). In the case of a hole transport material being in

contact with the perovskite layer, k_e may also denote electron localization by a trap site at the interface. Equations 1-4 model the change in electron population over time (see SI for the coupled equations which model the change in hole population).

$$\frac{dn_{CB}}{dt} = -k_T n_e(N_T - n_T) - k_2 n_e n_h - k_A(n_e{}^2 n_h + n_e n_h{}^2) - k_e n_e \quad (1)$$

$$\frac{dn_{VB}}{dt} = k_R n_T n_h + k_2 n_e n_h + k_A(n_e{}^2 n_h + n_e n_h{}^2) + k_h n_h \quad (2)$$

$$\frac{dn_T}{dt} = k_T n_e(N_T - n_T) - k_R n_T n_h \quad (3)$$

$$\frac{dn_{TM}}{dt} = k_e n_e - k_h n_h \quad (4)$$

The results of fitting both the species associated spectra (Figure 3-5d) to this model are presented in Table 3-2. Some caution must be taken when interpreting these values, as there exists a range of dependency between parameters (see Tables A-2 – A-4 for correlation matrices). Both the bimolecular and Auger rate constants for the $CH_3NH_3PbI_3$ sample are in good agreement with those previously reported from transient absorption measurements.[20, 61] We observed a larger trapping rate constant than had previously been reported by time resolved microwave conductivity measurements, although the samples were prepared using different fabrication procedures and differences in sample preparation have been shown to influence the nature of trap states present in $CH_3NH_3PbI_3$.[41, 62] As one might anticipate, we find that the rate for hole transfer to PEDOT:PSS ($k_h = 2.6 \times 10^9\ s^{-1}$) was an order of magnitude larger than that for electron transfer ($k_e = 3.1 \times 10^8\ s^{-1}$). This difference between the rate of electron and hole transfer is consistent with those measured for $CH_3NH_3PbI_3$ interfaced with other commonly used organic charge extraction layers.[16]

Table 3-2. Model Parameters for Fitting Electron and Hole Species Associated Spectra (SAS)

k_T (cm^3s^{-1})	k_R (cm^3s^{-1})	k_2 (cm^3s^{-1})	N_T (cm^{-3})	k_A (cm^6s^{-1})	k_e (s^{-1})	k_h (s^{-1})
2.6 (±0.1) x 10^{-8}	6 (±4) x 10^{-10}	4 (±3) x 10^{-10}	2.2 (±0.1) x 10^{17}	4 (± 2) x 10^{-28}	3.1 (±0.1) x 10^{8}	2.6 (±0.7) x 10^{9}

If the bleach we observe in the **2-step** sample is correlated to a mid-gap electron trap state that is removed in the **1-step** fabrication method, then the signal associated with electrons in this system should have an increased lifetime. Under the same excitation conditions, we observe diverging kinetics between the two samples beginning at roughly 200 ps, after which the **1-step** sample exhibits a slower decay (Figure 3-6a). Fitting each kinetic trace to Eqs. 1 – 3 with $k_e = k_h = 0$ allows us to analyze the different parameter values (Table 3-3). Comparing the two samples, both the bimolecular and auger recombination rate constants are within error of one another, and these calculated values are within the range found in literature.[63] We also observe an increase in the trapping rate constant in the **1-step** sample (3.9 x 10^{-8} cm^3s^{-1}) compared to the **2-step** sample (1.7 x 10^{-8} cm^3s^{-1}), but with a lower trap state density 1.5 x 10^{17} cm^{-3} compared to 4.6 x 10^{17} cm^{-3}. We will note that an inverse correlation exists between N_T and k_T in fitting the data to this model (Table A-3 – A-4), but the relatively larger change in trap state density compared to trapping rate constant between the two samples, implies that a higher trap state density exists in the **2-step** film. Based on our analysis of the transient absorption spectra, it appears that the trap state energy may be shifting towards the valence band maximum in the **1-step** film**,** in which case, according to Shockley-Read-Hall theory, we would expect an increase in the rate constant associated with charge trapping (k_T), which is what we observe.[64] Our calculated k_T and k_R are in agreement with a recent spectroscopic study which found trapping to occur on the sub-ns time scale, but overall charge recombination to occur on longer time scales.[65]

Table 3-3. Model Parameters for Fitting Electron Kinetics

Sample	k_T (cm^3s^{-1})	k_R (cm^3s^{-1})	k_2 (cm^3s^{-1})	N_T (cm^{-3})	k_A (cm^6s^{-1})
1-step	3.9 (±0.3) x 10^{-8}	3 (±2) x 10^{-10}	3 (±2) x 10^{-10}	1.5 (±0.2) x 10^{17}	6 (±5) x 10^{-28}
2-step	1.7 (±0.5) x 10^{-8}	3 (±2) x 10^{-10}	4 (±3) x 10^{-10}	4.6 (±0.1) x 10^{17}	8 (±1) x 10^{-28}

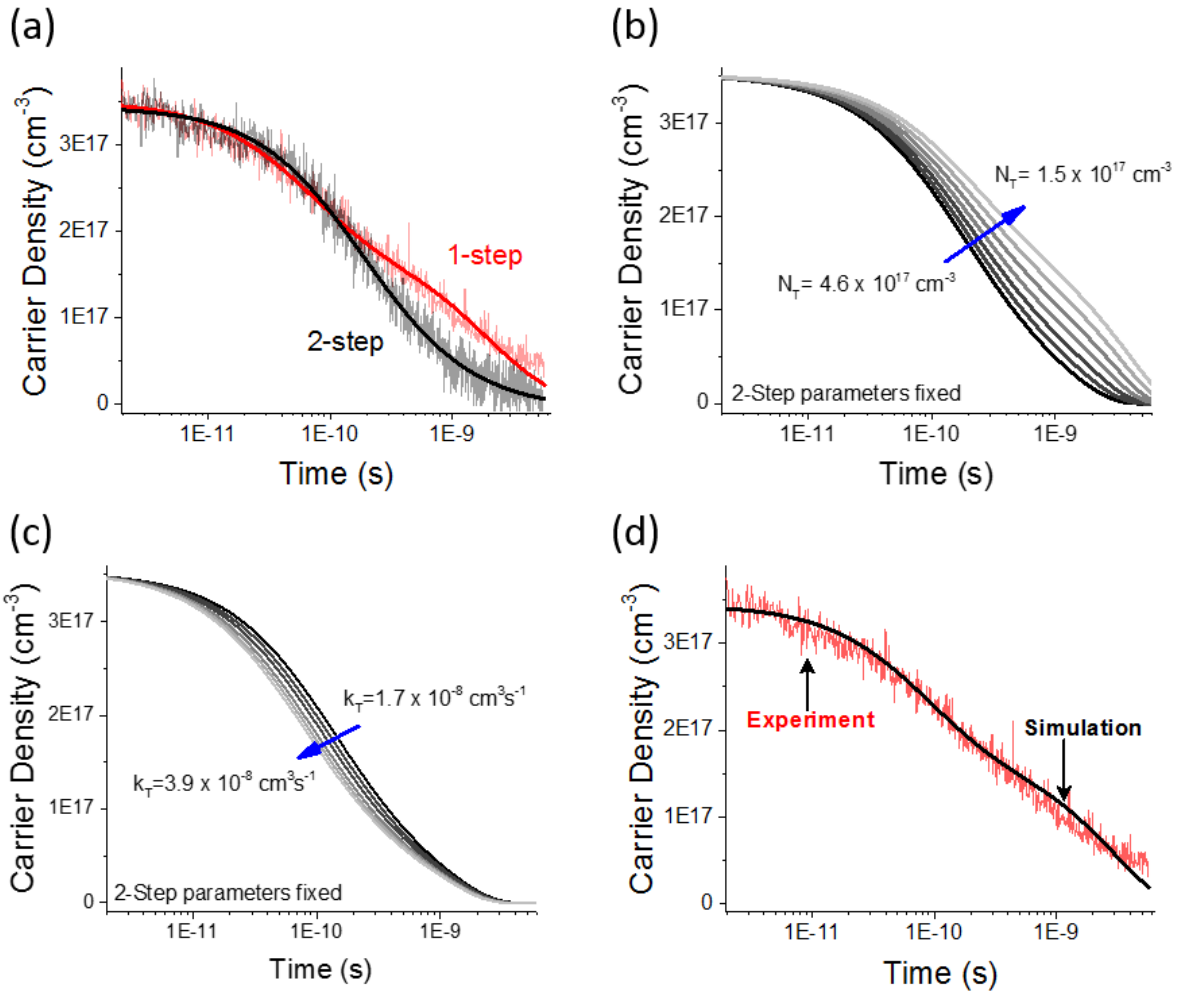

Figure 3-6. (a) Comparison of the kinetics associated with the electron lifetime (signal averaged 980-1000 nm) for the **1-step** (red) and **2-step** (black) fabrication methods with fits to Eqs. 1-3 with $k_e = k_h = 0$. Model simulation using initial parameters from **2-step** sample showing effect of (b) decreasing trap state density and (c) increasing trapping rate. (d) Comparison of the **1-step**

experimental data (red) and a model simulation of the **2-step** parameters (black) with k_T and N_T replaced with those of the **1-step** values.

Given the number of parameters included in our physical model (Eqs. 1 - 4), it is not immediately obvious by cursory inspection that the change in electron lifetime is due mainly to differences in the parameters related to the trapping process. To clarify the role of charge trapping, we used our model to simulate the effect on the signal amplitude as a function of time by varying each of the kinetic parameters individually, beginning with the initial values from the fit of the **2-step** data. The results of these simulations are shown in Figure 3-6. By varying the trap state density from the initial value for the **2-step** fit toward that of the **1-step** (Figure 3-6b), the electron lifetime increases, while increasing the trapping rate constant from the initial **2-step** value toward that of the **1-step** results in a shorter lifetime (Figure 3-6c). We can see that by changing only these two parameters while keeping all the other parameter values from the **2-step** fit, we can closely recover the dynamics of the **1-step** system (Figure 3-6d). This suggests that the differences we observe in the electron lifetime is correlated to both the trapping rate and trap state density.

There is still a debate in the literature as to the nature of $CH_3NH_3PbI_3$ deep level defect states. From computational studies, deep level electron accepting trap states in $CH_3NH_3PbI_3$ arise due to either interstitial iodine (I_i)[65-66] or iodine anti-site substitution on methylammonium (I_{MA}) or lead (I_{Pb}) sites, although I_{Pb} would have a small capture cross section as it is a charged defect.[62] The exact values for the depth of these traps have been shown to be dependent on the computational method employed.[66] Experimentally, deep trap levels have been observed at ~500-750 meV below the conduction band,[36, 67] although analysis as to the nature of the defects

was dependent on the chosen computational method. It appears likely that a distribution of trap states exists,[68] which include both I_i and I_{MA} defects. Energetically, the bleach we observe in our transient absorption measurement of the **2-step** sample is in agreement with the calculated energy for the I_i^+ defect level.[65] Assuming the main defect leading to the bleach in our **2-step** sample is I_i, it seems plausible that the hypophosphorous acid added in the **1-step** precursor solution acts to reduce I^+, pushing the defect energy further toward the valence band maximum. This would arguably account for trap state bleaching in the **1-step** sample being shifted to lower energies (>1600 nm) than we are able to observe with our InGaAs detector. Alternatively, growing $CH_3NH_3PbI_3$ in I-rich conditions, such as those for our **1-step** deposition, lowers the formation energy for I_{MA}, whose (0/-) level is ~200 meV closer to the valence band maximum than I_i (+/0) level. [65-66, 69]

3.4 Conclusion

In this work, we investigated the impact on device performance between 1- and 2-step fabrication methods for $CH_3NH_3PbI_3$. By utilizing electromodulation spectroscopy under charge accumulation conditions, we characterized and proposed distinct spectral assignments for electrons and holes in the perovskite layer. Based on this finding, we applied global target analysis to NIR excited state spectral features present in $CH_3NH_3PbI_3$ thin films to kinetically resolve contributions from photogenerated electrons and holes, as well as identify deep level electron traps. Our results suggest the increase in fill factor comparing the 1-step fabrication method to the 2-step is due to a decrease in trap state density, which correlates with longer electron lifetimes. The methodology we have presented for spectral assignments of charge carriers in this system should have broader applicability to improving design rationale in systems

which exhibit poor efficiencies due to slow interfacial charge transfer or fast back electron transfer, which are factors in many non-lead based photovoltaic perovskite materials.

3.5 References

1. Saliba, M.; Matsui, T.; Domanski, K.; Seo, J. Y.; Ummadisingu, A.; Zakeeruddin, S. M.; Correa-Baena, J. P.; Tress, W. R.; Abate, A.; Hagfeldt, A.; Gratzel, M., Incorporation of rubidium cations into perovskite solar cells improves photovoltaic performance. *Science* **2016,** *354* (6309), 206-209.
2. Stranks, S. D.; Eperon, G. E.; Grancini, G.; Menelaou, C.; Alcocer, M. J.; Leijtens, T.; Herz, L. M.; Petrozza, A.; Snaith, H. J., Electron-hole diffusion lengths exceeding 1 micrometer in an organometal trihalide perovskite absorber. *Science* **2013,** *342* (6156), 341-4.
3. Yang, Y.; Ostrowski, D. P.; France, R. M.; Zhu, K.; van de Lagemaat, J.; Luther, J. M.; Beard, M. C., Observation of a hot-phonon bottleneck in lead-iodide perovskites. *Nat. Photonics* **2015,** *10* (1), 53-59.
4. Munson, K. T.; Kennehan, E. R.; Doucette, G. S.; Asbury, J. B., Dynamic Disorder Dominates Delocalization, Transport, and Recombination in Halide Perovskites. *Chem* **2018,** *4* (12), 2826-2843.
5. Niesner, D.; Zhu, H.; Miyata, K.; Joshi, P. P.; Evans, T. J.; Kudisch, B. J.; Trinh, M. T.; Marks, M.; Zhu, X. Y., Persistent Energetic Electrons in Methylammonium Lead Iodide Perovskite Thin Films. *J. Am. Chem. Soc.* **2016,** *138* (48), 15717-15726.
6. Deschler, F.; Price, M.; Pathak, S.; Klintberg, L. E.; Jarausch, D. D.; Higler, R.; Huttner, S.; Leijtens, T.; Stranks, S. D.; Snaith, H. J.; Atature, M.; Phillips, R. T.; Friend, R. H., High Photoluminescence Efficiency and Optically Pumped Lasing in Solution-Processed Mixed Halide Perovskite Semiconductors. *J. Phys. Chem. Lett.* **2014,** *5* (8), 1421-6.
7. Zhao, B.; Bai, S.; Kim, V.; Lamboll, R.; Shivanna, R.; Auras, F.; Richter, J. M.; Yang, L.; Dai, L.; Alsari, M.; She, X.-J.; Liang, L.; Zhang, J.; Lilliu, S.; Gao, P.; Snaith, H. J.; Wang, J.; Greenham, N. C.; Friend, R. H.; Di, D., High-efficiency perovskite–polymer bulk heterostructure light-emitting diodes. *Nat. Photonics* **2018,** *12*, 783-789.
8. Quan, L. N.; Quintero-Bermudez, R.; Voznyy, O.; Walters, G.; Jain, A.; Fan, J. Z.; Zheng, X.; Yang, Z.; Sargent, E. H., Highly Emissive Green Perovskite Nanocrystals in a Solid State Crystalline Matrix. *Adv. Mater.* **2017,** *29* (21).
9. Kepenekian, M.; Robles, R.; Katan, C.; Sapori, D.; Pedesseau, L.; Even, J., Rashba and Dresselhaus Effects in Hybrid Organic-Inorganic Perovskites: From Basics to Devices. *ACS Nano* **2015,** *9* (12), 11557-67.
10. Nie, W.; Tsai, H.; Asadpour, R.; Blancon, J. C.; Neukirch, A. J.; Gupta, G.; Crochet, J. J.; Chhowalla, M.; Tretiak, S.; Alam, M. A.; Wang, H. L.; Mohite, A. D., Solar cells. High-efficiency solution-processed perovskite solar cells with millimeter-scale grains. *Science* **2015,** *347* (6221), 522-5.
11. Shao, Y.; Xiao, Z.; Bi, C.; Yuan, Y.; Huang, J., Origin and elimination of photocurrent hysteresis by fullerene passivation in $CH_3NH_3PbI_3$ planar heterojunction solar cells. *Nat. Commun.* **2014,** *5*, 5784.
12. Li, C.-Z.; Liang, P.-W.; Sulas, D. B.; Nguyen, P. D.; Li, X.; Ginger, D. S.; Schlenker, C. W.; Jen, A. K. Y., Modulation of hybrid organic–perovskite photovoltaic performance by controlling the excited dynamics of fullerenes. *Mater. Horiz.* **2015,** *2* (4), 414-419.
13. Xing, G.; Mathews, N.; Sun, S.; Lim, S. S.; Lam, Y. M.; Gratzel, M.; Mhaisalkar, S.; Sum, T. C., Long-range balanced electron- and hole-transport lengths in organic-inorganic $CH_3NH_3PbI_3$. *Science* **2013,** *342* (6156), 344-7.

14. Marchioro, A.; Teuscher, J.; Friedrich, D.; Kunst, M.; van de Krol, R.; Moehl, T.; Grätzel, M.; Moser, J.-E., Unravelling the mechanism of photoinduced charge transfer processes in lead iodide perovskite solar cells. *Nat. Photonics* **2014,** *8* (3), 250-255.
15. Arora, N.; Dar, M. I.; Hinderhofer, A.; Pellet, N.; Schreiber, F.; Zakeeruddin, S. M.; Gratzel, M., Perovskite solar cells with CuSCN hole extraction layers yield stabilized efficiencies greater than 20%. *Science* **2017,** *358* (6364), 768-771.
16. Hutter, E. M.; Hofman, J.-J.; Petrus, M. L.; Moes, M.; Abellón, R. D.; Docampo, P.; Savenije, T. J., Charge Transfer from Methylammonium Lead Iodide Perovskite to Organic Transport Materials: Efficiencies, Transfer Rates, and Interfacial Recombination. *Adv. Energy Mater.* **2017**, 1602349.
17. Ponseca, C. S., Jr.; Hutter, E. M.; Piatkowski, P.; Cohen, B.; Pascher, T.; Douhal, A.; Yartsev, A.; Sundstrom, V.; Savenije, T. J., Mechanism of Charge Transfer and Recombination Dynamics in Organo Metal Halide Perovskites and Organic Electrodes, PCBM, and Spiro-OMeTAD: Role of Dark Carriers. *J. Am. Chem. Soc.* **2015,** *137* (51), 16043-8.
18. Price, M. B.; Butkus, J.; Jellicoe, T. C.; Sadhanala, A.; Briane, A.; Halpert, J. E.; Broch, K.; Hodgkiss, J. M.; Friend, R. H.; Deschler, F., Hot-carrier cooling and photoinduced refractive index changes in organic-inorganic lead halide perovskites. *Nat. Commun.* **2015,** *6*, 8420.
19. Flender, O.; Klein, J. R.; Lenzer, T.; Oum, K., Ultrafast photoinduced dynamics of the organolead trihalide perovskite $CH_3NH_3PbI_3$ on mesoporous TiO_2 scaffolds in the 320-920 nm range. *Phys. Chem. Chem. Phys.* **2015,** *17* (29), 19238-46.
20. Manser, J. S.; Kamat, P. V., Band filling with free charge carriers in organometal halide perovskites. *Nat. Photonics* **2014,** *8* (9), 737-743.
21. Even, J.; Pedesseau, L.; Jancu, J.-M.; Katan, C., Importance of Spin–Orbit Coupling in Hybrid Organic/Inorganic Perovskites for Photovoltaic Applications. *J. Phys. Chem. Lett.* **2013,** *4* (17), 2999-3005.
22. Even, J.; Pedesseau, L.; Katan, C., Analysis of Multivalley and Multibandgap Absorption and Enhancement of Free Carriers Related to Exciton Screening in Hybrid Perovskites. *J. Phys. Chem. C* **2014,** *118* (22), 11566-11572.
23. Tanaka, K.; Takahashi, T.; Ban, T.; Kondo, T.; Uchida, K.; Miura, N., Comparative study on the excitons in lead-halide-based perovskite-type crystals $CH_3NH_3PbBr_3$ $CH_3NH_3PbI_3$. *Solid State Commun.* **2003,** *127* (9-10), 619-623.
24. Leguy, A. M.; Azarhoosh, P.; Alonso, M. I.; Campoy-Quiles, M.; Weber, O. J.; Yao, J.; Bryant, D.; Weller, M. T.; Nelson, J.; Walsh, A.; van Schilfgaarde, M.; Barnes, P. R., Experimental and theoretical optical properties of methylammonium lead halide perovskites. *Nanoscale* **2016,** *8* (12), 6317-27.
25. Umebayashi, T.; Asai, K.; Kondo, T.; Nakao, A., Electronic structures of lead iodide based low-dimensional crystals. *Phys. Rev. B* **2003,** *67* (15), 155405.
26. Hirasawa, M.; Ishihara, T.; Goto, T., Exciton Features in 0-Dimensional, 2-Dimensional, and 3-Dimensional Networks of $[PbI_6]^{4-}$ Octahedra. *J. Phys. Soc. Jpn.* **1994,** *63* (10), 3870-3879.
27. Schulz, P.; Dowgiallo, A. M.; Yang, M.; Zhu, K.; Blackburn, J. L.; Berry, J. J., Charge Transfer Dynamics between Carbon Nanotubes and Hybrid Organic Metal Halide Perovskite Films. *J. Phys. Chem. Lett.* **2016,** *7* (3), 418-25.
28. Zhai, Y.; Sheng, C. X.; Zhang, C.; Vardeny, Z. V., Ultrafast Spectroscopy of Photoexcitations in Organometal Trihalide Perovskites. *Adv. Funct. Mater.* **2016,** *26* (10), 1617-1627.
29. Ren, G.; Schlenker, C. W.; Ahmed, E.; Subramaniyan, S.; Olthof, S.; Kahn, A.; Ginger, D. S.; Jenekhe, S. A., Photoinduced Hole Transfer Becomes Suppressed with Diminished Driving Force in Polymer-Fullerene Solar Cells While Electron Transfer Remains Active. *Adv. Funct. Mater.* **2013,** *23* (10), 1238-1249.
30. Amthor, S.; Noller, B.; Lambert, C., UV/Vis/NIR spectral properties of triarylamines and their corresponding radical cations. *Chem. Phys.* **2005,** *316* (1-3), 141-152.

31. Kolle, U.; Moser, J.; Gratzel, M., Dynamics of Interfacial Charge-Transfer Reactions in Semiconductor Dispersions - Reduction of Cobaltoceniumdicarboxylate in Colloidal TiO_2. *Inorg. Chem.* **1985,** *24* (14), 2253-2258.
32. Dubois, D.; Kadish, K. M.; Flanagan, S.; Haufler, R. E.; Chibante, L. P. F.; Wilson, L. J., Spectroelectrochemical Study of the C_{60} and C_{70} Fullerenes and Their Monoanions, Dianions, Trianions, and Tetraanions. *J. Am. Chem. Soc.* **1991,** *113* (11), 4364-4366.
33. Samu, G. F.; Scheidt, R. A.; Kamat, P. V.; Janaky, C., Electrochemistry and Spectroelectrochemistry of Lead Halide Perovskite Films: Materials Science Aspects and Boundary Conditions. *Chem. Mater.* **2018,** *30* (3), 561-569.
34. Hsu, H. Y.; Ji, L.; Ahn, H. S.; Zhao, J.; Yu, E. T.; Bard, A. J., A Liquid Junction Photoelectrochemical Solar Cell Based on p-Type $MeNH_3PbI_3$ Perovskite with 1.05 V Open-Circuit Photovoltage. *J. Am. Chem. Soc.* **2015,** *137* (46), 14758-64.
35. Shallcross, R. C.; Zheng, Y.; Saavedra, S. S.; Armstrong, N. R., Determining Band-Edge Energies and Morphology-Dependent Stability of Formamidinium Lead Perovskite Films Using Spectroelectrochemistry and Photoelectron Spectroscopy. *J. Am. Chem. Soc.* **2017,** *139* (13), 4866-4878.
36. Heo, S.; Seo, G.; Lee, Y.; Lee, D.; Seol, M.; Lee, J.; Park, J.-B.; Kim, K.; Yun, D.-J.; Kim, Y. S.; Shin, J. K.; Ahn, T. K.; Nazeeruddin, M. K., Deep level trapped defect analysis in $CH_3NH_3PbI_3$ perovskite solar cells by deep level transient spectroscopy. *Energy Environ. Sci.* **2017,** *10* (5), 1128-1133.
37. Li, M.; Xie, Y.-M.; Xu, X.; Huo, Y.; Tsang, S.-W.; Yang, Q.-D.; Cheng, Y., Comparison of processing windows and electronic properties between $CH_3NH_3PbI_3$ perovskite fabricated by one-step and two-step solution processes. *Org. Electron.* **2018,** *63*, 159-165.
38. Lewis, A. E.; Zhang, Y.; Gao, P.; Nazeeruddin, M. K., Unveiling the Concentration-Dependent Grain Growth of Perovskite Films from One- and Two-Step Deposition Methods: Implications for Photovoltaic Application. *ACS Appl. Mater. Interfaces* **2017,** *9* (30), 25063-25066.
39. Xiao, Z. G.; Bi, C.; Shao, Y. C.; Dong, Q. F.; Wang, Q.; Yuan, Y. B.; Wang, C. G.; Gao, Y. L.; Huang, J. S., Efficient, high yield perovskite photovoltaic devices grown by interdiffusion of solution-processed precursor stacking layers. *Energy Environ. Sci.* **2014,** *7* (8), 2619-2623.
40. Snellenburg, J. J.; Laptenok, S. P.; Seger, R.; Mullen, K. M.; van Stokkum, I. H. M., Glotaran: A Java-Based Graphical User Interface for the R Package TIMP. *J. Stat. Softw* **2012,** *49* (3), 1-22.
41. Wu, X.; Trinh, M. T.; Niesner, D.; Zhu, H.; Norman, Z.; Owen, J. S.; Yaffe, O.; Kudisch, B. J.; Zhu, X. Y., Trap states in lead iodide perovskites. *J. Am. Chem. Soc.* **2015,** *137* (5), 2089-96.
42. Leijtens, T.; Stranks, S. D.; Eperon, G. E.; Lindblad, R.; Johansson, E. M.; McPherson, I. J.; Rensmo, H.; Ball, J. M.; Lee, M. M.; Snaith, H. J., Electronic Properties of Meso-Superstructured and Planar Organometal Halide Perovskite Films: Charge Trapping, Photodoping, and Carrier Mobility. *ACS Nano* **2014,** *8* (7), 7147-55.
43. Christians, J. A.; Miranda Herrera, P. A.; Kamat, P. V., Transformation of the excited state and photovoltaic efficiency of $CH_3NH_3PbI_3$ perovskite upon controlled exposure to humidified air. *J. Am. Chem. Soc.* **2015,** *137* (4), 1530-8.
44. Aristidou, N.; Sanchez-Molina, I.; Chotchuangchutchaval, T.; Brown, M.; Martinez, L.; Rath, T.; Haque, S. A., The Role of Oxygen in the Degradation of Methylammonium Lead Trihalide Perovskite Photoactive Layers. *Angew. Chem., Int. Ed. Engl.* **2015,** *54* (28), 8208-12.
45. Briggs, H. B.; Fletcher, R. C., New Infrared Absorption Bands in p-Type Germanium. *Phys. Rev.* **1952,** *87* (6), 1130-1131.
46. Spitzer, W. G.; Whelan, J. M., Infrared Absorption and Electron Effective Mass in n-Type Gallium Arsenide. *Phys. Rev.* **1959,** *114* (1), 59-63.
47. Gobeli, G. W.; Fan, H. Y., Infrared Absorption and Valence Band in Indium Antimonide. *Phys. Rev.* **1960,** *119* (2), 613-620.
48. Spitzer, W.; Fan, H. Y., Infrared Absorption in n-Type Silicon. *Phys. Rev.* **1957,** *108* (2), 268-271.

49. Venkateswara Rao, A.; Chazalviel, J. N.; Ozanam, F., In-situ characterization of the n-Si/acetonitrile interface by electromodulated infrared internal-reflection spectroscopy. *J. Appl. Phys.* **1986,** *60* (2), 696-706.
50. Harrick, N. J., Optical Spectrum of the Semiconductor Surface States from Frustrated Total Internal Reflections. *Phys. Rev.* **1962,** *125* (4), 1165-1170.
51. Pankove, J. I., *Optical Processes in Semiconductors*. Dover Publications, Inc.: New York, N.Y., 1971.
52. Narra, S.; Chung, C. C.; Diau, E. W.; Shigeto, S., Simultaneous Observation of an Intraband Transition and Distinct Transient Species in the Infrared Region for Perovskite Solar Cells. *J. Phys. Chem. Lett.* **2016,** *7* (13), 2450-5.
53. Giovanni, D.; Ma, H.; Chua, J.; Gratzel, M.; Ramesh, R.; Mhaisalkar, S.; Mathews, N.; Sum, T. C., Highly spin-polarized carrier dynamics and ultralarge photoinduced magnetization in $CH_3NH_3PbI_3$ perovskite thin films. *Nano Lett.* **2015,** *15* (3), 1553-8.
54. Brahms, S.; Cardona, M., Electric Field Effects on Optical Transitions to the n=1 Exciton in Cuprous Oxide. *Solid State Commun.* **1968,** *6*, 733-736.
55. Ahn, D.; Chuang, S. L., Intersubband optical absorption in a quantum well with an applied electric field. *Phys. Rev. B* **1987,** *35* (8), 4149-4151.
56. Stamplecoskie, K. G.; Manser, J. S.; Kamat, P. V., Dual nature of the excited state in organic–inorganic lead halide perovskites. *Energy Environ. Sci.* **2015,** *8* (1), 208-215.
57. Johnston, M. B.; Herz, L. M., Hybrid Perovskites for Photovoltaics: Charge-Carrier Recombination, Diffusion, and Radiative Efficiencies. *Acc. Chem. Res.* **2016,** *49* (1), 146-54.
58. D'Innocenzo, V.; Grancini, G.; Alcocer, M. J.; Kandada, A. R.; Stranks, S. D.; Lee, M. M.; Lanzani, G.; Snaith, H. J.; Petrozza, A., Excitons versus free charges in organo-lead tri-halide perovskites. *Nat. Commun.* **2014,** *5*, 3586.
59. Saba, M.; Cadelano, M.; Marongiu, D.; Chen, F.; Sarritzu, V.; Sestu, N.; Figus, C.; Aresti, M.; Piras, R.; Lehmann, A. G.; Cannas, C.; Musinu, A.; Quochi, F.; Mura, A.; Bongiovanni, G., Correlated electron-hole plasma in organometal perovskites. *Nat. Commun.* **2014,** *5*, 5049.
60. Ziffer, M. E.; Mohammed, J. C.; Ginger, D. S., Electroabsorption Spectroscopy Measurements of the Exciton Binding Energy, Electron–Hole Reduced Effective Mass, and Band Gap in the Perovskite $CH_3NH_3PbI_3$. *ACS Photonics* **2016,** *3* (6), 1060-1068.
61. Trinh, M. T.; Wu, X.; Niesner, D.; Zhu, X. Y., Many-body interactions in photo-excited lead iodide perovskite. *J. Mater. Chem. A* **2015,** *3* (17), 9285-9290.
62. Yin, W. J.; Shi, T. T.; Yan, Y. F., Unusual defect physics in $CH_3NH_3PbI_3$ perovskite solar cell absorber. *Appl. Phys. Lett.* **2014,** *104* (6), 063903.
63. Herz, L. M., Charge-Carrier Dynamics in Organic-Inorganic Metal Halide Perovskites. *Annu. Rev. Phys. Chem.* **2016,** *67*, 65-89.
64. Shockley, W.; Read, W. T., Statistics of the Recombinations of Holes and Electrons. *Phys. Rev.* **1952,** *87* (5), 835-842.
65. Meggiolaro, D.; Motti, S. G.; Mosconi, E.; Barker, A. J.; Ball, J.; Perini, C. A. R.; Deschler, F.; Petrozza, A.; De Angelis, F., Iodine chemistry determines the defect tolerance of lead-halide perovskites. *Energy Environ. Sci.* **2018,** *11* (3), 702-713.
66. Du, M. H., Density Functional Calculations of Native Defects in $CH_3NH_3PbI_3$: Effects of Spin-Orbit Coupling and Self-Interaction Error. *J. Phys. Chem. Lett.* **2015,** *6* (8), 1461-6.
67. Baumann, A.; Vath, S.; Rieder, P.; Heiber, M. C.; Tvingstedt, K.; Dyakonov, V., Identification of Trap States in Perovskite Solar Cells. *J. Phys. Chem. Lett.* **2015,** *6* (12), 2350-4.
68. Tress, W.; Yavari, M.; Domanski, K.; Yadav, P.; Niesen, B.; Correa Baena, J. P.; Hagfeldt, A.; Graetzel, M., Interpretation and evolution of open-circuit voltage, recombination, ideality factor and

subgap defect states during reversible light-soaking and irreversible degradation of perovskite solar cells. *Energy Environ. Sci.* **2018,** *11* (1), 151-165.
69. Agiorgousis, M. L.; Sun, Y. Y.; Zeng, H.; Zhang, S., Strong covalency-induced recombination centers in perovskite solar cell material $CH_3NH_3PbI_3$. *J. Am. Chem. Soc.* **2014,** *136* (41), 14570-5.

Chapter 4: Trap State Investigation in $CH_3NH_3PbI_3$ by Pump-Push-Probe Spectroscopy

4.1 Introduction

Hybrid organic-inorganic perovskites have shown exceptional optoelectronic properties allowing their incorporation into devices including photovoltaics, light emitting diodes,[1] and lasers.[2] Initial increases to device efficiency were realized through proper energy alignment of charge transport layers[3] and studies on compositional effects on phase stability,[4] but more recently improvements in efficiency have involved passivation of surface trap states to reduce unproductive recombination.[5-6] A greater understanding of the energetics of trap states, as well as their effect on charge carrier dynamics is necessary for perovskites to reach their potential.

Computational studies have looked at the nature of trap states in both the bulk[7] and at the surface[8] of perovskite films. This work has shown that a number of possible defects have energy levels within the band gap. Several experimental studies have provided evidence for the presence of electron traps including transient absorption,[9] two dimensional electronic spectroscopy,[10] and deep level transient spectroscopy.[11] While these studies provided information on the energy of trap levels and the formation of a trapped carrier population within the system, they do not focus on the effect of these trap states on overall carrier recombination.

Transient absorption spectroscopy has been an invaluable tool in studying the electronic structure of perovskites and its impact on charge carrier dynamics, from initial studies implying the presence of multiple valence and conduction bands[12] to more recent studies detailing electron-phonon coupling and large polaron formation.[13] Our group has previously shown some contribution to the NIR transient absorption signal for $CH_3NH_3PbI_3$ from interband carrier transitions in the valence and conduction bands, as well as trap state bleaching. Camargo et al.

showed that during transient absorption measurements there is some borrowing of oscillator strength for valence band to trap state transitions from a pump pulse with energy greater than the band gap.[10] This has implications for the modeling of kinetic parameters from transient absorption data as the actual occupied trap state density will differ from the assumed trap state occupation.

Pump-push-probe spectroscopy is a transient absorption technique where the push pulse is delayed in time relative to the pump which allows for controlled changes in excited state carrier populations. Previously the pump-push-probe method has been used on perovskite systems to study hot carrier relaxation times,[14] as well as the energetic barrier for hot carrier charge transfer to an electron acceptor.[15] In the first study, Hopper et al. utilized a NIR push and probe to model hot carrier dynamics in a series of lead halide perovskite systems, but their model neglected the presence of sub-gap trap states. In the latter case, the push pulse was used to excite electrons within the conduction band to higher energy states and the efficiency of charge transfer to the electron acceptor bphen was analyzed by probing the recovery of the ground state bleach. It was observed that for efficient charge transfer, a push pulse with energy greater than what was predicted by the difference in energy between the acceptor LUMO and perovskite conduction band minimum, implying an energy barrier between the two layers. As this method allows for controlled changes in excited state carrier populations, it provides an excellent opportunity for studying both the energetics and kinetics of electron trap states in lead halide perovskites.

In this study, we show that pump-push-probe spectroscopy can be used to determine the energy barrier between mid-gap electron trap states and the conduction band in $CH_3NH_3PbI_3$, and that the push induced dynamics can be modelled through a combination of hot carrier effects and changes in trapped and free electron densities. We find that a 1500 nm (0.83 eV) push pulse

is required to observe changes in recombination dynamics following hot carrier cooling which occurs within ~2 ps under our experimental conditions. Modelling of recombination kinetics following hot carrier cooling was found to imply that some valence band to trap state transition occurs upon above gap pumping. Additionally, we perform two pulse transient absorption with a sub-gap pump pulse to directly monitor recombination of trapped electrons with valence band holes. We find that a range of pump energies below the band gap are able to populate these trap states, but that the normalized recombination is independent of pump energy used. These observations imply that the common assumption in literature reports on pump induced carrier dynamics in time resolved spectroscopic measurements that the initial trap state density is negligible need to be reconsidered, along with the calculated recombination kinetic rate constants and subsequent analysis.

4.2 Experimental Methods

Perovskite film preparation: Perovskite films were prepared as previously described using a one step solution phase fabrication method. A precursor solution of 3:1 $Pb(OAc)_2 \cdot 3H_2O$ to CH_3NH_3I in anhydrous DMF, with 3 μL of hypophosphorous acid (50 wt% in H_2O). Glass slides were cleaned with sequential washing in water, acetone, and isopropanol, followed by drying and UV ozone treatment just prior to spin coating. Small volumes (>15 uL) of the precursor solution were spin coated on the glass slides. Samples were then allowed to dry at room temperature for 10 minutes, followed by annealing at 100°C for 5 minutes. Lewis bases were dissolved in anhydrous chlorobenzene at various concentrations. The Lewis base solution was then spin coated on the $CH_3NH_3PbI_3$ sample after it had been allowed to cool back to room temperature following the annealing process.

Transient Absorption: All transient absorption measurements were made on samples prepared on glass substrates and encapsulated under an inert atmosphere.

Our transient absorption experimental setup has been described previously.[16] Briefly, the output (800 nm, 50 fs, 1 kHz) from a Ti:sapphire laser system (Coherent, Libra) was used to generate both pump and probe beams for transient absorption measurements. This output is split using a 75/25 beam splitter with the higher intensity beam directed into the optical parametric amplifier (Coherent OPerA) for pump pulse generation, while the lower intensity beam was used for probe white light generation.

For probe beam generation, the Ti:sapphire output was focused onto a sapphire crystal for both visible and NIR spectral ranges. The SWIR probe was generated from 1550 nm output from an OPA. The change in transmittance of the sample is measured with a spectrometer coupled CMOS sensor for visible, and a 256 pixel InGaAs sensor for NIR and SWIR detection. An 850 nm long pass or 750 nm short pass filter was placed in front of the sample to attenuate excess 800nm light depending on which probe was used. A mechanical chopper (500 Hz) was used to collect pump on-pump off measurements.

Surface Xplorer software (Ultrafast Systems) was used to collect the transient absorption spectra and OriginLab OriginPro 9.1.0 was used to process, analyze, and plot the data.

Pump-push-probe: Pump and probe generation and alignment are the same as described for transient absorption measurements. For push pulse generation, a portion of the fundamental beam is routed to a second OPA (Coherent TOPAS). The output from this OPA is routed to the sample through a separate set of optics set to have a beam path slightly longer than that of the pump.

4.3 Results and Discussion

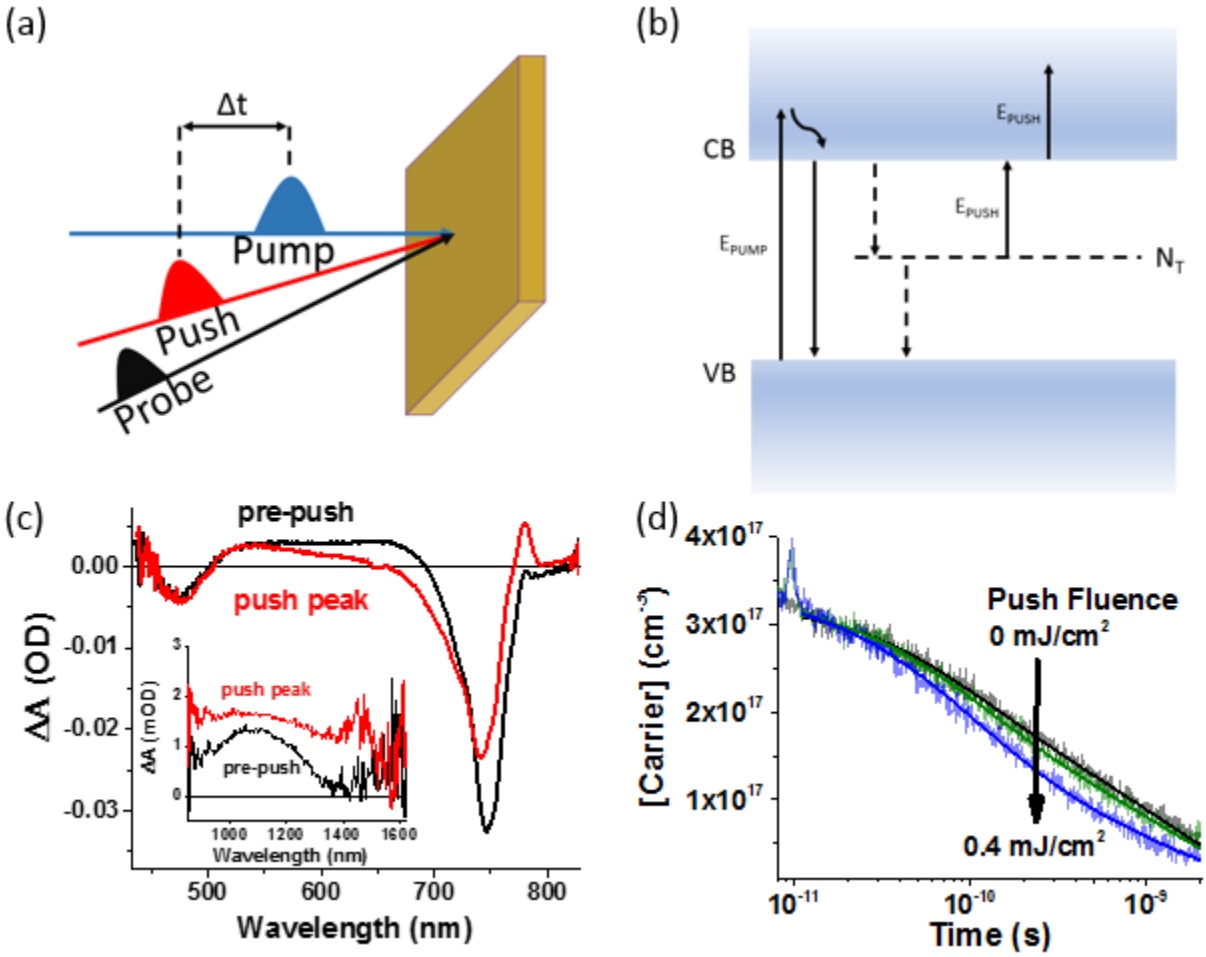

Figure 4-1. (a) Diagram for pump-push-probe spectroscopy (b) Schematic for transitions observed in pump-push-probe spectroscopy. (c) Transient absorption spectra in the visible and NIR (inset) showing the effect of the push pulse. (d) Comparison of kinetics for $CH_3NH_3PbI_3$ at 1000 nm induced absorption with increasing push pulse fluence. Dark lines are model fits as described in the main text.

To gain a better understanding of electron trapping kinetics in this system, we performed pump-push-probe spectroscopy (Figure 4-1a). Here we are pumping valence to conduction band transitions and probing the excited state spectra with a broadband probe (Figure 4-1b). At ~10 ps

following the pump pulse, a NIR push pulse is used to excite trapped electrons back into the conduction band. The time difference between the pump and push was chosen to allow for pump induced carriers to equilibrate to the band edge and a population of trapped electrons to form. In addition to exciting trapped carriers, the NIR push pulse interacts with band edge carriers to form a distribution of hot carriers, which is observed in the visible transient absorption spectra (figure 4-1c) as a decrease in signal at the band edge along with a broadening of this bleach to higher energies. The response we observe in the NIR (figure 4-1c, inset) is a broad increase in the induced absorption from 850-1600 nm. We'll first discuss hot carrier dynamics in order to differentiate their effect on observed spectra from changes occurring due to detrapping electrons.

A distribution of hot carriers in $CH_3NH_3PbI_3$ has previously been shown to broaden the high energy bleaching feature around the band edge.[17-19] We observe this broadening induced by the push pulse along with a decrease in the amplitude of the band edge signal which occurs due to the depopulation of carriers at the band edge. Fitting the ΔA signal above the band edge (>1.7 eV) to a Boltzmann distribution allows for the carrier temperature due to photoexcitation to be calculated (Figure B-1). We see an increase in initial carrier temperature from approximately 900 K to 1100 K and slower temperature decay as the push fluence is increased from 0.1 - 0.5 mJ/cm^{-2}. The later observation is in agreement with reports of the hot phonon bottleneck effect in lead halide perovskite films.[18]

Hot carrier cooling dynamics from Boltzmann analysis can also be compared to the change in signal amplitude at the band edge by fitting the decay of the change in ΔA due to a monoexponential function (Figure B-2). We observe carrier cooling lifetimes ranging from ~300-550 fs which vary linearly with push pulse fluence, and therefore hot carrier density. The lifetimes that we calculate are similar to those observed from pump-push-probe measurements

from Hopper et al.[14] Both this observation and the calculated carrier temperature cooling imply that hot carriers influence the transient spectral signal on the 100 fs to 1 ps time scale.

The effect of changes in trapped carrier density due to the push pulse is not as readily apparent as those due to hot carrier formation. When a push pulse with sufficient energy to promote a trapped electron to the conduction band is used, the signal at 1000 nm at times >10 ps following the push pulse begins to decrease more rapidly with increasing pulse fluence (Figure 4-1d). Here we choose to focus on the NIR kinetics, which we've previously shown to correlate to excited state conduction band electron transitions,[16] due to additional effects occurring near the band edge.

Through model simulations, we're able to account for this change in dynamics as faster observed recombination due to an increase in free carrier density as well as re-trapping of electrons. Here we've fit the kinetics for the measurement made with no push pulse to the following set of differential equations,

$$\frac{dn_e}{dt} = -k_T n_e (N_T - n_T) - k_2 n_e n_h - k_A (n_e^2 n_h + n_e n_h^2) \qquad (17)$$

$$\frac{dn_h}{dt} = -k_R n_h n_T - k_2 n_e n_h - k_A (n_e^2 n_h + n_e n_h^2) \qquad (18)$$

$$\frac{dn_T}{dt} = k_T n_e (N_T - n_T) - k_R n_h n_T \qquad (19)$$

where n_e is the population of electrons in the conduction band, n_h is the population of holes in the valence band, and n_T is population of trapped electrons in some overall density of trap states N_T. The rate constants governing carrier recombination between the three states are: k_2 for bimolecular recombination, k_A for Auger recombination, k_T for conduction band electron

trapping, and k_R for recombination of trapped electrons with valence band holes. The calculated values for k_2 ($4 \pm 2 \times 10^{-10}$ cm^3 s^{-1}), k_A ($7 \pm 1 \times 10^{-28}$ cm^6 s^{-1}), k_T ($4.7 \pm 0.8 \times 10^{-8}$ cm^3 s^{-1}), and k_R ($3.6 \pm 0.8 \times 10^{-10}$ cm^3 s^{-1}) are within error of what we've previously calculated for this system.[16]

In our previous analysis we assumed that each absorbed pump photon resulted in a free electron and free hole ($n_e = n_h$) and thus the initial values for Eq. 1 and Eq. 2 were determined by the pump fluence, while initial trap state population was assumed to be 0 cm^{-3}. By simulating Eq. 1-3 with the calculated rate constants, we're able estimate a trapped electron density of ~2 x 10^{16} cm^{-3} when the push pulse arrives at 10ps (Figure B-3). This trapped electron population, as well as the change in conduction band electron and valence band hole populations, then needs to be taken into account when modeling the kinetics following the push pulse. This is done by parameterizing the initial trapped electron population and setting the constraint $n_h = n_e + n_T$ for the initial values of electron and hole densities. The global fits for the kinetics following the push pulse can be seen in Figure 4-1d, where only the initial trapped electron density, and resultant conduction band electron density were allowed to vary. Fitting by this method results in a trapped electron density of $4 \pm 1 \times 10^{16}$ cm^{-3} prior to the push pulse, which is completely depopulated by a 0.4 mJ/cm^2 1500 nm push pulse.

To confirm that the change in kinetics we observe from 20 ps – 2 ns are the result of push induced changes in trapped and free electron populations, we performed the same pump-push-probe measurement using a lower energy (1630 nm) push pulse. Over a similar fluence range, we observe an increase in the induced absorption signal concurrent to the push pulse, with similar kinetics to the hot carrier cooling observed using the 1500 nm push (Figure B-4). We interpret

this to be due to the 1630 nm push not providing enough energy to excite trapped electrons into the conduction band. This allows us to estimate the energy difference between the conduction band minimum and upper edge of the mid-gap distribution of trap states present in the system as ~0.83 eV.

As an additional confirmation in the difference in timescales of hot carrier cooling from electron trapping, we performed pump-push-probe measurements on $CH_3NH_3PbI_3$ films treated with TOPO. We found that trioctylphosphine oxide treatment results in low energy bleaching (>1600 nm) that's present in non-treated $CH_3NH_3PbI_3$ becoming an induced absorption (Figure B-5a) implying that there is some degree of trap passivation in these samples. This passivation leads to a decrease in the longer timescale response to a 1500 nm push pulse due to changes in trapped and free electron densities ,while hot carrier effects are still observed to decay within 1-2 ps following the push (Figure B-5b).

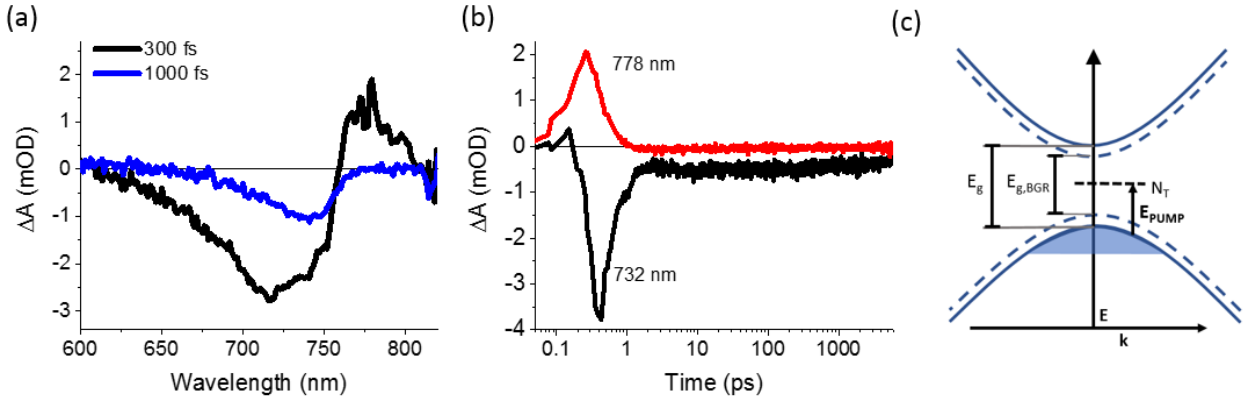

Figure 4-2. (a) Transient absorption spectra for a $CH_3NH_3PbI_3$ film following a sub-gap pump pulse (1100 nm) at times corresponding to maximum pump-probe overlap (black trace) and longer valence band bleaching (blue trace). (b) Kinetics of valence band bleach (black), and sub-gap induced absorption (red). (c) Diagram showing proposed phase-space filling and bandgap

renormalization as origins of sub-gap pump TA signal. Following the pump pulse, a population of holes is introduced to the valence band (blue shaded area) which results in a shift in the band extrema forming a new, lower energy bandgap ($E_{g,BGR}$).

To gain insight into the recombination of trapped electrons with valence band holes, we performed pump-probe spectroscopy using a sub-gap pump. Two distinct features can be observed at early times in the transient absorption spectrum (Figure 4-2a): an induced absorption below the band edge and a bleaching signal at higher energies. The low energy induced absorption decays within 1 ps, while the high energy bleach persists to 5.5 ns (Figure 4-2b). We attribute the negative signal at <750 nm to blocked valence band to conduction band transitions due to a reduced VB electron population and the induced absorption at 778 nm to band gap renormalization (Figure 4-2c).

Photoinduced absorption features just below the unperturbed band edge related to bandgap renormalization in $CH_3NH_3PbI_3$ have previously been shown to appear at <100 fs, and decay within 1-2 ps as carriers thermalize to the new energy states.[17] For all of the sub-gap excitation measurements in this study , we observe the induced absorption (778 nm) signal to peak within 500 fs, dependent on pump wavelength and fluence, followed by a decay to the baseline within 1-2 ps. As bandgap renormalization in semiconductors occurs due to Coulomb interactions between free carriers, this implies that in the case of sub-gap excitation resulting in valence band to trap state transitions, the change in band-edge energy would be due to an increase in hole density. Similar hole-induced bandgap renormalization has been shown in material's with engineered electron trap state densities.[20]

Due to using a sub-gap pump to excite our samples, changes in the transient absorption signal from the optical stark effect need to be taken into account. Yang et al. observed a similar derivative like feature, although opposite in sign, upon pumping $CH_3NH_3PbI_3$ with a high intensity 800 nm laser pulse.[21] This feature arises due to the influence of the electric field of a non-resonant laser pulse shifting the exciton transition energy higher and is most prominent when the laser pulse's energy is near that of the exciton transition. The shift in the exciton energy results in bleaching at the original transition energy and an induced absorption at higher energies correlating to the shift induced by the applied electric field. The resulting signal is the opposite of what we observe using lower energy pump pulse, occurs on a faster timescale, and thus has minimal influence on our analysis.

To corroborate the assignment of valence to trap state bleaching, we performed both fluence and energy dependence measurements using a sub-gap pump. The long lived bleaching feature at 732 nm is observed for pump energies ranging from 905 – 1500 nm, with the amplitude varying linearly with pump fluence (Figure B-6). As the pump energy is decreased the signal amplitude decreases for a given pulse power implying a decreased transition probability between the valence band and the distribution of trap states. When normalized after the decay of the fast spectral component (~2 ps), the decay of the long lived feature is observed to be independent of pump energy or fluence (Figure B-6), which is expected as single carrier trap recombination is a first-order process. The decay which occurs at >400 ps due to recombination of trapped electrons with valence band holes matches the rate calculated from our model.

4.4 Conclusions

In summary, we show that a combination of transient absorption measurements using a sub-gap pump pulse and pump-push-probe spectroscopy allow for a greater understanding of the timescale for electron trapping and recombination in $CH_3NH_3PbI_3$ thin films. By simplifying the excited state energy landscape with a pump pulse which induces valence band to trap state transitions, the recombination rate for trapped electrons and valence band holes (k_R) was calculated with greater confidence compared to the more complex model required for the system excited with an above gap pump pulse. Through comparing carrier cooling lifetimes and changes in kinetics induced by the push pulse in our pump-push-probe measurements, we were able to differentiate hot carrier effects from changes in trapped and free electron density. Modelling of the recombination following the push pulse implies that use of an above gap pump in two pulse transient absorption induces some initial trapped electron density which is counter to how these types of datasets are typically modelled. Overall this is important as the assumptions made for initial state populations for time-resolved spectroscopic measurements influence the calculated rate constants and their subsequent analysis.

4.5 References

1. Du, M. H., Density Functional Calculations of Native Defects in $CH_3NH_3PbI_3$: Effects of Spin-Orbit Coupling and Self-Interaction Error. *J. Phys. Chem. Lett.* **2015,** *6* (8), 1461-6.
2. Uratani, H.; Yamashita, K., Charge Carrier Trapping at Surface Defects of Perovskite Solar Cell Absorbers: A First-Principles Study. *J. Phys. Chem. Lett.* **2017,** *8* (4), 742-746.
3. Wu, X.; Trinh, M. T.; Niesner, D.; Zhu, H.; Norman, Z.; Owen, J. S.; Yaffe, O.; Kudisch, B. J.; Zhu, X. Y., Trap states in lead iodide perovskites. *J. Am. Chem. Soc.* **2015,** *137* (5), 2089-96.
4. Camargo, F. V. A.; Nagahara, T.; Feldmann, S.; Richter, J. M.; Friend, R. H.; Cerullo, G.; Deschler, F., Dark Subgap States in Metal-Halide Perovskites Revealed by Coherent Multidimensional Spectroscopy. *J. Am. Chem. Soc.* **2019**.
5. Heo, S.; Seo, G.; Lee, Y.; Lee, D.; Seol, M.; Lee, J.; Park, J.-B.; Kim, K.; Yun, D.-J.; Kim, Y. S.; Shin, J. K.; Ahn, T. K.; Nazeeruddin, M. K., Deep level trapped defect analysis in $CH_3NH_3PbI_3$ perovskite solar cells by deep level transient spectroscopy. *Energy Environ. Sci.* **2017,** *10* (5), 1128-1133.
6. Xing, G.; Mathews, N.; Sun, S.; Lim, S. S.; Lam, Y. M.; Gratzel, M.; Mhaisalkar, S.; Sum, T. C., Long-range balanced electron- and hole-transport lengths in organic-inorganic $CH_3NH_3PbI_3$. *Science* **2013,** *342* (6156), 344-7.

7. Ghosh, T.; Aharon, S.; Etgar, L.; Ruhman, S., Free Carrier Emergence and Onset of Electron–Phonon Coupling in Methylammonium Lead Halide Perovskite Films. *J. Am. Chem. Soc.* **2017,** *139* (50), 18262-18270.
8. Hopper, T. R.; Gorodetsky, A.; Frost, J. M.; Müller, C.; Lovrincic, R.; Bakulin, A. A., Ultrafast Intraband Spectroscopy of Hot-Carrier Cooling in Lead-Halide Perovskites. *ACS Energy Letters* **2018,** *3* (9), 2199-2205.
9. Lim, S. S.; Giovanni, D.; Zhang, Q.; Solanki, A.; Jamaludin, N. F.; Lim, J. W. M.; Mathews, N.; Mhaisalkar, S.; Pshenichnikov, M. S.; Sum, T. C., Hot carrier extraction in CH3NH3PbI3 unveiled by pump-push-probe spectroscopy. *Science Advances* **2019,** *5* (11), eaax3620.
10. deQuilettes, D. W.; Koch, S.; Burke, S.; Paranji, R. K.; Shropshire, A. J.; Ziffer, M. E.; Ginger, D. S., Photoluminescence Lifetimes Exceeding 8 μs and Quantum Yields Exceeding 30% in Hybrid Perovskite Thin Films by Ligand Passivation. *ACS Energy Letters* **2016,** *1* (2), 438-444.
11. Guyot-Sionnest, P.; Wehrenberg, B.; Yu, D., Intraband relaxation in CdSe nanocrystals and the strong influence of the surface ligands. *The Journal of Chemical Physics* **2005,** *123* (7), 074709.
12. Pollock, T. P.; Schlenker, C. W., Electromodulation and Transient Absorption Spectroscopy Suggest Conduction Band Electron Lifetime, Electron Trapping Parameters, and CH3NH3PbI3 Solar Cell Fill Factor Are Correlated. *J. Phys. Chem. C* **2019,** *123* (30), 18160-18170.
13. Price, M. B.; Butkus, J.; Jellicoe, T. C.; Sadhanala, A.; Briane, A.; Halpert, J. E.; Broch, K.; Hodgkiss, J. M.; Friend, R. H.; Deschler, F., Hot-carrier cooling and photoinduced refractive index changes in organic-inorganic lead halide perovskites. *Nat. Commun.* **2015,** *6*, 8420.
14. Yang, Y.; Ostrowski, D. P.; France, R. M.; Zhu, K.; van de Lagemaat, J.; Luther, J. M.; Beard, M. C., Observation of a hot-phonon bottleneck in lead-iodide perovskites. *Nat. Photonics* **2015,** *10* (1), 53-59.
15. Fu, J.; Xu, Q.; Han, G.; Wu, B.; Huan, C. H. A.; Leek, M. L.; Sum, T. C., Hot carrier cooling mechanisms in halide perovskites. *Nature Communications* **2017,** *8* (1), 1300.
16. Juodawlkis, P. W.; Ralph, S. E., Hole-induced transient bandgap renormalization: A mechanism for photo-induced absorption in defect-engineered semiconductors. *Appl. Phys. Lett.* **2000,** *76* (13), 1722-1724.
17. Yang, Y.; Yang, M.; Zhu, K.; Johnson, J. C.; Berry, J. J.; van de Lagemaat, J.; Beard, M. C., Large polarization-dependent exciton optical Stark effect in lead iodide perovskites. *Nature Communications* **2016,** *7* (1), 12613.

Appendix A Supporting Information for Chapter 3

1. Device Performance Modeling

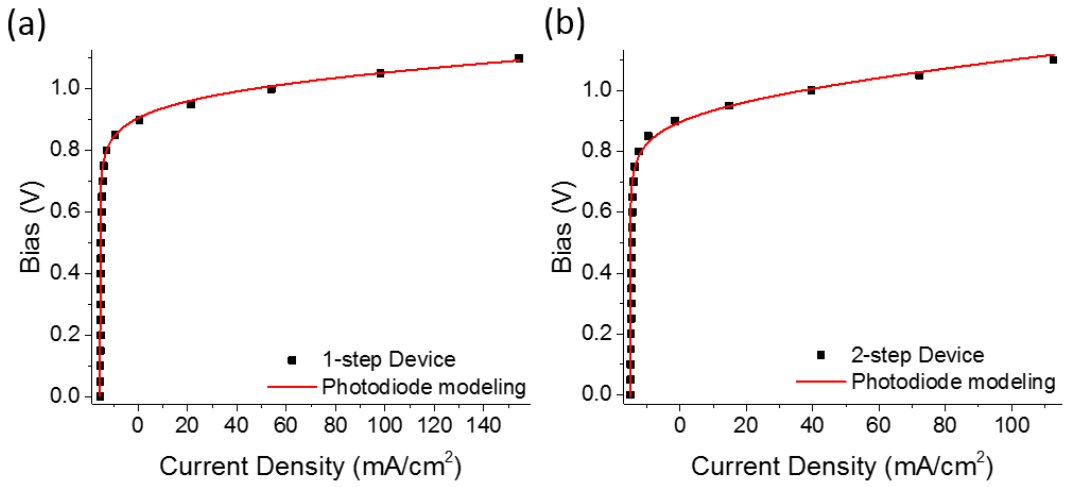

Figure A-1. Fitting of representative J-V data for 1- and 2-step devices to a simplified non-ideal diode equation (see main text).

2. Electroreflectance and Electrotransmission with Control Spectra

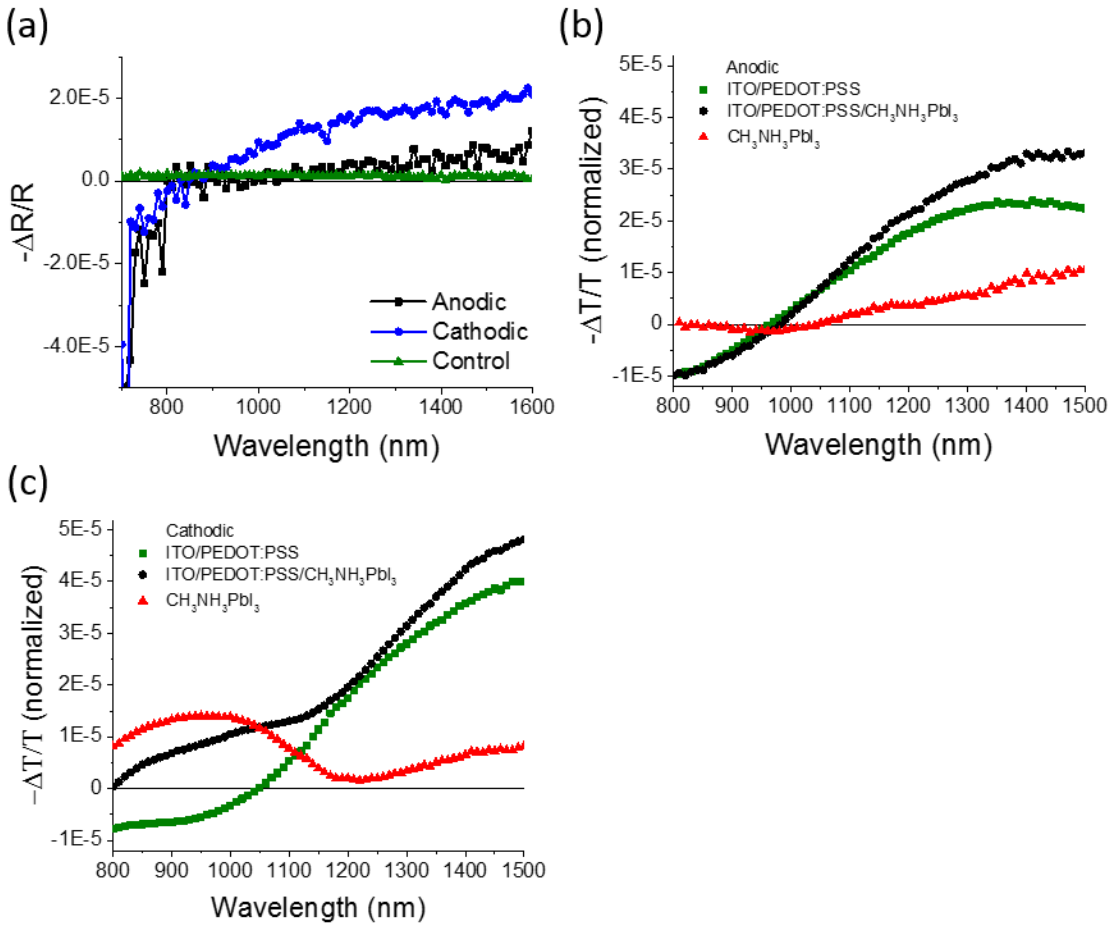

Figure A-2. (a) Electromodulated differential reflection (-ΔR/R) signal of $CH_3NH_3PbI_3$ deposited on the gold working electrode under cathodic (blue) or anodic (black) conditions. No difference was observed in the spectrum of the Au control electrode (green) comparing the applied potentials used for anodic and cathodic measurements. (b) Electromodulated differential transmission (-ΔT/T) signal of $CH_3NH_3PbI_3$ deposited on ITO/PEDOT:PSS working electrode under anodic conditions (black), the signal due to just ITO/PEDOT:PSS (green), and the difference of the two showing the signal of the $CH_3NH_3PbI_3$ layer (red). (c) The same as in (b), but under cathodic conditions.

In all cases, the green traces are measurements made on the bare Au or PEDOT:PSS-modified ITO electrode, with no $CH_3NH_3PbI_3$, under the same AC bias and at the same frequency. For all measurements made on ITO (all traces in Figure A-2 b and c), the electromodulation signal has been normalized to the amplitude of the AC current density, as the signal amplitude was found to increase linearly with respect to the current density. No change occurred in the shape or amplitude of the Au control spectra as a result of changing the DC bias between the cathodic (-0.75±0.4V vs. Fc/Fc^+) and anodic (0.04±0.4V vs. Fc/Fc^+) biases used for the $CH_3NH_3PbI_3$ samples.

For the control ITO/PEDOT:PSS measurements, a slight negative $-\Delta T/T$ is observed at wavelengths <1050 nm under cathodic conditions and <950 nm under anodic conditions, which we attribute to the changing oxidation state of the PEDOT:PSS layer. As a minor amount of degradation of the $CH_3NH_3PbI_3$ film still occurs under electromodulation conditions, albeit less than that which occurs under DC conditions, subtraction of the background ITO/PEDOT:PSS signal provides a $CH_3NH_3PbI_3$ spectrum which can only qualitatively be compared to other spectra, due to uncertainty in calculating an absorption cross section for each carrier transition.

3. Normalized Electroreflectance Spectra

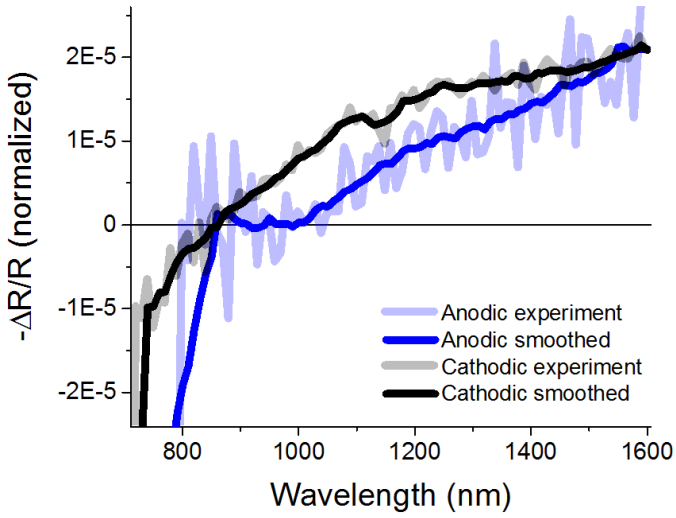

Figure A-3. Differential spectra for $CH_3NH_3PbI_3$ on Au normalized at 1580 nm to identify disparity between the anodic and cathodic charge accumulation conditions.

4. $CH_3NH_3PbI_3$ Film GIXRD Characterization

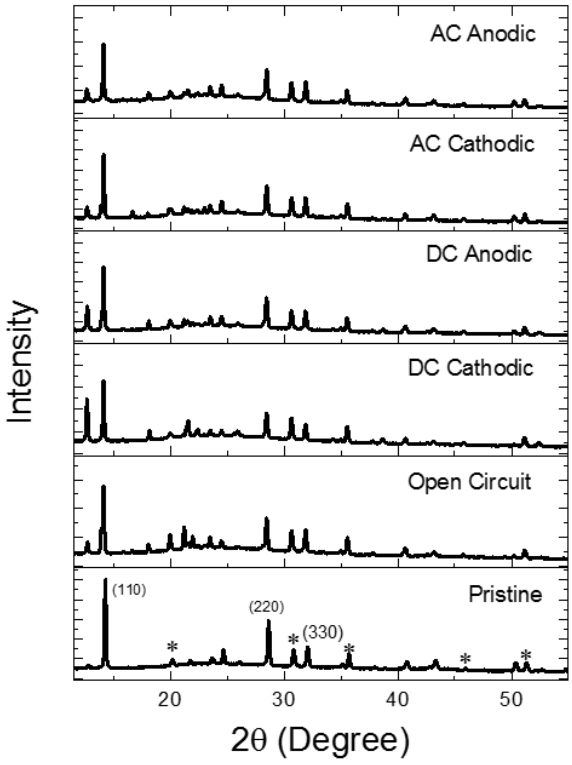

Figure A-4. GIXRD patterns of $CH_3NH_3PbI_3$ films on ITO/PEDOT:PSS substrates following DC spectroelectrochemical or DC + AC electromodulation measurements. Electrochemical measurements were made before removing each sample from the electrolyte solution, which were then dried at room temperature, all under an inert atmosphere, followed by GIXRD measurements. GIXRD measurements were performed under ambient atmospheric conditions. (110), (220), and (330) $CH_3NH_3PbI_3$ peaks are labeled on the pristine plot. ITO peaks are labeled with an asterisk (*).

Table A-1. Integrated Area and Ratio of PbI_2 (001) Peak (12.8°) and $CH_3NH_3PbI_3$ (110) Peak (14.3°).

Sample	Integrated Area (12.8°)	Integrated Area (14.3°)	Ratio (14.3°/12.3°)
Pristine	0.263	7.176	27.226
Open Circuit	0.956	7.972	8.336
DC Cathodic	3.172	4.642	1.463
DC Anodic	2.536	6.242	2.461
AC Cathodic	0.973	6.174	6.343
AC Anodic	0.911	4.428	4.860

5. Comparison of $CH_3NH_3PbI_3$ to PEDOT:PSS/$CH_3NH_3PbI_3$ Transient Absorption Spectra

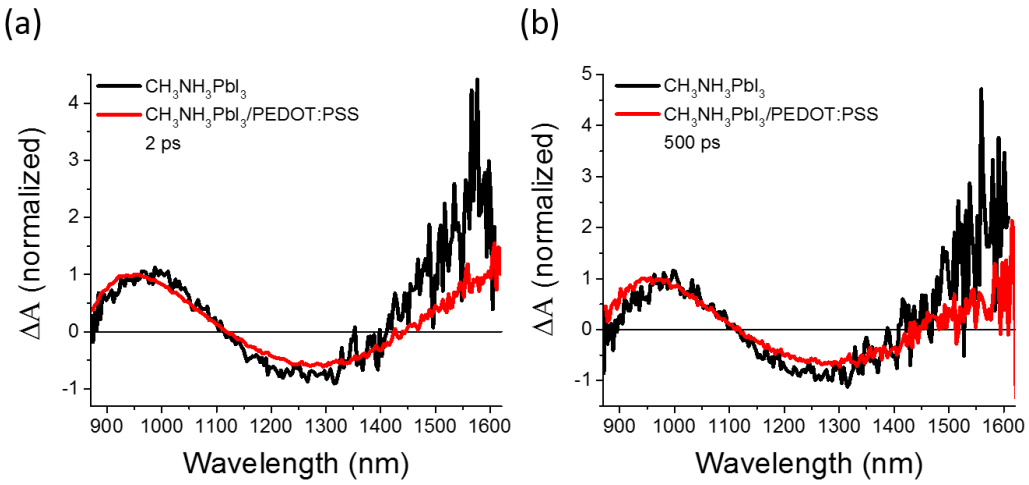

Figure A-5. Comparison of NIR transient absorption spectra between a single layer $CH_3NH_3PbI_3$ and double layer PEDOT:PSS/$CH_3NH_3PbI_3$ film, both deposited on glass at (a) 2 ps and (b) 500 ps. Spectra are normalized to their high energy peak.

6. Comparison of Electrotransmission and Transient Absorption Spectra

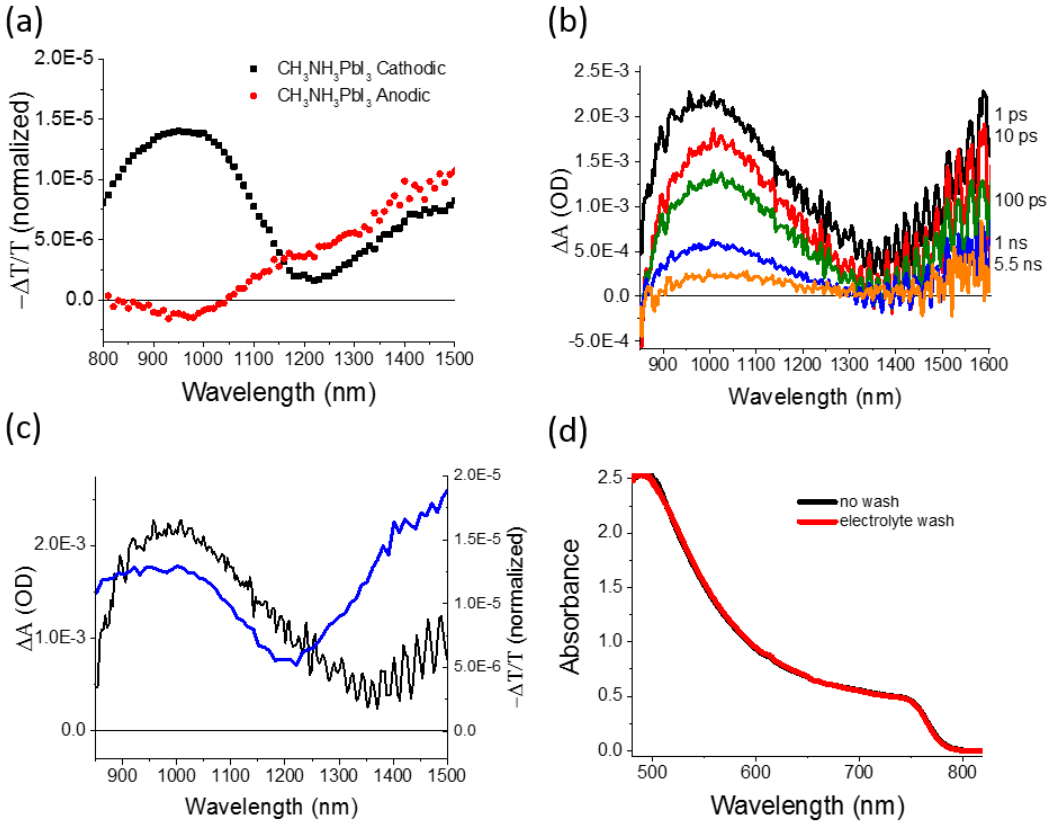

Figure A-6. (a) Electrotransmission spectra of $CH_3NH_3PbI_3$ after ITO/PEDOT:PSS background has been subtracted. (b) Transient absorption of $CH_3NH_3PbI_3$ film after washing in 0.1M $TBAPF_6$ dichloromethane solution. (c) Comparison of the sum of anodic and cathodic electrotransmission (blue) to transient absorption spectrum (black). (d) Comparison of ground state absorbance of $CH_3NH_3PbI_3$ deposited on glass before and after electrolyte wash.

For a more thorough comparison between the transmission mode electromodulation spectra and transient absorption spectra, which are made in transmission mode, we made transient absorption measurements on **2-step** $CH_3NH_3PbI_3$ films deposited on glass substrates which were washed in 0.1M $TBAPF_6$ dichloromethane solutions for the same time period as the electromodulation measurement (~15 minutes), followed by rinsing the film with

dichloromethane to remove any electrolyte which had adhered to the surface. It appears that there is some passivation or removal of surface defects due to this treatment, as the bleach observed in the untreated **2-step** film (Figure 3-2) is diminished in the transient absorption spectra of the electrolyte-washed sample (Figure A-6b), with only a notable valley near 1360 nm remaining.

Taking a linear combination of the anodic and cathodic $CH_3NH_3PbI_3$ electromodulation spectra and comparing it to a representative spectrum from the transient absorption of the electrolyte-treated film reveals similarity between the two spectra (Figure A-6c). As the transmission mode measurement reports on the bulk of the sample, in addition to the surface, it appears that defects not present at the surface of the film contribute to both spectra in Figure A-6c. As we've mentioned in the discussion comparing the transmission and reflection mode electromodulation spectra, the uncertainty in the absorption cross section for these carrier transitions makes the comparison of the linear combination of the anodic and cathodic spectra to the transient absorption spectra merely qualitative.

We also note that negligible degradation occurs to the $CH_3NH_3PbI_3$ film during the washing process as seen comparing the UV-vis absorption spectrum for a film before and after washing (Figure A-6d).

7. NIR Transient Absorption Fluence Dependence

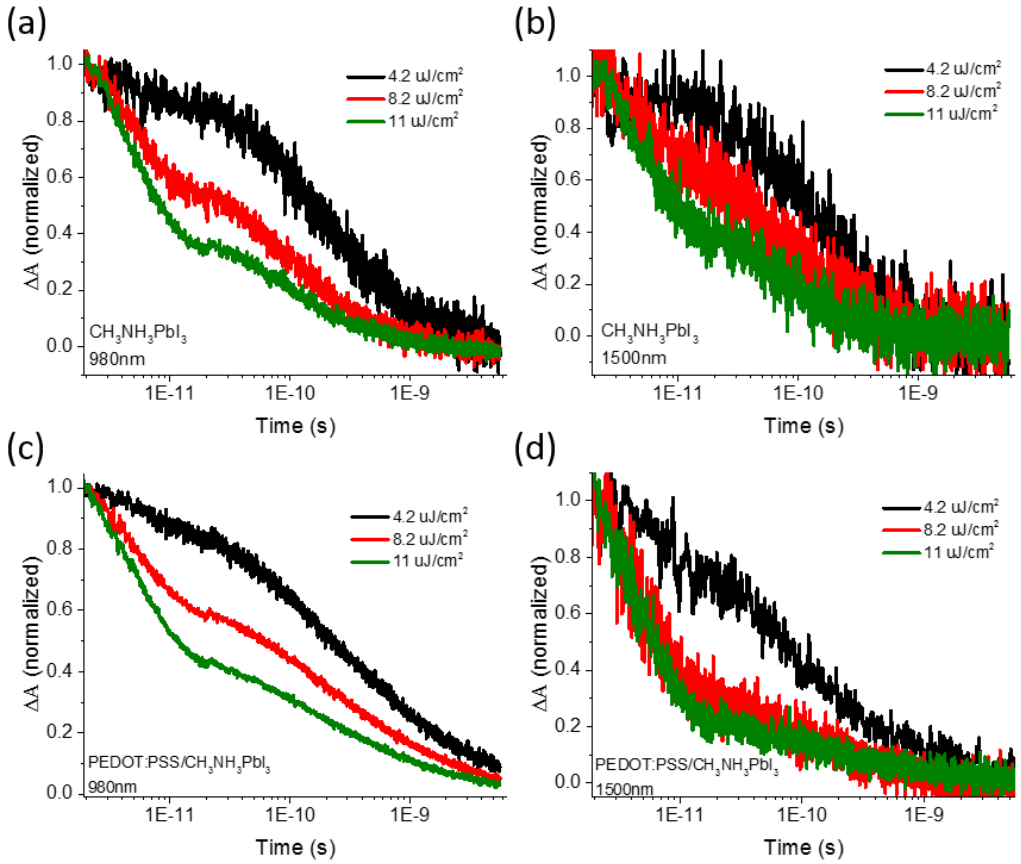

Figure A-7. Fluence dependence for kinetics at 980 nm and 1500 nm in both the single layer $CH_3NH_3PbI_3$ (2-step preparation) and bilayer PEDOT:PSS/ $CH_3NH_3PbI_3$.

8. Fitting h^+ Species Associated Spectra

$$\frac{dn_{VB}}{dt} = -k_R n_h (N_T - n_T) - k_2 n_e n_h - k_A (n_e^2 n_h + n_e {n_h}^2) - k_h n_h \quad \text{(A1)}$$

$$\frac{dn_{CB}}{dt} = k_T n_T n_e + k_2 n_e n_h + k_A (n_e^2 n_h + n_e {n_h}^2) + k_e n_e \quad \text{(A2)}$$

$$\frac{dn_T}{dt} = k_R n_h (N_T - n_T) - k_T n_T n_e \quad \text{(A3)}$$

$$\frac{dn_{TM}}{dt} = k_h n_h - k_e n_e \quad \text{(A4)}$$

Electron and hole species associated spectral kinetics were fit using each respective set of equations and forced to share respective carrier parameter values. For equations A1-A4, n_{VB} refers to the population of holes in the valence band following photoexcitation, n_{CB} refers to holes in the conduction band, and all other parameters remain the same as described in the main text and Figure 3-5d.

9. Statistical Analysis of Transient Absorption Fitting Parameters

	k_T	k_R	k_2	N_T	k_a	k_e	k_h
k_T	1	0.35761	-0.64228	-0.90987	0.80102	0.03466	-0.27916
k_R	0.35761	1	-0.81569	-0.51471	0.67203	0.81207	-0.96271
k_2	-0.64228	-0.81569	1	0.82	-0.95288	-0.55148	0.73975
N_T	-0.90987	-0.51471	0.82	1	0.2085	-0.10973	0.46136
k_a	0.80102	0.67203	-0.95288	0.2085	1	0.30956	0.56127
k_e	0.03466	0.81207	-0.55148	-0.10973	0.30956	1	-0.8975
k_h	-0.27916	-0.96271	0.73975	0.46136	0.56127	-0.8975	1

Table A-2. Correlation matrix for fitting of parameters for the SAS from table 3-2 in the main text.

	k_T	k_R	k_2	N_T	k_a
k_T	1	-0.62279	-0.68861	-0.8903	0.73651
k_R	-0.62279	1	-0.91373	-0.79632	0.90600
k_2	-0.68861	-0.91373	1	0.92195	-0.97668
N_T	-0.8903	-0.79632	0.92195	1	-0.91238
k_a	0.73651	0.90600	-0.97668	-0.91238	1

Table A-3. Correlation matrix for parameters from fitting the 1-step electron signal from table 3-3 in the main text.

	k_T	k_R	k_2	N_T	k_a
k_T	1	0.76009	-0.91441	-0.94081	0.92513
k_R	0.76009	1	-0.94996	-0.92698	0.94149
k_2	-0.91441	-0.94996	1	0.96741	-0.96461
N_T	-0.94081	-0.92698	0.96741	1	-0.95603
k_a	0.92513	0.94149	-0.96461	-0.95603	1

Table A-4. Correlation matrix for parameters from fitting the 2-step electron signal from table 3-3 in the main text.

Appendix B. Supporting Information for Chapter 4

1. Push Pulse Induced Hot Carrier Temperature Analysis

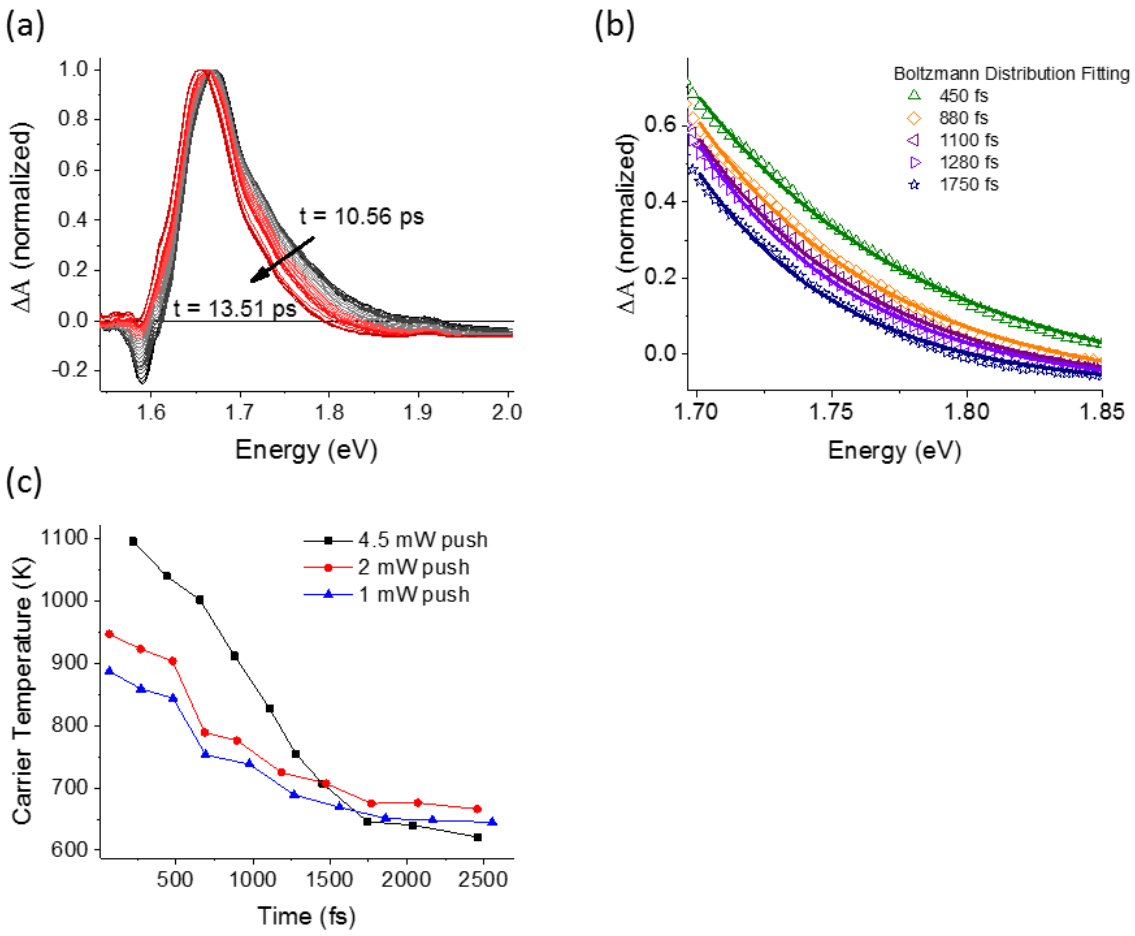

Figure B-1. (a) Transient absorption spectra normalized at the band edge bleach peak beginning at the peak of the push pulse overlap with the probe (t = 10.56 ps). (b) Fitting of the high energy portion of the bleach signal to a Boltzmann distribution at time points following the push peak. (c) Comparison of carrier temperature decay with push pulse fluence.

Per the method of Price et al.,[1] fitting the high energy portion (>1.7 eV) of the band edge to a Boltzmann distribution allows the charge carrier temperature to be calculated. At higher push pulse fluences, and corresponding higher hot carrier densities, we observe an increased

carrier temperature and a slower temperature decay in agreement with phonon bottleneck effect, which has previously been observed in perovskite systems. The carrier temperature at longer times (> 1500 fs) is elevated from what would be expected (~300 K) likely due to heating of the sample by the push pulse.

2. Hot Carrier Kinetic Analysis

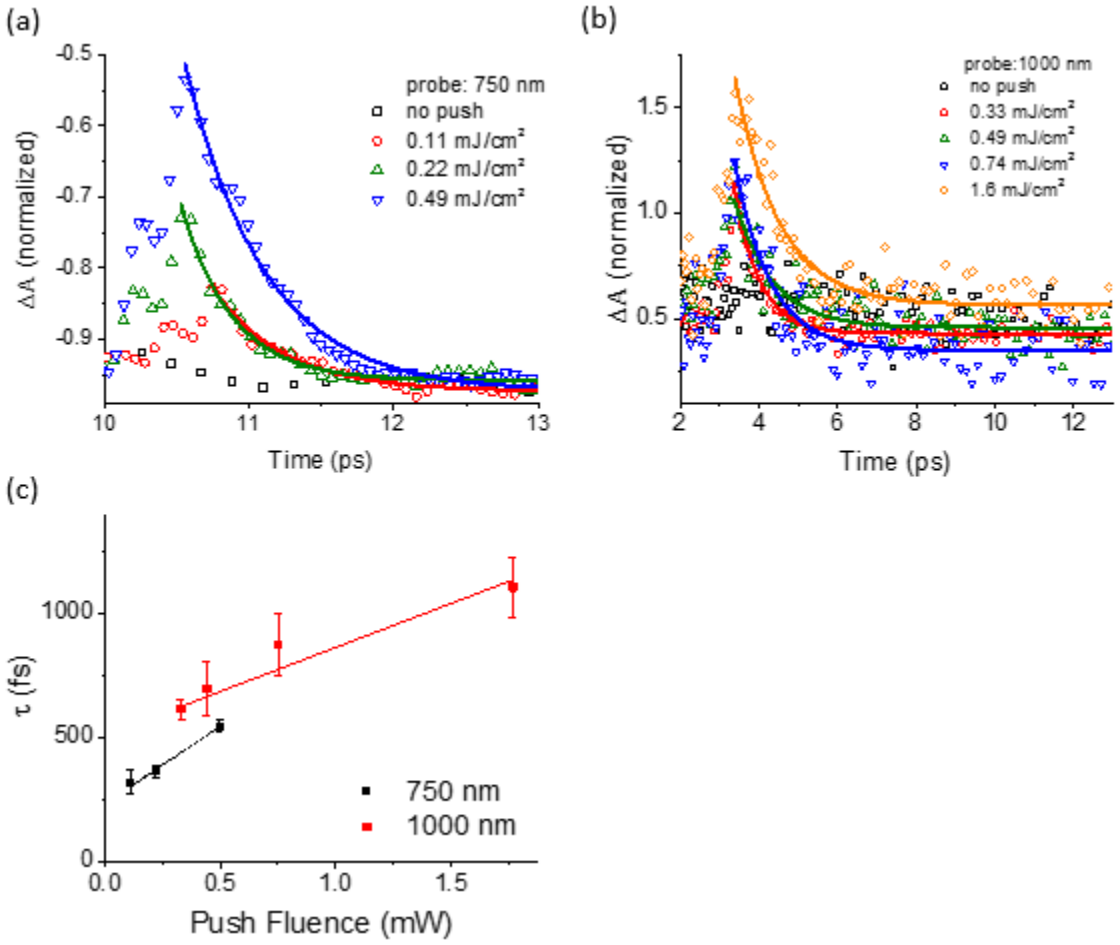

Figure B-2. Push pulse induced change in transient absorption kinetics for $CH_3NH_3PbI_3$ at (a) the band edge and (b) in the NIR. Solid lines represent monoexponential fits. Lifetimes for these fits are shown in (c).

3. Carrier Population Simulation

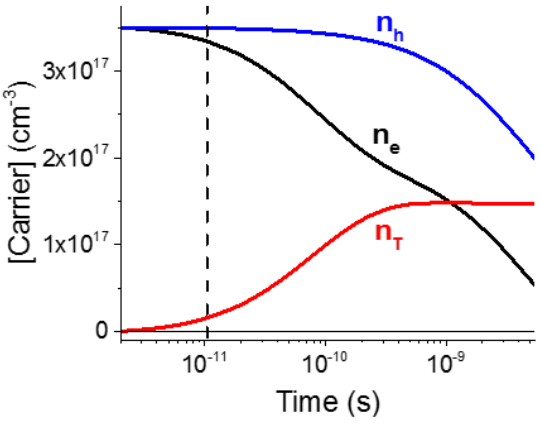

Figure B-3. Simulation of carrier dynamics for conduction band electron (n_e), valence band hole (n_h), and trapped electron (n_T) population. Dashed line indicates time delay for push pulse arrival in pump-push-probe measurements.

4. Low Energy Push Kinetic Comparison

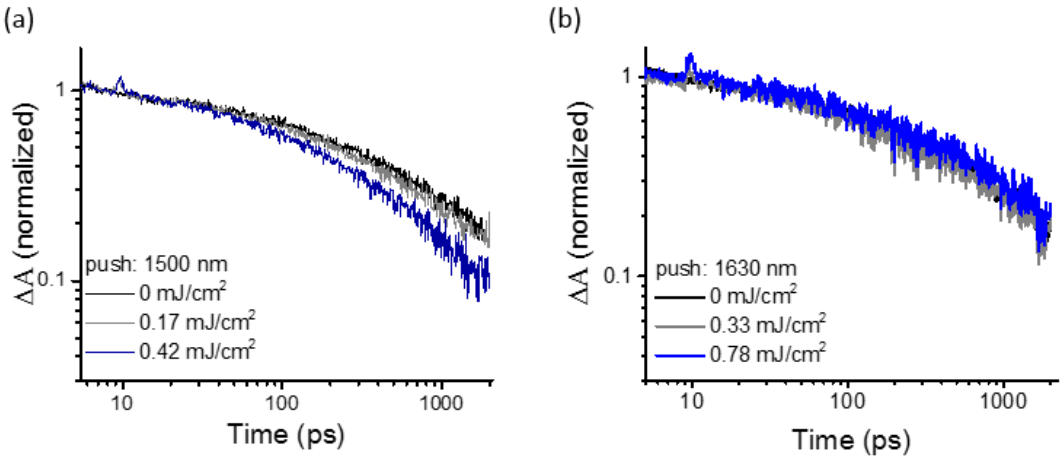

Figure B-4. Normalized pump-push-probe kinetics at 1000 nm with (a) 1500 nm push pulse and (b) 1630 nm push pulses.

5. Transient Absorption and Pump-Push-Probe kinetics for TOPO Passivated Samples

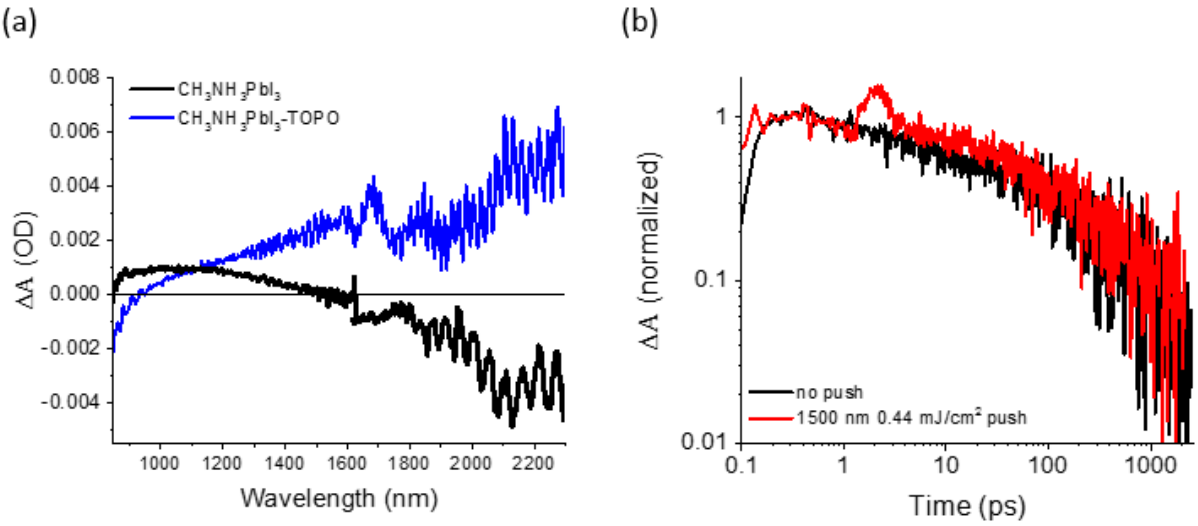

Figure B-5. (a) Comparison of excited state NIR transient absorption spectra for $CH_3NH_3PbI_3$ with (blue trace) and without (black trace) TOPO treatment. (b) Pump-push-probe kinetics at 1000 nm for a TOPO passivated $CH_3NH_3PbI_3$ sample comparing no push (black) and a 1500 nm push pulse (red).

6. Sub-gap Pump Transient Absorption Kinetics

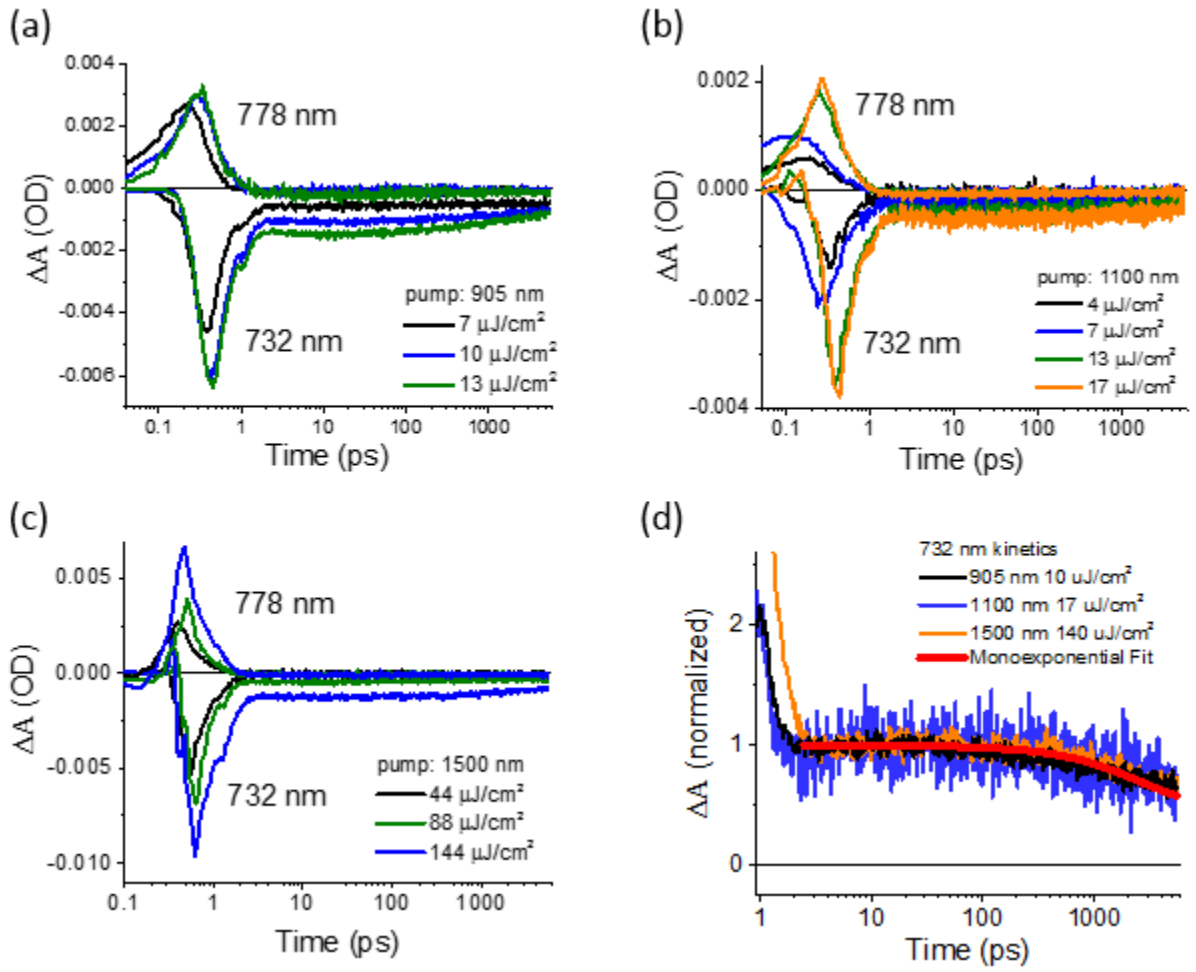

Figure B-6. Raw kinetics for the low energy induced absorption at 778 nm and the band edge bleach at 732 nm for a (a) 905 nm, (b) 1100 nm, and (c) 1500 nm pump. (d) Kinetics for the band edge bleach normalized following decay of the fast component showing pump energy independent recombination. Red line shows monoexponential fit for 1100 nm data.

References

1. Price, M. B.; Butkus, J.; Jellicoe, T. C.; Sadhanala, A.; Briane, A.; Halpert, J. E.; Broch, K.; Hodgkiss, J. M.; Friend, R. H.; Deschler, F., Hot-carrier cooling and photoinduced refractive index changes in organic-inorganic lead halide perovskites. *Nat. Commun.* **2015,** *6*, 8420.

Timothy P. Pollock

Education

Ph.D.	Chemistry, University of Washington	GPA: 3.48/4.00	2020
B.S.	Chemistry, University of California, San Diego	GPA: 3.81/4.00	2013
A.A.	Chemistry, San Diego Mesa College	GPA: 3.95/4.00	2011

Skills

- Time resolved and steady state optical characterization of semiconductor systems using transient absorption spectroscopy (including use of an optical parametric amplifier), UV-vis absorption, time-correlated single photon counting, raman microscopy, and photoluminescence quantum yield.
- Modeling semiconductor charge recombination kinetics using prebuilt target analysis software (Glotaran) as well as custom written code (C++).
- Electrochemical characterization of thin film semiconductor systems including electrochemical impedance spectroscopy, cyclic voltammetry, alternating current voltammetry, and electromodulation spectroscopy.
- Thin film characterization by scanning electron microscopy, profilometry, and x-ray diffraction.
- Photovoltaic device characterization by solar simulation, external quantum efficiency, and electroluminescence measurements.
- Knowledgeable in the use of monochromators, lock-in amplifiers, source meters, current preamplifiers, and LabView for the detection and measurement of optical and optoelectronic properties
- Semiconductor and metal thin film deposition techniques including solution phase spin coating, thermal evaporation, and electron beam evaporation.
- Maintenance, upkeep, and user training of a materials fabrication and characterization facility (University of Washington Photonics Research Center and Research Training Testbed) including: Gloveboxes, spin coaters, solar simulators, potentiostat, TCSPC, quantum yield system, thermal and e-beam evaporators.
- Maintenance, upkeep, and user training of a femtosecond laser with transient absorption and streak camera detection systems. (University of Washington Molecular Analysis Facility)

Research Experience

Ph.D. Candidate, Chemistry Department, University of Washington 2013-Present

- Fabricated hybrid perovskite photovoltaic devices utilizing solution phase spin coating, thermal evaporation, and electron beam evaporation
- Studied ultrafast charge carrier dynamics in molecular and solid state systems using transient absorption spectroscopy and time-resolved photoluminescence measurements
- Designed electromodulation spectroscopy experimental setup for the characterization of charge carrier spectral features in hybrid perovskite photovoltaic materials
- Modeled and simulated charge recombination kinetics in photoexcited semiconductor systems using Glotaran and custom written script (C++)

Research Assistant, Department of Chemistry and Biochemistry, UCSD 2012-2013

- Performed molecular synthesis to prepare ligands for mechanistic studies on the electrocatalytic reduction of CO_2
- Studied the influence of steric hindrance around the active metal site on electrocatalytic activity of homogeneous CO_2 reduction
- Performed DFT calculations to study the energy landscape relevant to molecular electrocatalytic CO_2 reduction

Publications

Pollock, T.P.; Schlenker, C. W., Improved Modeling of Trapping Kinetics in $CH_3NH_3PbI_3$ by Subgap Pump Transient Absorption and Pump-Push-Probe Spectroscopy, *manuscript in preparation,* **2020**

Pollock, T.P.; Schlenker, C. W., Electromodulation and Transient Absorption Spectroscopy Suggest Conduction Band Electron Lifetime, Electron Trapping Parameters, and $CH_3NH_3PbI_3$ Solar Cell Fill Factor Are Correlated, *Journal of Physical Chemistry C,* **2019**, 123, 30, 18160-18170

Bowring, M.A.; Bradshaw, L.R.; Parada, G.A.; **Pollock, T.P.**; Fernández-Terán, R.J.; Kolmar, S.S.; Mercado, B.Q.; Schlenker, C.W.; Gamelin, D.R.; Mayer, J.M., Activationless Multiple-Site Concerted Proton-Electron Tunneling, *Journal of the American Chemical Society*, **2018**, *140,* (24), 7449-7452

Presentations

MRS Spring Meeting 2019, Poster presentation, "*$CH_3NH_3PbI_3$ exhibits distinct NIR sub -gap absorption features in response to AC anodic and cathodic electrochemical modulation*"

Orcas Conference 2014, Poster presentation, "*Toward understanding hybrid perovskite excited state dynamics*"

Southern California Inorganic Photochemistry Conference 2012, Oral presentation, "*Electrocatalytic activity of nickel cyclam and it's derivatives"*

UCSD Summer Research Conference 2012, Oral presentation, "*Mono-methylated nickel cyclam synthesis and its role in electrocatalytic CO_2 reduction*"

Honors

Clean Energy Institute Travel Grant 2019
Clean Energy Institute Fellow, University of Washington 2015
David M. Ritter Endowed Fellow 2013

UCSD Summer Research Program Grant 2012
Dean's Honor List, San Diego Mesa College 2008-2010

Community Involvement/Public Outreach

Imagine Tomorrow Science Fair Judge, Ballard High School 2017
PacSci Nano Day, Pacific Science Center 2017
CEI outreach, Westhills Elementary School 2016
CENTC Highschool outreach coordinator 2016
CENTC outreach, Roosevelt High school 2015
PAWS on Science, Pacific Science Center 2016
PAWS on Science, Pacific Science Center 2015
Engineering Discovery Days, University of Washington 2015
Washington Trails Association, volunteer 2015
Washington Trails Association, volunteer 2014
CENTC outreach, Roosevelt High school 2014

Work Experience

Intern, Presidio Components Inc., San Diego, CA 2010-2011

- Worked in the production of dielectric material for use in capacitor fabrication.

References

- Cody W. Schlenker, Assistant Professor of Chemistry, University of Washington Chemistry Department, schlenk@uw.edu, (w) 206-221-8627
- Dana Sulas, Postdoctoral Research Scientist, National Renewable Energy Laboratory, Dana.Sulas@nrel.gov, (h) 608-239-7035
- Kristine Parra, Staff Scientist, University of Washington Clean Energy Institute, kpoparra@uw.edu, (w) 206-221-3334